PHYSICS BASED MODELING

OF AXIAL COMPRESSOR STALL

A Thesis Dissertation

Presented to

The Academic Faculty

By

Mina Adel Zaki

In Partial Fulfillment

Of the Requirements for the Degree

Doctor of Philosophy in the

School of Aerospace Engineering

Georgia Institute of Technology
December 2009

PHYSICS BASED MODELING

OF AXIAL COMPRESSOR STALL

Approved by:

Dr. Lakshmi N. Sankar, Advisor
School of Aerospace Engineering
Georgia Institute of Technology

Dr. Richard Gaeta
School of Aerospace Engineering
Georgia Institute of Technology

Dr. Suresh Menon
School of Aerospace Engineering
Georgia Institute of Technology

Dr. Alex Stein
Energy and Propulsion Technologies
GE Global Research Center

Dr. J.V. R. Prasad
School of Aerospace Engineering
Georgia Institute of Technology

Date Approved: August 21, 2009

In the name of the Father, and the Son, and the
Holy Spirit, one God. Amen.

"And those who know Your name will put their trust in You;
For You, LORD, have not forsaken those who seek You." Psalm 9:10.

Dedicated to my parents

For their continuous encouragement and endless love and support.

ACKNOWLEDGEMENTS

I would like first to thank my God and my Savior Jesus Christ for His gift of salvation, tender mercies, grace, and many blessings. I would also like to tha nk the Theotokos St. Mary and all the holy saints for interceding and praying for us all the time.

I would like to thank Dr. Lakshmi N. Sankar, my thesis advisor and mentor, for his guidance, advice, patience, and support throughout my research work. I would also like to thank Dr. Suresh Menon for his mentorship, support, and valuable recommendations. I would like to thank my thesis committee members: Dr. Lakshmi N. Sankar, Dr. Suresh Menon, Dr. J. V. R. Prasad, Dr. R. Gaeta, and Dr. Alex Stein for their valuable comments and suggestions. I would also like to thank Dr. J. Jagoda, the graduate coordinator, for his help and support. I would like to thank the past and present members of the CFD lab: Dr. Liu Yi, Dr. Sarun Benjanirat, Dr. Chanin Tongchitpakdee, Sujeet Phanse, Dr. Vishwas Iyengar, Nandita Yeshala, Nischint Rajmohan, Byung Young Min, and Jeremy Bain for creating a friendly environment in the lab.

I would like to thank my friends: Matthew Zaki, Randy Tadros, Sam Wanis, Ray Tadros, Rafik Hanna, and Bobby Zaki for their warm friendship, support, fellowship, and good times spent.

Finally, I owe my greatest gratitude to my parents, Adel Shaker Zaki and Irene Badie Naguib, for their encouragement, patience, and great love. I would like to thank my siblings: Afifa, Mariam, Gergis, and Shaker for all their love and support. Thank you!!!

TABLE OF CONTENTS

Page

LIST OF TABLES

Page

LIST OF FIGURES

Page

LIST OF SYMBOLS AND ABBREVIATIONS

A	Jacobian matrix
a	speed of sound
C_P	specific heat at constant pressure
C_p	pressure coeffieicent
C_k, C_{kl}, $C_{l,}$ C_υ	constants in the KES turbulence model
$CD_{k\omega}$	cross diffusion term in the k-ω-SST turbulence model
E, F, G	inviscid flux vectors
E_t	total internal energy
F_1, F_2	blending functions in the turbulence models
k	turbulent kinetic energy
L_{ref}	characteristic length of the configuration
$\dot{m}$	mass flow rate
p	pressure
q	conserved flow variables vector
R_v , S_v, T_v	viscous stresses and heat fluxes at a cell face
T	temperature
T	eigenvectors matrix of A
t	time
U	relative velocity normal to a cell face

u, v, w	Cartesian velocity components
x, y, z	Cartesian coordinates
y	distance to the neareast wall, used in the turbulence models
Δq	change in conserved flow variables from one time step to the next
Δt	time step
γ	specific heat ratio
$\gamma, \gamma_1, \gamma_2$	constants in the k-ω-SST turbulence model
Λ	eigenvalues matrix of A
κ	Von Karman constant
υ	molecular viscosity
υ_t	eddy viscosity
ρ	density
$\sigma_k, \sigma_{k1}, \sigma_{k2}, \sigma_{\omega 1}, \sigma_{\omega 2}$	constants in the k-ω-SST turbulence model
σ_k, σ_{kl}	constants in the KES turbulence model
Ω	vorticity in the turbulence models
ω	specific turbulent dissipation rate
τ_{ij}	stress tensor
ε	turbulent dissipation energy

Subscripts

i, j, k	Cartesian tensor indices
ξ, η, ζ	non-orthogonal body fitted coordinate system
∞, Ref	free stream flow quantities

Superscripts

n, n+1	two adjacent time levels

Over bars

~	used to indicate Roe averages
$\rightarrow$	used to indicate vectors
—	time or spatial averages

SUMMARY

Axial compressors are used in a wide variety of aerodynamic applications and are one of the most important components in aero-engines. However, the operability of compressors is limited at low-mass flow rates by fluid dynamic instabilities such as stall and surge. These instabilities can lead to engine failure and loss of engine power which can compromise the aircraft safety and reliability. Thus, a better understanding of how stall occurs and the causes behind its inception is extremely important.

In the vicinity of the stall line, the flow field is inherently unsteady due to the interactions between adjacent rows of blades, formation of separation cells, and the viscous effects including shock-boundary layer interactions. Accurate modeling of these phenomena requires a proper set of stable and accurate boundary conditions at the rotor-stator interface that conserve mass, momentum, and energy, while eliminating false reflections.

As a part of this research effort, an existing 3-D Navier-Stokes analysis for modeling single stage compressors has been modified to model multi-stage axial compressors and turbines. Several rotor-stator interface boundary conditions have been implemented. These conditions have been evaluated for the first stage (a stator and a rotor) of the two-stage fuel turbine on the space shuttle main engine (SSME). Their effectiveness in conserving global properties such as mass, momentum, and energy across the interface while yielding good performance predictions has been evaluated. While all the methods gave satisfactory results, a characteristic based approach and an unsteady sliding mesh approach are found to work best.

Accurate modeling of the formation of stall cells requires the use of advanced turbulence models. As a part of this effort, a new advanced turbulence model called the Hybrid RANS/KES (HRKES) model has been developed and implemented. This model solves the Menter's k-ω-SST model near walls and switches to the Kinetic Eddy Simulation (KES) model away from walls. The KES model solves directly for local turbulent kinetic energy and local turbulent length scales, alleviating the grid spacing dependency of the length scales found in other Detached Eddy Simulation (DES) and Hybrid RANS/LES (HRLES) models. Within the HRKES model, combinations of two different blending functions have been evaluated for integrating the near wall model with the KES model. The use of realizability constraints to bound the KES model parameters has also been studied for several internal and external flows.

The current methodology is used in the prediction of the performance map for the NASA Stage 35 compressor configuration as a representative of a modern compressor stage. The present approach is found to effectively predict the onset of stall. It is found that the rotor blade tip leakage vortex and its interaction with the shock wave is mainly the reason behind the stall inception in this compressor stage.

CHAPTER 1

INTRODUCTION

Modern compressors have a wide variety of applications, such as refrigeration and air conditioning systems, gas turbine systems, jet engines, power generation stations, and industrial processes. Compressors are one of the most important components within a gas turbine engine. The various components of an aero engine where the compressor forms the first part of the engine core are shown in Figure 1.1. Compressors are used to increase the total enthalpy of the working fluid using input shaft work. Compressors can be divided into four general types: reciprocating, rotary, centrifugal, and axial compressors. The first two types are aimed at reducing the volume of the gas. The other two types transfer energy to the fluid by accelerating it to high velocities and subsequently decelerating it through a diverging channel to convert this kinetic energy into pressure energy. The present study deals with axial compressors.

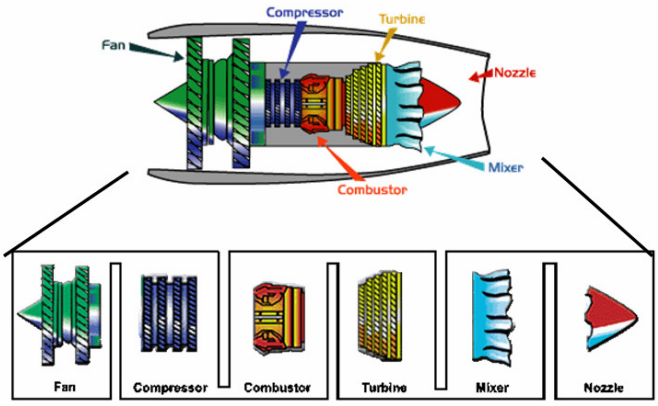

Figure 1.1: Components of a turbo-fan engine, Reference-http://en.wikipedia.org/wiki/Image:Axial-flow-compressor.png.

In axial compressors, flow enters and leaves the compressor in the axial direction. The compressor is made up of successive stages (multi-stages) attached to the shaft. Figure 1.2 shows a single stage of an axial compressor.[1] Each stage (Figure 1.2a) is made up of a row of rotor blades (where the energy is transferred from the rotating blades to the passing fluid, and the fluid flow accelerates), and a row of stator blades (where the fluid flow decelerates as it passes through diverging channels and the kinetic energy is converted into pressure energy). Thus, the compressor stage exerts work on the fluid and subsequently compresses the working fluid through progressively converging passages (Figure 1.2b), resulting in an increase of its stagnation and static pressure. This rise in the pressure energy relies on the work performed by the rotor on the fluid flow and the deceleration of the fluid through the stator. A single stage usually has a pressure ratio in the range of 1.15~2.0. The number of stages of a multistage compressor varies depending on its application. Increasing the number of stages in a compressor increases the total pressure ratio of that compressor, but also decreases its overall efficiency and increases its weight and cost.

The flow through modern axial compressors is very complex; it is inherently three dimensional and unsteady due to the relative motion between the successive blade rows and the viscous effects within each row. The flow is also transonic where regions of subsonic and supersonic flow coexist. Supersonic flow usually appears near the rotor tip leading edge where the highest rotational velocity is combined with the flow axial velocity, and the relative Mach number often exceeds unity. Such conditions lead to the

formation of a system of shock waves and three-dimensional shock boundary layer interactions.

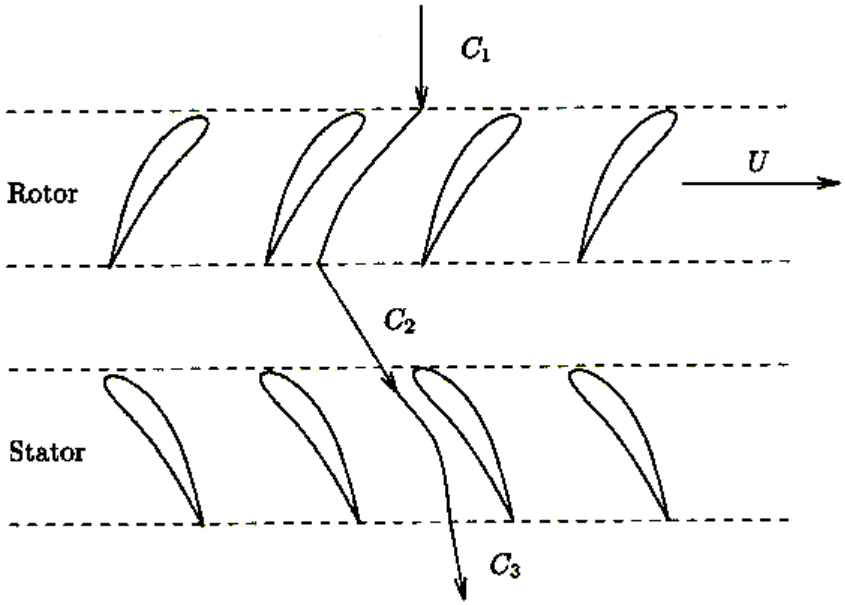

a) Cylindrical cross section

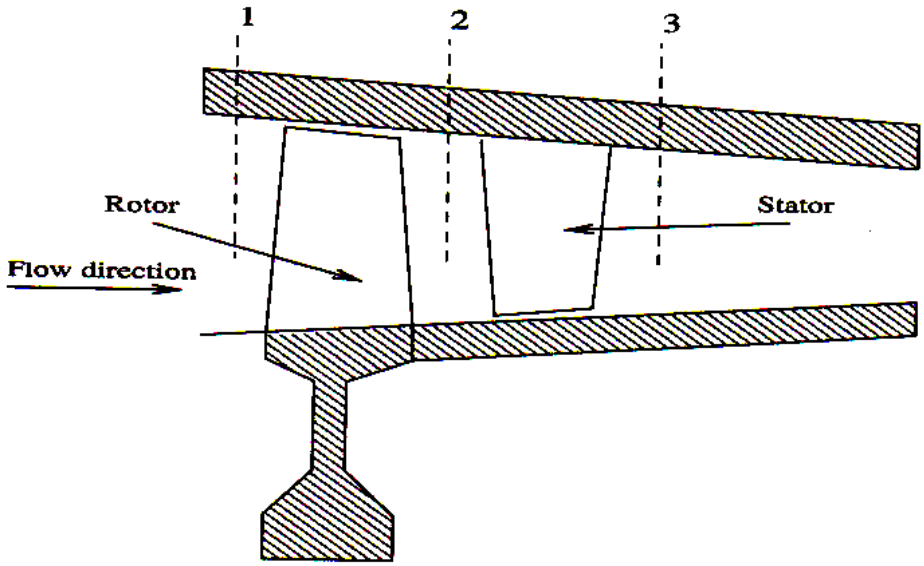

b) Axial cross section

Figure 1.2: Single stage of an axial compressor (Ref.1).

The complicated nature of the flow field coupled with the high blade loading needed to achieve high compression ratios makes it difficult to maintain a sufficiently large operating range. The useful operation range of compressors is limited at both very high and very low mass flow rates. At high mass flow rates, the operation of the compressor is limited by the occurrence of strong shock waves and the flow chokes through the compressor. Any attempt to raise the flow rate beyond this point will result in an increase in the shock strength, leading to a significant reduction in the efficiency of the compressor. At low mass flow rates, the operation of the compressor is limited by the onset of aerodynamic instabilities such as stall and surge. These instabilities are characterized by the occurrence of strong fluctuations and limit cycle oscillations in the flow properties and mass flow rate. Persistent oscillations can lead to blade fatigue and engine failure which can compromise the safety and reliability of the aircraft. Thus, an understanding of the three-dimensional transonic effects and both aerodynamic instabilities is a major aspect of compressor design and performance predictions.

A typical performance map for the compression system is shown in Figure 1.3 for a range of rotor RPM. The horizontal axis represents the mass flow rate through the compressor and the vertical axis represents the total pressure rise across the compressor. The dashed line on this plot represents the stall/surge line. However, stall and surge may still briefly occur to the right side of the stall/surge line. For this reason operating points are limited to a region to the right of the broken line to avoid stall and surge inception. The closer the operating point is to the surge/stall line, the greater the benefit of increased

pressure ratio, but the higher the risk of stall or surge. An accurate prediction of the stall/surge line is a crucial aspect of compressor design.

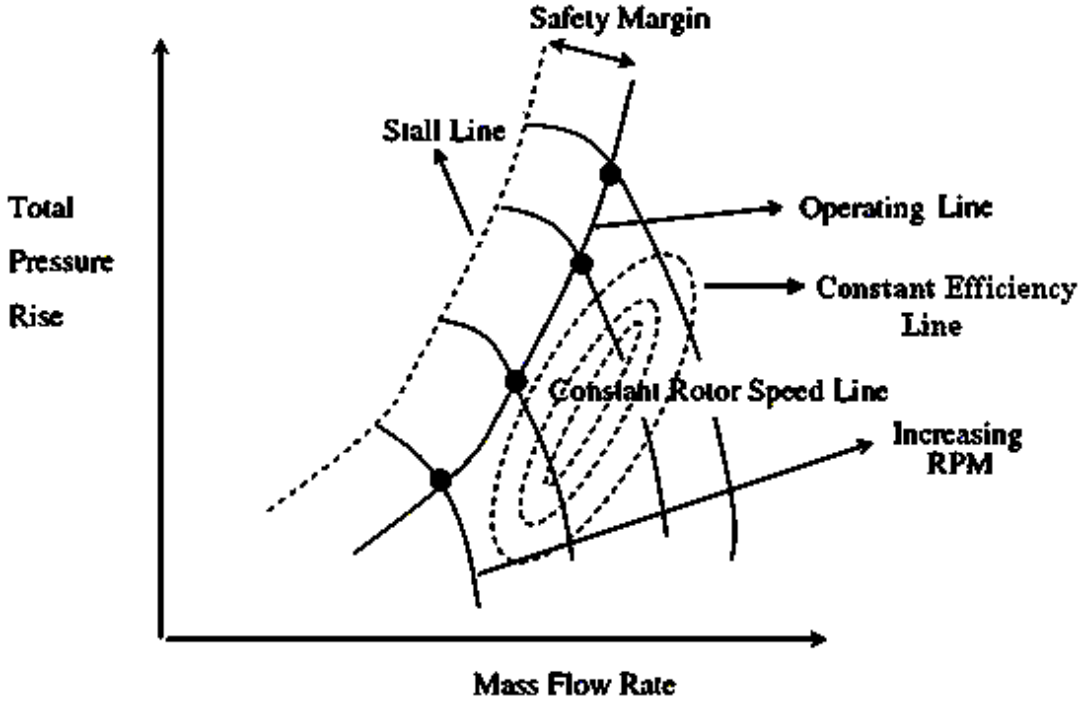

Figure 1.3: Typical compressor performance map.

1.1 Scope of Present Work

Most current Computational Fluid Dynamics (CFD) methods used in the simulation and analysis of turbomachinery flows are based on Reynolds Averaged Navier-Stokes (RANS) approaches, which rely on turbulence closure models for the eddy viscosity and conductivity. When the compressor operates in the vicinity of the stall/surge line, an accurate prediction of the flow field is significantly influenced by the prediction of the eddy viscosity field. If the eddy viscosity is underpredicted, computational simulations will predict larger separations in the flow field and the simulations will indicate that the compressor will stall before its actual stall point. On the other hand, if the eddy viscosity

is overpredicted, computational simulations will predict attached flows while the flow in reality may have stalled. Thus, turbulence modeling plays a very important role in determining the operation of the compressor in the vicinity of the stall/surge line.

Researchers have explored a variety of turbulence models to compute the flow field eddy viscosity. Turbulence models can generally be categorized based on their complexity. Zero-equation algebraic turbulence models are one of the earliest models which estimate the eddy viscosity based on a typical velocity scale and a typical eddy size length scale. One-equation turbulence models estimate the eddy viscosity by solving an eddy viscosity transport equation, or a transport equation for the turbulent kinetic energy. Two-equation turbulence models estimate the eddy viscosity by solving two transport equations. Although most of these models yield good predictions for attached flow fields, they fail to accurately predict flow structures in separated flow regions. To address this shortcoming, researchers have developed more advanced models such as Detached Eddy Simulation (DES) and Hybrid RANS/LES (HRLES) turbulence models. A literature survey of different turbulence models used is documented in great detail in the following chapter. Most of the DES and HRLES approaches used a one-equation model in the free shear layers to estimate the velocity scales associated with turbulent eddies while the length scale was estimated based on the grid spacing, as done in early LES work. Therefore, the transition between RANS and LES regions may depend entirely on the grid spacing, and it is not correlated with the local flow properties.

Most recently, a two-equation turbulence model was developed for the LES of wall-bounded turbulent flows at high Reynolds numbers. This model, called Kinetic Eddy

Simulation (KES), solves for both turbulence velocity and length scales, thus alleviating the grid spacing dependency found in the other LES models. The KES model has been applied to static stall, oscillatory attached and dynamic light stall, and dynamic deep stall flows around airfoils with good agreement with the experimental data.

1.2 Research Objectives

As mentioned in the previous section, most of the compressor stall inception studies that have been done to date used a RANS solver coupled with either a one or two equations turbulence model. Due to of the complicated physics behind stall inception, turbulence modeling plays a very important role in its detection. Thus, there is a huge need for more sophisticated turbulence models.

The objective of the current study is to develop, implement, and assess a Hybrid RANS/KES (HRKES) turbulence model for modeling stall inception. In the HRKES model, solving the KES model in the free shear layer alleviates the grid spacing dependency found in other DES and HRLES models. As a part of this effort, investigations are carried out to determine how to combine a classical RANS model near walls with the KES model away from walls and how to blend both models for a variety of external and internal flows.

Furthermore, modeling multi-stage compressors requires the use of a proper set of rotor-stator interface boundary conditions that conserves mass, momentum, and energy across the interface while eliminating any false reflections. As a part of this effort, several rotor-stator interface boundary conditions are implemented and evaluated.

Computational investigations are then carried out to study the stall inception in a single blade passage of a transonic compressor stage, NASA Stage 35, as a representative of a modern compressor stage. The flow field is analyzed in details to understand the relevant flow mechanisms behind the stall inception in this configuration.

1.3 Thesis Organization

The rest of the thesis is organized as follows. A survey of the research work in compressor stall inception predictions, different turbulence models used in computational fluid dynamics, and multistage interface boundary condition techniques are described in the second chapter.

The present methodology uses an in-house 3-D Navier-Stokes solver called GT-TURBO3D (Georgia Tech. Turbomachinery 3D), which is under continuous enhancements at the School of Aerospace Engineering at Georgia Institute of Technology. The governing equations, mathematical formulations, numerical formulation, and the recent developments employed in GT-TURBO3D are documented in details in the third chapter.

Prior to the application of the HRKES turbulence model to compressor stall predictions, this model is applied to simpler 2-D and 3-D internal and external flows. These validation studies are documented in chapter four. The rotor-stator interface boundary condition investigations are also documented in chapter four.

Performance predictions for the NASA stage 35 compressor configuration and the stall inception studies are presented in chapter five. Conclusions from this work and recommendations for future work are given in chapter six.

CHAPTER 2

LITERATURE REVIEW

In this chapter, the literature survey related to the current study is documented. A quick review of different Computational Fluid Dynamics (CFD) techniques, a survey of the research work in compressor stall, different turbulence models, and multistage interface boundary condition techniques are presented below.

2.1 Background

Computational techniques have been widely used in the design and analysis of turbomachinery. Until the1960s, most of the work done was limited only to potential flow solutions coupled with boundary layer methods due to the limitation of the computational resources, body fitted grid techniques, and the lack of stable time marching schemes and spatial discretization schemes.

Around 1969, MacCormack[2] developed one of the earliest successful techniques for integrating Navier-Stokes equations. During the 1970s, various grid generation techniques were developed for body fitted grids around general 2-D and 3-D configurations. Stable implicit time marching schemes (e.g.: Briley-Macdonald[3] , Beam–Warming[4]) were also developed and used successfully. These advancements, along with the increase in the computational speed and storage resources led to the explosion of CFD studies and applications for various internal and external flows, and in particular turbomachinery applications.

CFD techniques play a very important role in the design and analysis of turbomachinery. Early studies were two dimensional and focused on modeling blade to blade flow fields (e.g.: Denton,[5] Steger at al.,[6] Chima[7]) or meridional flow fields (e.g.: McNally[8]) to reach an optimum design for the blade sections. Improvements in computational resources and CFD techniques led to the ability of investigating the flow fields around three dimensional isolated and multistage blade rows and the causes behind the complicated flow instabilities that limit their stable operating range. (e.g.: Chima[9,10], Adamczyk et al.[11], Hathaway et al.[12,13]).

2.2 Compressor Stall

As mentioned in the previous chapter, there are two major aerodynamic instabilities that occur in compressors known as stall and surge. Compressor stall typically occurs first then the stall grows with time causing surge, which is a more severe and dangerous flow instability phenomena than stall. Compressor stall is a 2-D unsteady local phenomenon in which the flow is no longer uniform in the azimuthal direction. The average mass flow through the compressor during stall is nominally steady, but the flow has a circumferentially non-uniform mass deficit. Several types of compressor stall exist, part-span stall (where only a restricted region of the blade passage, usually the tip, is stalled), a full-span stall (where the entire height of the annulus is stalled with various stalled cells), and a small/large scale stall (where a small/large part of the annular flow path is blocked).

Many researchers have studied the stall inception mechanism in compressors. The basic explanation of the stall mechanism was given by Emmons et al.[14] as shown in

Figure 2.1. This figure shows the top view of a blade row. Stall is present on some of the blades. When one of the blades (blade B) stalls, as a consequence of some instability, the flow separation on the blade suction surface will cause a flow blockage between blade B and blade C. This blockage will lead to the diversion of the inlet flow streamlines towards the neighboring blades A and C, increasing the angle of attack on blade C causing it to stall and decreasing the angle of attack on blade A. As blade B rotates away from the disturbances, its angle of attack decreases, restoring normal flow over that blade. The stalled flow region, known as a stall cell, continues moving from blade to blade and propagates around the annulus. To a stationary observer, the stall cells appear to rotate at a lower RPM than the blades themselves. Compressor stall serves as a precursor to surge. Therefore, many of the ongoing computational and experimental studies have been aimed at detecting the stall onset.

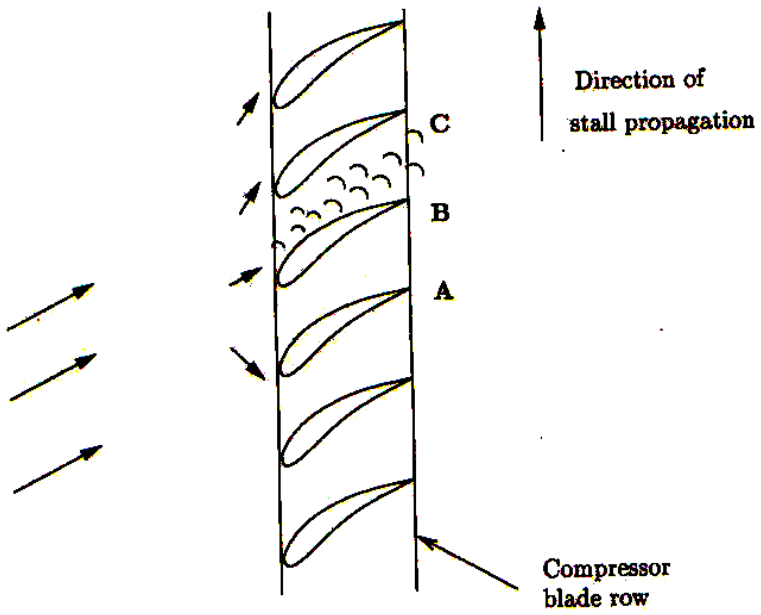

Figure 2.1: Physical mechanism for the inception of rotating stall (Ref.2).

It is well known that there are two distinctive routes to stall inception in compressors; the modal inception (long length scale) and the spike type inception (short length scale). The modal inception has been extensively studied and is believed to be well understood;[15-16] its inception can be described without considering details of the flow inside the blade passages. On the other hand, the spike type inception is not yet fully understood, especially in high speed compressors. Because the spike disturbances are comparable in scale to the mean velocity through the compressor, its analysis requires a detailed understanding of the flow structures within the blade passage.

Recently, many numerical studies have been reported on the role of flow structure in spike type stall inception in low-speed compressors.[17-19] These studies indicate that there are two main criteria behind stall inception. The first criterion is the net upstream mass flow at the trailing edge of the blade tip section. The second criterion is the leading edge tip clearance flow spillage.

As mentioned in the previous chapter, the flow mechanism behind stall inception is not as well understood in high-speed compressors as it is in low speed compressors. Few experimental or analytical studies have been reported on stall inception in a high-speed compressor. He et al.[20] numerically simulated stall inception in an isolated compressor blade row. Their study indicates that an isolated blade row with supersonic inflow tends to stall in a one-dimensional "surge-like" pattern without first experiencing rotating stall.

Niazi et al.[21] numerically simulated stall inception in an isolated transonic compressor blade row. Their study showed that at low mass flow rates, the tip leakage flow becomes stronger, and its interaction with the tip shock leads to compressor stall.

Their calculations showed that the use of bleed valves located on the diffuser walls eliminates these phenomena and restores the compressor back to its stable operating conditions.

Hah et al.[22] performed unsteady RANS analyses for an isolated transonic compressor rotor. The numerically produced stall indicator in terms of axial velocity was very similar to the measured stall signals from high-response pressure transducers mounted upstream of the rotor. The numerical analysis revealed that the axial positions of shocks detached from the rotor blades vary from blade to blade, and that this non-uniform shock front triggers the stall inception.

Haixin et al.[23] studied the stall mechanism in an isolated transonic axial compressor rotor with different tip gap heights. They found that for small tip gabs (0.4% blade span), the trailing edge vortex break down will trigger stall; while, for large tip gabs (1.0% blade span), the leading edge blade tip leakage vortex (BTLV) will trigger the stall. Various effects of the tip clearance gap on the flow field have been also studied by other researchers,[24,25] in which they obtained results for different tip clearance gap sizes with an accurate modeling of the clearance gap.

Hah et al.[26] carried out computational simulations for a transonic compressor rotor to identify the flow mechanism behind the spike-type stall inception. They found that the unsteady random behavior of the tip clearance vortex and its interactions with the passage shock seem to be critical factors in the development of spike-type stall in a transonic compressor. They showed that the spike-type stall develops after the passage shock is fully detached from the blade passages, and as the stalled blade passages are formed

behind the passage shock, the stalled area rotates counter to the blade rotation just like the classical Emmon's type stall.

Furthermore, many experimental efforts have been also made to detect stall and surge precursors.[27,28] For example, Dhingra et al.[29] experimentally described a new type of precursor to stall and surge inception by analyzing pressure signals using a correlation based scheme. They analyzed the pressure data measurements from two low speed compressors and one high speed compressor. Their measurements showed a consistent behavior for different rotor speeds. They found that the pressure sensor location is important for this technique.

2.3 Turbulence Modeling

As discussed in the previous section, the physics behind stall inception in axial compressor stages is complicated, and in order to be able to capture them accurately, high fidelity turbulence models should be used. As the compressor throttles towards stall, flow separation occurs and the wakes start to grow thicker. Turbulence modeling plays an important role in predicting such flows. Most current CFD methods used in the simulation and analysis of stall inception in axial compressors are based on Reynolds Averaged Navier-Stokes (RANS) approaches, in which the time-averaged mean effects are resolved and turbulence closure models are used to provide the flow field turbulent effects (e.g.: eddy viscosity). RANS turbulence closure models can be generally divided according to the number of additional equations used in the estimation of the flow turbulent viscosity as follows. Algebraic models or zero-equation models (e.g.: Smith and Cebeci model[30], Baldwin-Lomax model[31]) are of the earliest models to be used. In these

models algebraic equations are used to estimate the eddy viscosity based on a typical eddy size length scale and a velocity length scale. In zero-equation models, the convection of turbulence is not modeled, thus the physical effect of the past history of the turbulent viscosity in the flow is not included. Local equilibrium of production and dissipation effects are also implicitly assumed. In order to account for this physical effect, transport formulations derived from Navier-Stokes equations should be used. One-equation models (e.g.: Spalart-Allmaras (SA) model[32]) were subsequently developed in which a transport equation for the flow turbulent viscosity or the turbulent kinetic energy is solved. In one-equation models, length scales were specified empirically, which is not appropriate for complex turbulent flows. To address this drawback, two-equation models[33-35] were developed in which two transport equations for two turbulent variables (for example, turbulent kinetic energy and turbulent dissipation rate) are solved to estimate the flow field turbulent viscosity based on the predicted length scale and velocity scale. Examples for two-equation turbulence models are: k-ε model[33] which solves for turbulent kinetic energy and turbulent dissipation energy, Wilcox's k-ω model[34] which solves for turbulent kinetic energy and turbulent dissipation rate, and Menter's k-ω-SST model[35] which solves Wilcox's k-ω model[34] near walls and switches to k-ε model[33] away from walls. Two-equation turbulence models are commonly used in most of the RANS solvers.

Although most of the RANS approaches mentioned above yield good predictions for attached flows, they fail to accurately predict flow structures in separated flow regions because they resolve only a portion of the turbulence scales of interest. Of course, the

ideal approach would be Direct Numerical Simulation (DNS), because the entire range of spatial and temporal scales of turbulence is resolved, but the computational cost of DNS is prohibitive. Another intermediate technique between DNS and RANS has been proposed to replace RANS in such cases (Figure 2.2); this approach is called Large Eddy Simulation (LES).

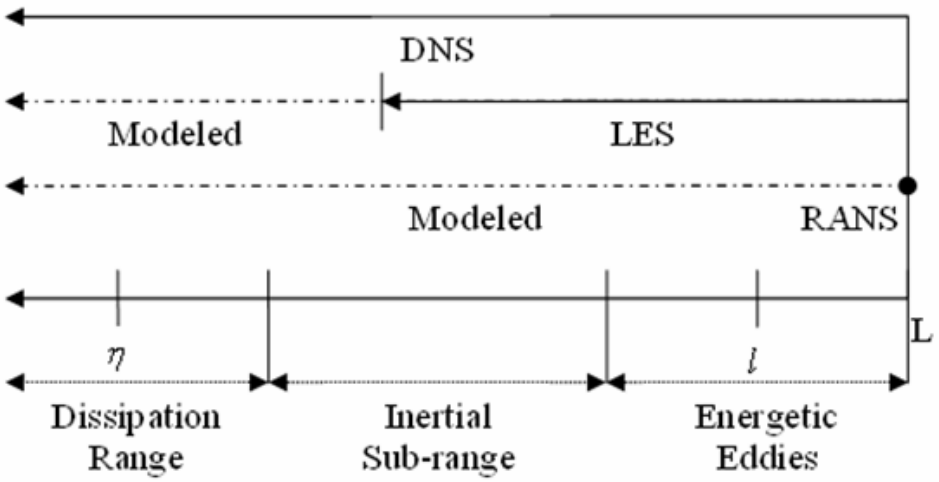

Figure 2.2: Resolution of turbulence scales by different numerical techniques.

In LES[36], the contribution of large energy containing structures and all scales larger than the grid resolution to momentum and energy transfer is computed, and the effect of sub-grid unresolved small scales is modeled. The main limitation of LES is that the wall shear layers have to be accurately resolved. In order to capture the near-wall flow structures in the LES approach, the distance from the wall to the first grid point should be about two wall units[36] (y^+~1). This requirement along with commencing grid spacing in the other directions gives rise to a large grid requirement and thus a prohibitive computational cost. To alleviate this grid resolution requirement, researchers have

proposed using RANS in near-wall regions and use an LES approach away from walls. These approaches have been called Hybrid RANS/LES (HRLES) methods.

The need for different approaches for computing turbulent Reynolds stresses near the wall and away from the wall was recognized as early as the 1960s during the development of the zero-equation turbulence models.[30,31] Smith and Cebeci (Ref. 30) computed eddy viscosity in the region close to the wall using Prandtl's mixing length model, while using eddy viscosity that is proportional to the product of the boundary layer edge velocity and the displacement thickness away from the wall. This approach, called the Cebeci-Smith model, was adopted in early turbulence models for use in Navier-Stokes analyses. For example, the well-known Baldwin-Lomax model[31] uses Prandtl's mixing length theory near walls and an approach similar to Cebeci-Smith elsewhere. In these models, distance from the nearest solid walls was used to compute the model length scales.

Later in the 1990s, Spalart et al.[37] realized that in free shear layers, the distance from the wall does not represent an appropriate length scale. Other length scales such as shear layer thickness are more relevant. Inspired by ongoing research on LES, Spalart extended the earlier one-equation Spalart-Allmaras (SA) model[32] so that it yielded a conventional eddy viscosity near the wall bounded regions but switched to a pseudo Smagorinsky LES model that is proportional to the grid spacing (Δ) away from the wall. This approach, called Detached Eddy Simulation (DES), was found to yield superior results compared to the earlier approaches for separated flows (e.g., static and dynamic

stall). Other researchers[38-41] proposed similar concepts of DES based on two-equation turbulence models (e.g.: k-ε model[33], k-ω-SST model[35]).

Other HRLES approaches have also been proposed. Baurle et al.[42] proposed a hybrid technique based on a combination of the k-ω-SST model[35] and the one-equation sub-grid scale turbulent kinetic energy model.[42] They used this model to simulate an incompressible Poiseuille flow, a supersonic base flow, and a supersonic flow over recessed cavities and they compared those results with DES computations. Their hybrid models showed improvements over the RANS model in the prediction of velocity profiles downstream of separation.

Xiao et al.[43] proposed a hybrid technique based on a combination of the two-equation k-ζ (enstrophy) model[44] and the one-equation sub-grid scale turbulent kinetic energy model. They applied it on two supersonic flow cases over a compression corner and a compression/expansion. Their hybrid models showed improvements over the RANS model only for the compression ramp case. In both cases, the RANS and the hybrid models did not predict the observed rapid recovery of the turbulent boundary layer after the reattachment point.

Basu et al.[45] proposed a hybrid technique based on a combination of the k-ε model[33] and the one-equation sub-grid scale turbulent kinetic energy model.[46] They used this model to simulate a transonic flow over an open cavity corner. Their results showed that all their proposed models captured the three dimensionality of the flow field, the fine scale flow structures, and the unsteady shedding of vortices.

Sanchez-Rocha et al.[47] proposed a hybrid technique based on a combination of the k-ω-SST model[35] and the one-equation localized dynamic sub-grid scale turbulent kinetic energy model (LDKM).[48] They used it to simulate the unsteady 2-D and 3-D flows over a static and oscillating airfoil. They conducted 2-D simulations for three dynamic stall conditions (attached flow, mild stall and deep stall) and 3-D simulations for a deep stall case with a good agreement with the experimental results.

All the aforementioned DES and HRLES models used a one-equation sub-grid scale turbulent kinetic energy model in the free shear layers to estimate the velocity scales associated with turbulent eddies. The length scale was estimated based on the grid spacing, as done in early LES work. This deficiency was addressed by Fang and Menon (Ref. 49, 50); they developed a two-equation sub-grid model for the LES of wall-bounded turbulent flow at high Reynolds numbers. This approach, called Kinetic Eddy Simulation (KES), solves for both sub-grid kinetic energy (k) and sub-grid length scales (l). The KES[49,50] model has been applied to static stall around a NACA0015 wing, oscillatory attached and dynamic light stall, and dynamic deep stall flows around a NACA0015 airfoil with good agreement with the experimental data. Versions of this model have also been applied to helicopter rotors in forward flight.[51,52]

2.4 Multistage Interface Boundary Conditions

As mentioned earlier, the physics behind stall inception in axial compressor stages is complicated, and in order to be able to capture them accurately, and to preclude the numerical reflections from clouding the observed phenomena, proper rotor-stator interface boundary conditions should be used in the simulations of multi-stage

turbomachinery. Flow fields of multi-stage turbomachinery tend to be extremely complex as the flow is inherently unsteady and three dimensional due to interactions between adjacent rows of blades. Over the last two decades, considerable progress has been made in understanding and modeling axial turbo-machinery flow fields and heat transfer.[53-57] In simulating the flow through multiple blade rows, one major obstacle is the relative motion between the rotor and stator blades.[61] A proper set of stable and accurate boundary conditions must be used at the rotor-stator interface to conserve local and global fluxes, and eliminate false reflections.

Several interface boundary conditions exist for modeling the flow through multi-stage turbo-machines.[58-61] Some of these include: isolated blade rows analysis, averaging plane methods, average passage methods, and fully unsteady methods.

Isolated blade row analysis allows the analysis of successive blade/vane rows from inlet to exit. Information flows from upstream stages to the downstream stages. This method allows solving the blade rows successively and does not model any of the transient interactions between the successive blade rows. In most approaches, the averaging plane method is used, where the flow properties are averaged (mixed out average, kinetic energy average) before being passed on to the neighbor set of blades. Some researchers used characteristic boundary condition approaches[58-60] in which they applied a characteristic based approach to the averaging plane method. These methods allow solving all the blade rows simultaneously. While all the averaging plane method based approaches have the advantage of conserving mass, momentum, and energy at each radial location in a global sense, the averaging smears out the azimuthal (blade to blade)

details of the flow field. To overcome these limitations, average passage approaches[53,54] and full unsteady approaches[61] (overset grids, sliding meshes) were subsequently developed. In the average passage approaches,[53,54] the effects of the blade to blade flow variations (e.g.: wakes, pressure waves) are modeled. While in the full unsteady approaches[61] (unsteady sliding mesh), interpolation takes place at the interface boundary between the successive blade rows to ensure the continuity of the flow variables across the interface.

CHAPTER 3

NUMERICAL AND MATHEMATICAL FORMULATION

This study uses an existing 3-D Navier-Stokes solver (GT-TURBO3D) which is under continuous development at Georgia Institute of Technology. GT-TURBO3D was built for earlier studies[62,63] to model single stage compressors. In these earlier studies a one equation Spalart-Allmaras (S-A) turbulence model was employed.

As part of the current investigations, two-equation k-ω-SST, two-equation Kinetic Eddy Simulation (KES), and Hybrid k-ω-SST/KES turbulence models have been implemented in GT-TURBO3D. Local time stepping, C-grid capability, and several multi-stage interface boundary conditions have also been implemented. In this chapter, the governing equations, mathematical formulation, and numerical tools employed in the current methodology are documented.

In Section 3.1 unsteady compressible flow equations are presented. In Section 3.2 the numerical discretization process and the solution algorithm used in GT-TURBO3D are described. In Section 3.3 turbulence models implemented in this analysis are discussed. Finally, in Section 3.4 the initial and boundary conditions are described.

3.1 Governing Equations

The system of partial differential equations for the conservation of mass, momentum, and energy in fluid flow are known as the Navier-Stokes equations. These equations are derived from first-principles. Navier-Stokes equations describe the physics of 3-D, unsteady compressible viscous flow, subject to some stress-strain rate relationships. In this study, calorically perfect Newtonian fluids, obeying Stokes' linear stress-strain rate

law, are considered. In three-dimensional Cartesian coordinates, the conservative form of Navier-Stokes equations in vector form is written as follows:

$$\frac{\partial q}{\partial t}+\frac{\partial E}{\partial x}+\frac{\partial F}{\partial y}+\frac{\partial G}{\partial z}=\frac{\partial R_v}{\partial x}+\frac{\partial S_v}{\partial y}+\frac{\partial T_v}{\partial z} \tag{3-1}$$

Where, q is the state vector, ρ is the density, the momentum components in x, y, z directions are ρ u, ρ v, and ρ w, respectively, and the total energy is E_t. The quantity E_t is the summation of the internal energy ($\frac{p}{\gamma-1}$) and kinetic energy $\frac{1}{2}\rho(u^2+v^2+w^2)$ and p is the static pressure The quantities E, F, G are the inviscid flux terms, and R_v, S_v, T_v are the viscous terms. The state vector, inviscid flux terms, and viscous terms are as follows:

$$q=\begin{Bmatrix}\rho\\ \rho u\\ \rho v\\ \rho w\\ E_t\end{Bmatrix},\quad E=\begin{Bmatrix}\rho u\\ \rho u^2+p\\ \rho uv\\ \rho uw\\ (E_t+p)u\end{Bmatrix},\quad F=\begin{Bmatrix}\rho v\\ \rho uv\\ \rho v^2+p\\ \rho vw\\ (E_t+p)v\end{Bmatrix},\quad G=\begin{Bmatrix}\rho w\\ \rho uw\\ \rho uw\\ \rho w^2+p\\ (E_t+p)w\end{Bmatrix},$$

$$R_v=\begin{Bmatrix}0\\ \tau_{xx}\\ \tau_{xy}\\ \tau_{xz}\\ u\tau_{xx}+v\tau_{xy}+w\tau_{xz}+-K\frac{\partial T}{\partial x}\end{Bmatrix},\quad S_v=\begin{Bmatrix}0\\ \tau_{yx}\\ \tau_{yy}\\ \tau_{yz}\\ u\tau_{y}x+v\tau_{yy}+w\tau_{yz}+-K\frac{\partial T}{\partial y}\end{Bmatrix},$$

$$T_v = \begin{Bmatrix} 0 \\ \tau_{zx} \\ \tau_{zy} \\ \tau_{zz} \\ u\tau_{zx} + v\tau_{zy} + w\tau_{zz} + -K\dfrac{\partial T}{\partial z} \end{Bmatrix} \tag{3-2}$$

Where,

$$\begin{aligned} p &= \rho RT = (\gamma - 1)\left[E_t - \frac{1}{2}\rho(u^2 + v^2 + w^2) \right] \\ \tau_{xx} &= \lambda(u_x + v_y + w_z) + 2\mu u_x \\ \tau_{xy} &= \tau_{yx} = \mu(u_y + v_x) \\ \tau_{xz} &= \tau_{zx} = \mu(u_z + w_x) \\ \tau_{yy} &= \lambda(u_x + v_y + w_z) + 2\mu u_y \\ \tau_{yz} &= \tau_{zy} = \mu(v_z + w_y) \\ \tau_{zz} &= \lambda(u_x + v_y + w_z) + 2\mu u_z \end{aligned} \tag{3-3}$$

In the above equations, T is the temperature. Here, γ is the specific heat ratio (~1.4 for air at standard conditions). Also, μ is the molecular viscosity, and λ is defined as $-\frac{2}{3}\mu$ (using Stokes hypothesis). The quantity K is the thermal heat conductivity coefficient of the fluid; it is defined as $\frac{C_P \mu}{\mathrm{Pr}}$ (where Pr in the laminar Prandtl number (~0.72) and C_P is the specific heat at constant pressure).

It is convenient to non-dimensionalize all quantities in the Navier-Stokes equations by their corresponding reference values. This would provide conditions where dynamic and energetic similarity may be obtained for geometrically similar configurations.

Secondly, the equations will provide values of the order of (~1) which will reduce the round off error during computations. The following reference parameters have been used in this work for non-dimensionalization.

$$
\begin{aligned}
L_{Ref} &= Diameter\ of\ the\ rotor,\ at\ the\ blade\ trailing\ edge \\
V_{Ref} &= a_{\infty} \\
\rho_{Ref} &= \rho_{\infty} \\
T_{Ref} &= T_{\infty} \\
p_{Ref} &= \frac{\rho_{\infty} a_{\infty}^2}{\gamma} \\
\mu_{Ref} &= \mu_{\infty}
\end{aligned}
\tag{3-4}
$$

Here, the free stream speed of sound is used as a reference velocity instead of the rotor blade tip speed.

3.2 Discretization and Numerical Solution of the Governing Equations

Analytical solution of the Navier-Stokes equations is limited to simple geometries. Therefore, for complex geometry and flows, numerical techniques must be used to find an approximate solution for such cases. In numerical approaches, solutions are found at discrete points at discrete time levels. Several numerical techniques, such as finite difference methods, finite element methods, and finite volume methods, exist for solving the Navier-Stokes equations. The finite volume method is commonly used in fluid dynamic problems. In this study, the 3-D unsteady compressible Reynolds-averaged Navier-Stokes equations are cast in an integral form, and solved using a finite volume scheme.

The integral form of Equation (3-1) is:

$$\iiint_V \frac{\partial q}{\partial t} dV + \iint_S (E\vec{i} + F\vec{j} + G\vec{k}) \cdot \vec{n} dS - \iint_S q\vec{V}_G \cdot \vec{n} dS = \iint_S (R_v\vec{i} + S_v\vec{j} + T_v\vec{k}) \cdot \vec{n} ds \tag{3-5}$$

Here, V is the control volume; S is the surface of the control volume, and $\vec{n}$ represents the outward normal vector to surface S. The term $\vec{V}_G$ refers to the velocity of the surface S.

The flow field is divided into discrete volumes and Equation (3-5) is applied. In the present work, hexahedral cells are used (Figure 3.1). The state vector q is evaluated at the cell vertices and the surface integrals are computed at the cell faces surrounding the control volume as follows:

$$\iint_s (E\vec{i} + F\vec{j} + G\vec{k}) \cdot \vec{n} dS - \iint_S q\vec{V}_G \cdot \vec{n} dS = \sum_{All\ Faces} (En_x + Fn_y + Gn_z)\Delta S - \left[q\vec{V}_G \cdot \vec{n}\Delta S \right]$$

$$= \left[\widehat{E}_{i+\frac{1}{2},j,k} - \widehat{E}_{i-\frac{1}{2},j,k} \right] + \left[\widehat{F}_{i,j+\frac{1}{2},k} - \widehat{F}_{i,j-\frac{1}{2},k} \right] + \left[\widehat{G}_{i,j,k+\frac{1}{2}} - \widehat{G}_{i,j,k-\frac{1}{2}} \right] \tag{3-6}$$

Where, $$\widehat{E}\Big|_{i\pm\frac{1}{2},j,k} = \left[En_x + Fn_y + Gn_z - q(\vec{V}_G \cdot \vec{n}) \right] \Delta S \Big|_{i\pm\frac{1}{2},j,k}$$

$$\widehat{F}\Big|_{i,j\pm\frac{1}{2},k} = \left[En_x + Fn_y + Gn_z - q(\vec{V}_G \cdot \vec{n}) \right] \Delta S \Big|_{i,j\pm\frac{1}{2},k} \tag{3-7}$$

$$\widehat{G}\Big|_{i,j,k\pm\frac{1}{2}} = \left[En_x + Fn_y + Gn_z - q(\vec{V}_G \cdot \vec{n})\right]\Delta S\Big|_{i,j,k\pm\frac{1}{2}}$$

The viscous fluxes (R_v , S_v, and T_v) on the right hand side are evaluated as follows:

$$\iint_s (R_v\vec{i} + S_v\vec{j} + T_v\vec{k})\cdot\vec{n}dS = \sum_{All\ Faces} (R_v n_x + S_v n_y + T_v n_z)\Delta S \tag{3-8}$$

The derivatives appearing in the viscous fluxes are computed by using central difference formulations. These are computed explicitly, using information available at a previous time level.

The inviscid fluxes, $\widehat{E}$, $\widehat{F}$, and $\widehat{G}$ are calculated implicitly using Roe's flux difference scheme[62-66] over a four-point stencil as shown in Figure 3.1. At a cell interface, the numerical flux f_{Num} (which is an approximation to $\widehat{E}$, $\widehat{F}$, or $\widehat{G}$) is given by:

$$f_{Num} = \left[\overbrace{\frac{1}{2}\left[f(q_L) + f(q_R)\right]}^{\text{Physical Flux Term}} - \overbrace{\frac{1}{2}\left[\left|\tilde{A}(q_L, q_R)\right|(q_R - q_L)\right]}^{\text{Artificial Viscosity Term}}\right]\Delta S \tag{3-9}$$

Where,

$$f(q_L) = \begin{bmatrix} \rho_L U_L \\ \rho_L U_L u_L + p_L n_x \\ \rho_L U_L v_L + p_L n_y \\ \rho_L U_L w_L + p_L n_z \\ U_L H_{0L} - p_L n_t \end{bmatrix} \quad , \quad f(q_R) = \begin{bmatrix} \rho_R U_R \\ \rho_R U_R u_R + p_R n_x \\ \rho_R U_R v_R + p_R n_y \\ \rho_R U_R w_R + p_R n_z \\ U_R H_{0R} - p_R n_t \end{bmatrix} \tag{3-10}$$

The subscripts L and U refer to the estimates of the flow properties to the left and right side of a cell, respectively.

Here, ΔS is the cell area of the face over which f_{Num} is evaluated. The quantities U and H_0 are the relative velocities normal to the cell face and total enthalpy, respectively. The quantity $\tilde{A}$ is defined as: $\tilde{A} = T|\Lambda|T^{-1}$, assuming that the original matrix is given by $A = \frac{\partial f}{\partial q} = T\Lambda T^{-1}$. Matrix T contains the eigenvectors of A, while Λ contains the eigenvalues. In Equation (3-10), the primitive variables q_L and q_R to the left and the right of the cell interfaces are defined as follows:

$$q_L = \begin{bmatrix} \rho_L \\ u_L \\ v_L \\ w_L \\ p_L \end{bmatrix}, \qquad q_R = \begin{bmatrix} \rho_R \\ u_R \\ v_R \\ w_R \\ p_R \end{bmatrix} \tag{3-11}$$

A four-point stencil, with Roe's Superbee limiter[65] to control the high frequency oscillations near shocks, is used to compute the left and right values of primitive variable vectors at each cell interface. For example, q_L and q_R at cell face $i+\frac{1}{2}$ can be written as follows:

$$\begin{aligned} q_L &= q_i + \frac{1}{6}\Phi^+_{i-\frac{1}{2}}(q_i - q_{i-1}) + \frac{1}{3}\Phi^-_{i+\frac{1}{2}}(q_{i+1} - q_i) \\ q_R &= q_{i+1} - \frac{1}{3}\Phi^+_{i+\frac{1}{2}}(q_{i+1} - q_i) - \frac{1}{6}\Phi^-_{i+\frac{3}{2}}(q_{i+2} - q_{i+1}) \end{aligned} \tag{3-12}$$

Where,

$$\Phi^{+}_{i-\frac{1}{2}} = \Phi(r^{+}_{i-\frac{1}{2}}), \quad \Phi^{-}_{i+\frac{1}{2}} = \Phi(r^{-}_{i+\frac{1}{2}})$$

$$r^{+}_{i-\frac{1}{2}} = \frac{q_{i+1} - q_i}{q_i - q_{i-1}} \quad , \quad r^{-}_{i+\frac{1}{2}} = \frac{q_i - q_{i-1}}{q_{i+1} - q_i} \tag{3-13}$$

$$\Phi(r) = \max\left[0, \min(2r, 1), \min(r, 2)\right]$$

The second term in Equation (3-9), using Liu and Vinokur[66] formula, can be expanded as:

$$\left|\tilde{A}(q_L, q_R)\right|(q_R - q_L) = \left|\tilde{\lambda}_1\right|\Delta q + \delta_1 \tilde{q}^{*} + \delta_2 N_n \tag{3-14}$$

Where,

$$\delta_1 = \left(-\left|\tilde{\lambda}_1\right| + \frac{\left|\tilde{\lambda}_2\right| + \left|\tilde{\lambda}_3\right|}{2}\right)\frac{\Delta p}{\tilde{a}^2} + \frac{\left|\tilde{\lambda}_2\right| - \left|\tilde{\lambda}_3\right|}{2}\frac{\tilde{\rho}\Delta U}{\tilde{a}} \tag{3-15}$$

$$\delta_2 = \left(-\left|\tilde{\lambda}_1\right| + \frac{\left|\tilde{\lambda}_2\right| + \left|\tilde{\lambda}_3\right|}{2}\right)\tilde{\rho}\Delta U + \frac{\left|\tilde{\lambda}_2\right| - \left|\tilde{\lambda}_3\right|}{2}\frac{\Delta p}{\tilde{a}} \tag{3-16}$$

$$\tilde{q}^{*} = \begin{bmatrix} \\ 1 \\ \tilde{u} \\ \tilde{v} \\ \tilde{w} \\ \dfrac{\tilde{H}_0}{\tilde{\rho}} \end{bmatrix} \quad , \quad N_n = \begin{bmatrix} 0 \\ n_x \\ n_y \\ n_z \\ \tilde{U} \end{bmatrix}\Delta S \tag{3-17}$$

And

$$\begin{aligned}\tilde{\lambda}_1 &= \tilde{U} \\ \tilde{\lambda}_2 &= \tilde{U} + \tilde{a} \\ \tilde{\lambda}_3 &= \tilde{U} - \tilde{a}\end{aligned} \tag{3-18}$$

In Equations (3-14) through (3-18), the "~" quantities are computed using Roe averaging as follows:

$$\begin{bmatrix}\tilde{\rho} \\ \tilde{u} \\ \tilde{v} \\ \tilde{w} \\ \tilde{H} \\ \tilde{U}\end{bmatrix} = \begin{bmatrix}\sqrt{\rho_L \rho_R} \\ \dfrac{\sqrt{\rho_L}u_L + \sqrt{\rho_R}u_R}{\sqrt{\rho_L} + \sqrt{\rho_R}} \\ \dfrac{\sqrt{\rho_L}v_L + \sqrt{\rho_R}v_R}{\sqrt{\rho_L} + \sqrt{\rho_R}} \\ \dfrac{\sqrt{\rho_L}w_L + \sqrt{\rho_R}w_R}{\sqrt{\rho_L} + \sqrt{\rho_R}} \\ \dfrac{\sqrt{\rho_L}H_L + \sqrt{\rho_R}H_R}{\sqrt{\rho_L} + \sqrt{\rho_R}} \\ (\tilde{u}\vec{i} + \tilde{v}\vec{j} + \tilde{w}\vec{k}) \cdot \vec{n} - \vec{V}_G \cdot \vec{n}\end{bmatrix} \tag{3-19}$$

In Equations (3-14) through (3-16), the difference Δ represents the change in the quantities across the cell interface (for example, $\Delta q = q_R - q_L$). In Equations (3-19), $\vec{V}_G$ is the grid velocity, as seen by a stationary observer.

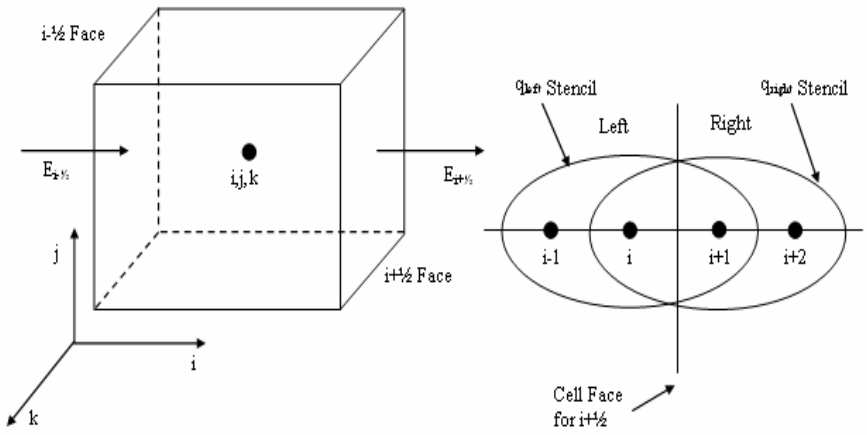

Figure 3.1: Cell centered finite volume formulation and four point stencil.

The spatially discretized Navier-Stokes equations (the semi-discrete form) lead to a set of ordinary differential equations for the flow properties. These are solved using a time marching scheme, subject to initial conditions with an appropriate set of boundary conditions, discussed in Section 3.4.

A first order two point backward difference is used to approximate the time derivative. The resulting system is given by:

$$\frac{(q\Delta V)_{i,j,k}^{n+1} - (q\Delta V)_{i,j,k}^{n}}{\Delta t} = -\sum_{All\ Faces} f_{Num}{}^{n+1}\Delta S - \sum_{All\ Faces} \left(Rn_x + Sn_y + Tn_z\right)^n \Delta S \tag{3-20}$$

Here "n" is the time level where the solution is known, and "n+1" is the next time level where the solution is sought. As stated earlier, the viscous terms are computed

explicitly at the known time level. This equation set is highly nonlinear and couples the finite volume cell (i, j, k) to its neighbors (i±1, j, k), (i, j±1, k), and (i, j, k±1). A non-iterative time marching scheme is used. All terms in Equation (3-20) are first expanded about known flow quantities at the time level "n":

$$\left(\sum_{All\ Faces} f_{Num}\Delta S\right)^{n+1} = \left(\sum_{All\ Faces} f_{Num}\Delta S)\right)^{n} + \sum_{All\ Faces} \frac{\partial f_{Num}}{\partial q}(q^{n+1} - q^{n})\Delta S \tag{3-21}$$

Carrying the unknown quantities to the left side:

$$\frac{(\Delta q)^n}{\Delta t}V + \sum \hat{A}(\Delta q)^n = -\left(\sum f_{Num}\Delta S\right)^n - \left(\sum (R_v n_x + S_v n_y + T_v n_z)\right)^n \tag{3-22}$$

Where $(\Delta q)^n = q^{n+1} - q^n$.

Finally, $(\Delta q)_{cell\ face}$ is defined as the average of (Δq) at all centers. This leads to a seven-diagonal system linking the (Δq) value at node (i, j, k) with its neighbors (i±1, j, k), (i, j±1, k), and (i, j, k±1). This system of linear equations is approximately solved by an incomplete lower-upper factorization scheme. The lower-upper block decomposition (LU-SGS) algorithm has been described in detail by Yoon et al.[67] The factorization leads to an error of order $(\Delta t)^3$. Details of the equations, the algorithm, and sample numerical calculations can be found in that report, as well as many CFD classical textbooks.

3.3 Turbulence Modeling

In most practical applications within turbomachinery, the Reynolds number is high and the flow is turbulent. The methodology followed in this work is a RANS (Reynolds Average Navier-Stokes System of equations) approach in which the time-averaged mean effects are resolved and the turbulence fluctuating effects are modeled. Time-averaging the equations gives rise to new terms, often referred to as the components of the Reynolds stress tensor, that are additional unknowns and must be appropriately modeled to close the system of governing equations ("closure problem"). As mentioned in the previous chapter, several turbulence closure models exist in CFD, most of which differ in the type, number, and complexity of additional equations to be solved.

The RANS approach used in this work account for the turbulent effects by following Boussinesq's assumption and replacing the laminar viscosity (μ) with ($\mu + \mu_t$), where μ_t is the eddy viscosity. The laminar viscosity (μ) is a fluid property, while the eddy viscosity (μ_t) is a flow property that is determined by solving turbulence closure models. Those models can be divided according to the number of additional equations used in the estimation of the flow field eddy viscosity. The turbulence closure models implemented and studied in the current work fall within the two-equation models category and are described in the following sections.

3.3.1 Menter's k-ω-SST model:

Menter's k-ω-SST model[35] solves the two equations for k (turbulent kinetic energy) and ω (turbulent dissipation rate). Menter[35] developed the k-ω-SST model to combine the advantages found in Wilcox's k-ω model[34] and the advantages found in the k-ε model.[33]

Near the walls, k-ω-SST model solves the k-ω equations that do not require any near wall damping functions as required in the k-ε model. Away from walls, the k-ω-SST model solves the k-ε equations which do not suffer from the free stream dependency found in the k-ω model. This is done by transforming the k-ε model equations into a k-ω formulation with an additional cross-diffusion term not found in the original k-ω formulation. The blending between original k-ω formulation and the transformed k- ε formulation is done by multiplying the original k-ω equations by a function F_1 and multiplying the transformed k- ε equations by a function $(1\text{-}F_1)$. The function F_1 is designed to be unity near walls and zero away from walls. The "SST" refers to "Shear Stress Transport" which assumes that the shear stress is proportional to the turbulent kinetic energy in boundary layer flows. The k-ω-SST model[35] equations are as follows:

$$\frac{\partial \rho k}{\partial t}+\frac{\partial \rho u_i k}{\partial x_j}=\underbrace{\tau_{ij}\frac{\partial u_i}{\partial x_j}}_{\text{Production term}}-\underbrace{\frac{k^{\frac{3}{2}}}{l}}_{\text{Dissipation term}}+\underbrace{\frac{\partial}{\partial x_j}\left[(\mu+\frac{\mu_t}{\sigma_k})\frac{\partial k}{\partial x_j}\right]}_{\text{Diffusion term}} \tag{3-23}$$

$$\frac{\partial \rho \omega}{\partial t}+\frac{\partial \rho u_i \omega}{\partial x_j}=\overbrace{\frac{\gamma}{\upsilon_t}\tau_{ij}\frac{\partial u_i}{\partial x_j}}-\overbrace{\beta\rho\omega^2}+\overbrace{\frac{\partial}{\partial x_j}\left[(\mu+\frac{\mu_t}{\sigma_\omega})\frac{\partial \omega}{\partial x_j}\right]}+\underbrace{2(1-F_1)\rho\sigma_{\omega 2}\frac{1}{\omega}\frac{\partial k}{\partial x_j}\frac{\partial \omega}{\partial x_j}}_{\text{Cross-diffusion term}} \tag{3-24}$$

The length scale is computed from:

$$l=\frac{\sqrt{k}}{\beta^*\omega} \tag{3-25}$$

The model constants (φ) are computed from two related quantities (φ_1 and φ_2) as follows:

$$\varphi=F_1*\varphi_{1+}(1-F_1)*\varphi_2 \tag{3-26}$$

The quantity φ_1 is computed using:

$$\sigma_{k1}=1/0.85,\ \sigma_{\omega 1}=1/0.5,\ \beta_1=0.075$$
$$\beta^*=0.09,\ \kappa=0.41,\ \gamma_1=\frac{\beta_1}{\beta^*}-\frac{\kappa^2}{\sigma_{\omega 1}\sqrt{\beta^*}} \tag{3-27}$$

The quantity φ_2 is computed, likewise, using:

$$\sigma_{k2}=1.0,\ \sigma_{\omega 2}=1/0.856,\ \beta_2=0.0828$$
$$\beta^*=0.09,\ \kappa=0.41,\ \gamma_2=\frac{\beta_2}{\beta^*}-\frac{\kappa^2}{\sigma_{\omega 2}\sqrt{\beta^*}} \tag{3-28}$$

The function F_1 used in blending the original k-ω formulation and the transformed k-ε formulation is computed from:

$$F_1=\tanh\left(\left(\min\left[\max\left[\frac{2\sqrt{k}}{\beta^*\omega y};\frac{500\nu}{y^2\omega}\right];\frac{4\rho\sigma_{\omega 2}k}{CD_{k\omega}y^2}\right]\right)^4\right) \tag{3-29}$$

The function F_1 is designed to be one in the near wall region and transitions to zero away from the wall. Here, y is the distance to the nearest wall and CD_{kw} is the positive portion of the cross-diffusion term of Eq. (3-41):

$$CD_{k\omega}=\max\left[2\rho\sigma_{\omega 2}\frac{1}{\omega}\frac{\partial k}{\partial x_j}\frac{\partial \omega}{\partial x_j};10^{-20}\right] \tag{3-30}$$

The eddy viscosity is computed from:

$$\mu_t=\frac{a_1\rho k}{\max(a_1\omega;\Omega F_2)} \tag{3-31}$$

Where $a_1 = 0.31$. This formulation of the eddy viscosity ensures that the shear stress in boundary layer flows is proportional to the turbulent kinetic energy (where function F_2 takes the value of one); however, this does not hold for free shear layer flows (where function F_2 takes the value of zero). The function F_2 takes the form:

$$F_2 = \tanh\left(\left(\max\left[\frac{2\sqrt{k}}{\beta^* \omega y}; \frac{500\nu}{y^2 \omega}\right]\right)^2\right) \tag{3-32}$$

3.3.2 Kinetic Eddy Simulation (KES) model:

The Kinetic Eddy Simulation (KES) model was developed by Fang and Menon[49, 50] for the Large Eddy Simulation (LES) of wall-bounded turbulent flow at high Reynolds numbers. In LES, the contribution of large energy containing structures and all scales larger than the grid resolution to momentum and energy transfer is computed, and the effect of sub-grid unresolved small scales is modeled. The KES approach solves for both sub-grid kinetic energy (k) and sub-grid length scales (l). The KES model does not depend on non-physical parameters like grid spacing (Δ) to determine the length scales of the turbulent eddies. In the case where the computed sub-grid length scales (l) are close to the local grid spacing (Δ), KES approaches LES; however, when the computed sub-grid length scales (l) are much larger than the local grid spacing (Δ), KES smoothly transitions from LES to Very Large Eddy Simulation (VLES) in which only the very largest scales are resolved. The transition between the LES and VLES takes place as a part of the solution and is not pre-determined. Therefore, this approach can be considered as a VLES-LES approach. The KES model[49,50] solves two transport equations in k and kl as follows:

$$\frac{\partial \rho k}{\partial t}+\frac{\partial \rho u_i k}{\partial x_j} = \underbrace{\tau_{ij}\frac{\partial u_i}{\partial x_j}}_{\text{Production term}} - \underbrace{C_k \rho \frac{k^{\frac{3}{2}}}{l}}_{\text{Dissipation term}} + \underbrace{\frac{\partial}{\partial x_j}\left[(\mu+\frac{\mu_t}{\sigma_k})\frac{\partial k}{\partial x_j}\right]}_{\text{Diffusion term}} \tag{3-33}$$

$$\frac{\partial \rho (kl)}{\partial t}+\frac{\partial \rho u_i (kl)}{\partial x_j} = \overbrace{C_l l \tau_{ij}\frac{\partial u_i}{\partial x_j}} - \overbrace{C_{kl}\rho k^{\frac{3}{2}}} + \overbrace{\frac{\partial}{\partial x_j}\left[(\mu+\frac{\mu_t}{\sigma_{kl}})\frac{\partial (kl)}{\partial x_j}\right]} \tag{3-34}$$

The model constants used in this work are:

$$\begin{aligned}&\sigma_k = 0.9, C_k = 0.916\\ &\sigma_{kl} = 1/0.5, C_l = 1.06\end{aligned} \tag{3-35}$$

The turbulent viscosity is computed from:

$$\mu_t = C_\upsilon \rho \sqrt{k} l \tag{3-36}$$

The dissipation coefficient of (kl) depends on the length scale gradient as follows:

$$C_{kl} = 0.58 + 2\frac{C_\upsilon}{\sigma_{kl}}\left(\frac{\partial l}{\partial x_j}\right)^2 \tag{3-37}$$

C_υ is computed following the realizability constraints[50] based on the ratio of turbulent time ($t = l/\sqrt{k}$) scale to a shear time scale ($t = 1.0/\sqrt{\left(S_{ij}S_{ij}-\frac{1}{3}S_{kk}^2\right)}$) to prevent the over prediction of turbulent viscosity in the regions where strong velocity gradients exist as follows:

$$C_\upsilon = \min[0.0667; \frac{1}{\sqrt{6}}\frac{(\sqrt{k}/l)}{\sqrt{S_{ij}S_{ij}-\frac{1}{3}S_{kk}^2}}] \tag{3-38}$$

3.3.3 Hybrid RANS/KES (HRKES) model:

As mentioned in the previous chapter, all of the existing DES and HRLES approaches use a one-equation model in the free shear layers to estimate the velocity scales associated with turbulent eddies, while the length scale is estimated based on the local grid spacing. Therefore, the transition between RANS and LES regions may depend entirely on the grid spacing and it is not correlated with the local flow properties. This approach might not be suitable in predicting the turbulence length scales in the separated flow regions far from walls. To address this drawback, a new advanced turbulence model called hybrid RANS/KES (HRKES) turbulence model has been developed and implemented in the current work. This model solves Menter's k-ω-SST[35] model near walls and switches to the KES[49,50] model (which solves for both velocity and length scales) away from walls. By using the KES model away from the walls, the grid spacing dependency of the length scales found in other DES and HRLES models is eliminated.

Furthermore, KES requires using a "law of the wall" type approach that requires specifying (k) and (l) at the first grid point off the wall. These ad-hoc values of (k) and (l) at the first grid point off the wall are derived from the analyses of the energy dissipation rate on the wall for attached flows, which might not be suitable for large separated flows, or for transonic flows. In the HRKES model, the need to specify (k) and (l) is avoided by solving the classical k-ω-SST[35] model equations in near-wall regions while the KES[49,50] model equations are solved away from walls. This approach provides boundary conditions for both (k) and (l) and eliminates the need for any ad hoc

specification of their values at the first grid point off the wall, leading to a more robust formulation, compared to using KES everywhere.

In earlier DES and HRLES approaches, a common difficulty is in determining when and where to switch between near-wall RANS approaches (k-ω or SA) to LES approaches away from walls. In all of the aforementioned DES and HRLES approaches, researchers have used a combination of distance from the wall and grid spacing to switch between these two approaches. As a part of the current work, the assumption that (k) and (l) are continuous functions is invoked and these quantities are blended from the two approaches using two different blending functions.

In the KES model, as in other LES models, the eddy viscosity is proportional to the product of velocity scale (k) and length scale (Δ in the early LES models, l in the KES model). The constant of proportionality is often specified empirically. In the present study, numerical simulations have been done to estimate and bound this constant using realizability constraints.[50]

This section presents the blended k-ω-SST and KES model equations implemented and studied in this work.[68] The present HRKES turbulent kinetic energy equation is formulated as follows. In the region close to the wall, Menter's k-ω-SST equations[35] are solved as follows:

$$\frac{\partial \rho k}{\partial t}+\frac{\partial \rho u_i k}{\partial x_j}=\underbrace{\tau_{ij}\frac{\partial u_i}{\partial x_j}}_{\text{Production term}}-\underbrace{\frac{k^{\frac{3}{2}}}{l}}_{\text{Dissipation term}}+\underbrace{\frac{\partial}{\partial x_j}\left[(\mu+\frac{\mu_t}{\sigma_k})\frac{\partial k}{\partial x_j}\right]}_{\text{Diffusion term}} \tag{3-39}$$

$$\frac{\partial \rho \omega}{\partial t}+\frac{\partial \rho u_i \omega}{\partial x_j}=\overbrace{\frac{\gamma}{\upsilon_t}\tau_{ij}\frac{\partial u_i}{\partial x_j}}-\overbrace{\beta\rho\omega^2}+\overbrace{\frac{\partial}{\partial x_j}\left[(\mu+\frac{\mu_t}{\sigma_\omega})\frac{\partial \omega}{\partial x_j}\right]}+\underbrace{2(1-F_1)\rho\sigma_{\omega 2}\frac{1}{\omega}\frac{\partial k}{\partial x_j}\frac{\partial \omega}{\partial x_j}}_{\text{Cross-diffusion term}} \tag{3-40}$$

In the outer region, the (k) equation is solved as before, and the (ω) equation is replaced by the (kl) equation from the KES model[49,50] as follows:

$$\frac{\partial \rho (kl)}{\partial t}+\frac{\partial \rho u_i (kl)}{\partial x_j}=\underbrace{C_l l\tau_{ij}\frac{\partial u_i}{\partial x_j}}_{\text{Production term}}-\underbrace{C_{kl}\rho k^{\frac{3}{2}}}_{\text{Dissipation term}}+\underbrace{\frac{\partial}{\partial x_j}\left[(\mu+\frac{\mu_t}{\sigma_{kl}})\frac{\partial (kl)}{\partial x_j}\right]}_{\text{Diffusion term}} \tag{3-41}$$

In order to avoid abrupt jumps in the values of (l) between near-wall regions and the outer layer, the following blending is used in computing the HRKES length scale:

$$\begin{aligned} l &= F_{blend}.l_{k-\omega-SST}+(1-F_{blend}).l_{KES} \\ l_{k-\omega-SST} &= \frac{\sqrt{k}}{\beta^*\omega} \\ l_{KES} &\rightarrow \text{Eq.(3-58)} \end{aligned} \tag{3-42}$$

The HRKES model constants are computed from k-ω-SST[35] and KES[49,50] model constants as follows:

$$
\begin{aligned}
\sigma_k &= F_{blend}.[\sigma_{k_1}.F_1 + \sigma_{k_2}.(1-F_1)] + (1-F_{blend}).\sigma_{k_3} \\
\sigma_\omega &= \sigma_{\omega_1}.F_1 + \sigma_{\omega_2}.(1-F_1) \\
\beta &= \beta.F_1 + \beta.(1-F_1) \\
\gamma &= \gamma_1.F_1 + \gamma_2.(1-F_1)
\end{aligned}
\tag{3-43}
$$

Where,

$$
\begin{aligned}
&\sigma_{k_1} = 1/0.85, \sigma_{\omega_1} = 2.0, \beta_1 = 0.075, \beta^* = 0.09 \\
&\sigma_{k_2} = 1.0, \sigma_{\omega_2} = 1/0.856, \beta_2 = 0.0828 \\
&\sigma_{k_3} = 0.9, \sigma_{kl} = 2.0, C_l = 1.06, \kappa = 0.41 \\
&\gamma_1 = \frac{\beta_1}{\beta^*} - \frac{\kappa^2}{\sigma_{\omega_1}\sqrt{\beta^*}}, \gamma_2 = \frac{\beta_2}{\beta^*} - \frac{\kappa^2}{\sigma_{\omega_2}\sqrt{\beta^*}}
\end{aligned}
\tag{3-44}
$$

The functions F_1, F_2, C_{kl}, and C_υ are calculated as before in Eq.(3-29), Eq.(3-32), Eq.(3-37), and Eq.(3-38), respectively.

Finally, the turbulent viscosity is computed from:

$$
\begin{aligned}
\mu_t &= F_{blend}\mu_t\big|_{k-\omega-SST} + (1-F_{blend})\mu_t\big|_{KES} \\
\mu_t\big|_{k-\omega-SST} &= \frac{a_1\rho k}{\max(a_1\omega;\Omega F_2)} \\
\mu_t\big|_{KES} &= C_\upsilon \rho\sqrt{k} l_{KES}
\end{aligned}
\tag{3-45}
$$

The blending functions (F_{blend}) evaluated in the HRKES model are Menter's k-ω-SST[35] F_1 and F_2 functions (Eq. (3-29), Eq. (3-32), respectively). Those distance-dependent blending functions are chosen to insure a smooth transition between the RANS formulation in near-wall regions and the LES formulation away from walls. In the current work, four different options (Table 3.1) for the HRKES model (a combination of F_1 and F_2 blending functions and the use of realizability constraints to bound the KES model

parameters) have been coded, studied and compared to the classical k-ω-SST turbulence model.

Table 3.1: Different HRKES options

Type	C_v	F_{blend}
HRKES1	0.0667	F_2 (Eq.(3-32))
HRKES2	Eq.(3-38)	F_2 (Eq.(3-32))
HRKES3	0.0667	F_1 (Eq.(3-29))
HRKES4	Eq.(3-38)	F_1 (Eq.(3-29))

3.4 Initial and Boundary Conditions

Navier-Stokes equations are parabolic in time and elliptic in space. Thus, they require a physical set of initial and boundary conditions for the numerical solution to be advanced and for a stable solution to be achieved. In this section, the initial and boundary conditions used in the current methodology are presented.

At the beginning of the calculations, the flow properties everywhere in the system are assumed to be uniform (cold start). The analysis can also use a previously stored solution file with a corresponding grid file, to restart the computations.

The early version of GT-TURBO3D had the capability of dealing with H-grids only. However as a part of the current work, a C-grid capability has been added to GTTURBO3D in which the boundary conditions subroutines are modified to deal with C-grids (Figure 3.2). The following boundary conditions have been used in the current analysis:

3.4.1 Inflow Boundary Condition:

At this boundary, the stagnation temperature, T_0, the total pressure, P_0, and the tangential components of velocity are assumed to be known. The fifth equation applied at the inlet boundary condition is the one-dimensional Riemann characteristic equation, for the quantity $(\frac{2a}{\gamma-1}-\vec{V}.\vec{n})$, which allows the acoustic disturbances to leave the computational field through the inlet face. The turbulence inflow boundary conditions are set as follows[35]:

$$\begin{aligned} \nu_{t\infty} &= 10^{-3}\nu \\ \omega_\infty &= (1 \to 10)\frac{a_\infty}{L} \\ k_\infty &= \nu_{t\infty}\omega_\infty \end{aligned} \tag{3-46}$$

3.4.2 Outflow Boundary Condition:

Two different outflow boundary conditions exist in the current analysis. The first outflow boundary condition is to specify the exit static pressure. In the second approach, the exit static pressure is iteratively adjusted until the prescribed mass flow rate is achieved. All other quantities such as the density, the three components of velocity, and turbulence quantities are extrapolated from the interior of the domain. The downstream boundary is far enough downstream and does not require non-reflective boundary conditions.

3.4.3 Solid Walls Boundary Condition:

At solid walls, a no slip boundary condition is used. For stationery walls, the velocity is set to zero, while for moving walls, the velocity is set equal to $\vec{\Omega}\times\vec{r}$. The temperature

values at the solid surfaces are directly extrapolated from the interior flow field assuming an adiabatic wall boundary condition. The pressure is found by solving the momentum equation in the normal direction to the blade surfaces, as described by Pulliam et al.[69] The density values are found from the equation of state after temperature and pressure are computed. The turbulence wall boundary conditions are set as follows[35] :

$$\begin{aligned} \nu_t &= 0.0 \\ k &= 0.0 \\ \omega &= \frac{60\mu}{\beta_1 \rho y^2} \end{aligned} \tag{3-47}$$

Where, y is the distance to the first grid point off the wall and β_1=0.075.

3.4.4 Cutout and Periodic Boundary Conditions:

The cutout and blade-to-blade periodic boundaries are similar in the sense that the flow properties are averaged on either side of the boundary to compute the interface value. The cutout boundary condition is used with C-grids in which density, momentum and energy are averaged directly along the cutout interface. The blade-to-blade periodic boundary condition is used with both H-grids and C-grids to account for the neighboring blade passages. In the periodic boundary condition the direct averaging only holds for density, energy, and axial velocity. The remaining two velocity components in y- and z-directions are converted into radial and azimuthal components on either side of the interface before they are averaged. After the interface values are computed, the radial and azimuthal velocity components are converted back to Cartesian velocity components.

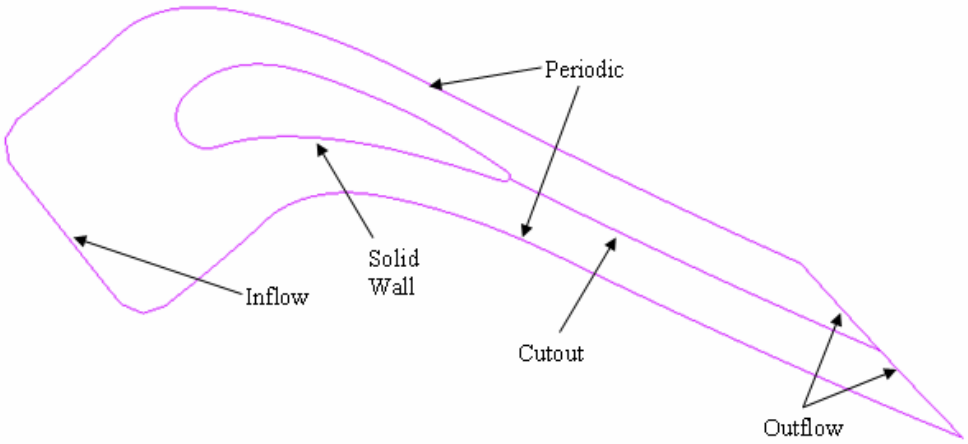

a) C-grid boundary conditions

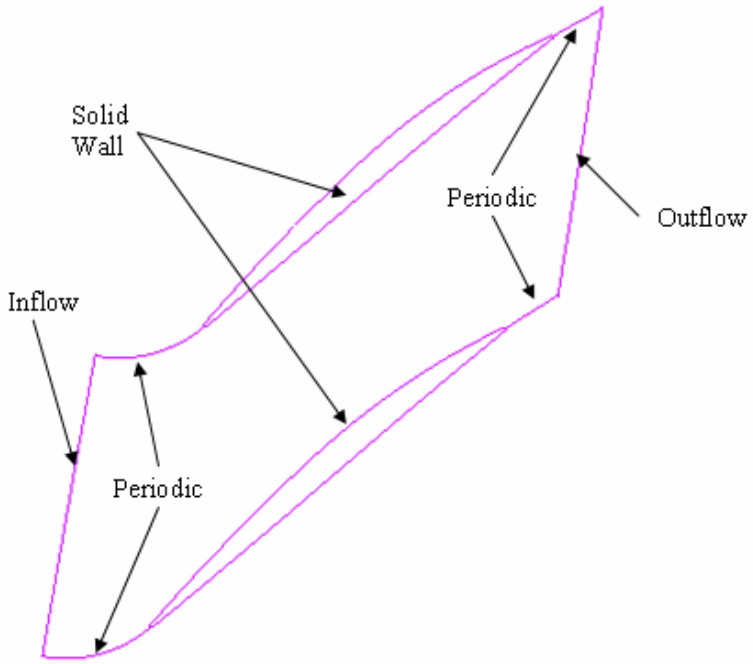

b) H-grid boundary conditions

Figure 3.2: Boundary conditions.

3.4.5 Multi-stage Interface Boundary Conditions:

As mentioned before, when simulating the flow field through multiple blade rows, one major difficulty is the relative motion between the rotor and stator blades. A proper set of stable and accurate boundary conditions must be used at the rotor-stator interface to conserve local and global fluxes.

In the current analysis, two different approaches are used to transfer the flow field variables (density, energy, and three momentum components) across the rotor-stator interface. The first is the averaging plane (AP) approach, and the second is the unsteady sliding mesh (USM) approach. In the following sections, the rotor-stator interface boundary conditions used in the current work are described.

3.4.5.1 Averaging Plane (AP) Approach:

Within this approach, five different sets[70] of averaging plane boundary conditions have been implemented and studied. In all these approaches, the starting point is the mixed out averaging.[59] In the mixed out averaging approach, at each radial location, for a strip of the interface as shown in Figure 3.3, the mass, momentum, and energy fluxes on both sides of the interface are first computed using the information available from the upstream and downstream blocks.

$$\begin{Bmatrix} I_1 \\ I_2 \\ I_3 \\ I_4 \\ I_5 \end{Bmatrix} = \begin{Bmatrix} \iint \rho v_n dA \\ \iint \rho u v_n dA + \iint p\vec{i} \bullet \vec{n} dA \\ \iint \rho v v_n dA + \iint p\vec{j} \bullet \vec{n} dA \\ \iint \rho w v_n dA + \iint p\vec{k} \bullet \vec{n} dA \\ \iint \rho h_0 v_n dA \end{Bmatrix} \tag{3-48}$$

Here u,v,w are the velocity components with unit vectors $\vec{i}, \vec{j}, \vec{k}$ in the axial, azimuthal, and radial directions, respectively. The vector $\vec{n}$ is normal to the interface surface which in general may be curved. From these integrated values, the average values of pressure, density, and the three velocity components are next extracted. These are five non-linear equations linking the desired average properties, but may be easily ordered so that they may be solved without iterations. The detailed description of how the individual velocity, density, and pressure components are computed is found in (Ref. 60, 71, 72).

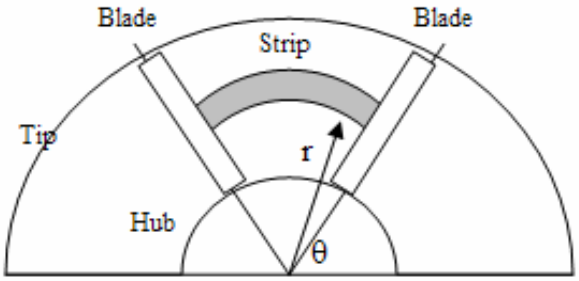

Figure 3.3: Radial strip from blade to blade at the interface boundary condition.

Consider two blocks. The upstream block is the stator and the downstream block is the rotor. The interest is in the flow properties at the stator boundary AB and the rotor boundary CD as shown in Figure 3.4.

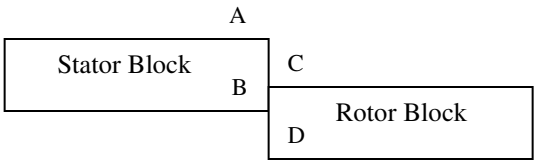

Figure 3.4: Interface boundary condition between the stator and rotor blocks.

In describing the boundary conditions, for simplicity, it is assumed that the first block consists of stator blades and the second block consists of rotor blades and that the blade to blade periodicity exists within the stator block and the rotor block, although the number of blades is allowed to be different in each row. It is also assumed that the flow is locally subsonic. The analysis, off course, does not use these simplifying assumptions.

3.4.5.1.1 IBC1 Approach:

In this approach, the interface boundary is treated as an inflow / outflow boundary. The azimuthally averaged pressure from the downstream block is prescribed as an outflow pressure boundary condition for the upstream block (for axially subsonic flow), while other properties (normal velocity, two tangential components of velocity, density) are prescribed from the interior of the domain as the averaged values. For the downstream block, the averaged velocities and density values are prescribed from the upstream block as an inflow boundary conditions and the azimuthally averaged pressure is prescribed from the interior of the domain (for axially subsonic flow). This is shown in Table 3.2 and in Figure 3.5, with subscripts "S" and "R" referring to the stator and rotor, respectively, and "$\bar{}$" referring to the azimuthally averaged values.

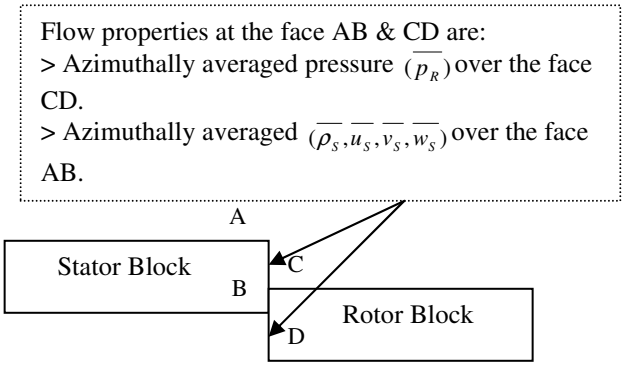

Figure 3.5: IBC1 interface boundary condition between the stator and rotor blocks.

Table 3.2: IBC1 interface boundary condition.

IBC1	Outflow (Stator Block) Face AB	Inflow (Rotor Block) Face CD
Number of B.C. using information from the other block.	1 $(\overline{p_R})$	4 $(\overline{\rho_S}, \overline{u_S}, \overline{v_S}, \overline{w_S})$
Number of B.C. using information from the same block.	4 $(\overline{\rho_S}, \overline{u_S}, \overline{v_S}, \overline{w_S})$	1 $(\overline{p_R})$

3.4.5.1.2 IBC2 Approach:

In this approach, the rotor inlet face CD of the downstream block is treated exactly as in IBC1 in which the averaged velocities and density values are prescribed from the upstream block (stator block) as an inflow boundary conditions and the azimuthally averaged pressure is prescribed from inside the domain (for axially subsonic flow). For the stator exit face AB, the pressure is specified as in IBC1 in which the azimuthally averaged pressure from the rotor block is prescribed as an outflow pressure

boundary condition but the local instantaneous values of density, the normal velocity, and the two tangential components of velocity are extrapolated from the interior of the domain instead of using the averaged values. The IBC2 approach is shown in Table 3.3 and in Figure 3.6.

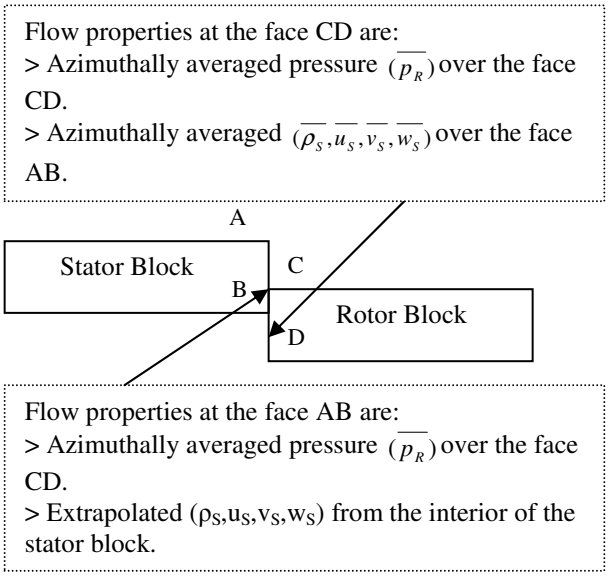

Figure 3.6: IBC2 interface boundary condition between the stator and rotor blocks.

Table 3.3: IBC2 interface boundary condition.

IBC2	Outflow (Stator Block) Face AB	Inflow (Rotor Block) Face CD
Number of B.C. using information from the other block.	1 $(\overline{p_R})$	4 $(\overline{\rho_S}, \overline{u_S}, \overline{v_S}, \overline{w_S})$
Number of B.C. using information from the same block.	4 (ρ_S, u_S, v_S, w_S)	1 $(\overline{p_R})$

3.4.5.1.3 IBC3 Approach:

In this approach, the averaged values from the downstream block are prescribed as the boundary conditions for the upstream block, and the averaged values from the upstream block are prescribed as the boundary conditions for the downstream block. The IBC3 approach is shown in Table 3.4 and in Figure 3.7.

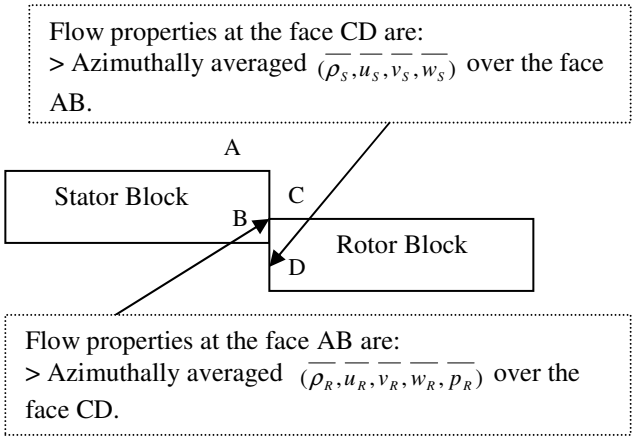

Figure 3.7: IBC3 interface boundary condition between the stator and rotor blocks.

Table 3.4: IBC3 interface boundary condition.

IBC3	Outflow (Stator Block) Face AB	Inflow (Rotor Block) Face CD
The flow variables at the interface B.C.	$\left(\overline{\rho_R}, \overline{u_R}, \overline{v_R}, \overline{w_R}, \overline{p_R}\right)$	$\left(\overline{\rho_S}, \overline{u_S}, \overline{v_S}, \overline{w_S}, \overline{p_S}\right)$

3.4.5.1.4 IBC4 Approach:

In this approach, the azimuthally averaged properties at each radial location (from the stator and rotor) are arithmetically averaged and prescribed as boundary conditions at

both the stator downstream face AB and the rotor upstream face CD. The IBC4 approach is shown in Table 3.5 and in Figure 3.8.

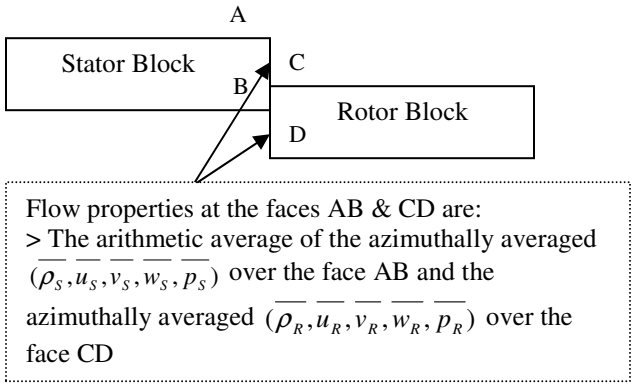

Figure 3.8: IBC4 interface boundary condition between the stator and rotor blocks.

Table 3.5: IBC4 interface boundary condition.

IBC4	Outflow (Stator Block) Face AB	Inflow (Rotor Block) Face CD
The flow variables at the interface B.C.	$\frac{1}{2}\begin{pmatrix} \overline{\rho_S}+\overline{\rho_R} \\ \overline{u_S}+\overline{u_R} \\ \overline{v_S}+\overline{v_R} \\ \overline{w_S}+\overline{w_R} \\ \overline{p_S}+\overline{p_R} \end{pmatrix}$	$\frac{1}{2}\begin{pmatrix} \overline{\rho_S}+\overline{\rho_R} \\ \overline{u_S}+\overline{u_R} \\ \overline{v_S}+\overline{v_R} \\ \overline{w_S}+\overline{w_R} \\ \overline{p_S}+\overline{p_R} \end{pmatrix}$

3.4.5.1.5 IBC5: Characteristic Boundary Condition Approach:

The mixed out averaged quantities calculated are used in a non-reflective characteristic boundary condition approach proposed by Giles[72] and used by Chima[71] and others. Giles[72] constructed a set of non-reflecting boundary conditions based on the linearized form of Euler equations written in terms of perturbations of primitive variables about the average flow from the neighboring blade row. Substituting wave like solutions into the flow governing equations and circumferentially decomposing the solutions into its Fourier modes in which the computed zeroth mode corresponds to the mean flow and

is treated following one-dimensional characteristic theory. This leads to a set of five equations in the perturbed values of the density, pressure, and three velocity components at the interface boundary and allows specification of the average changes in characteristic variables at the interface boundary. The IBC5 approach is shown in Table 3.6, where C_5 is the characteristic variable corresponding to an upstream running pressure wave. Complete details of this boundary condition can be found in Ref. (71, 72).

Table 3.6: IBC5 interface boundary condition.

Outflow (Stator Block) Face AB	$\rho = \rho_S$ $u = u_S$ $v = v_S$ $w = w_S$ $p = \frac{1}{2}[\overline{p_R} + p_S + \overline{\rho_R}.\overline{a_R}.(u_S - \overline{u_R})]$
Inflow (Rotor Block) Face CD	$C_{5R} = -\overline{\rho_S}.\overline{a_S}.(u_R - \overline{u_S}) + (p_R - \overline{p_S})$ $\rho = \overline{\rho_S} + \frac{C_{5R}}{2\overline{a_S^2}}$ $u = \overline{u_S} - \frac{C_{5R}}{2\overline{\rho_S}.\overline{a_S}}$ $v = \overline{v_S}$ $w = \overline{w_S}$ $p = \overline{p_S} + \frac{1}{2}.C_{5R}$

3.4.5.2 Unsteady Sliding Mesh (USM) Approach:

In the previous section, the averaging plane approach was described, in which the starting point is the averaging of the flow field variables over radial strips at the interface boundary conditions. This averaging process smears out the blade to blade details of the

flow field and will preclude the proper transfer of locally separated pockets of flow between stages, preventing the use of these approaches from accurately modeling the spatial propagation of wakes and stall cells between stages. To overcome these limitations, full unsteady approaches[61] (unsteady sliding mesh) should be used. In the unsteady sliding mesh approach, interpolation takes place at the interface boundary between the successive blade rows to ensure the continuity of the flow variables across the interface.

The interpolation process should ensure that the flow properties at any mesh point at a certain radial and azimuthal location on one side of the interface should be equal to the ghost point on the other side of the interface. The interpolation process should also ensure the conservation of the mass, momentum and energy fluxes across the interface. In the current work, an unsteady sliding mesh interface boundary condition is implemented and studied. At each time step, the flow variables at the interface boundary are rotated and a first order interpolation with cell face area weighting is used. The USM approach is shown in Figure 3.9.

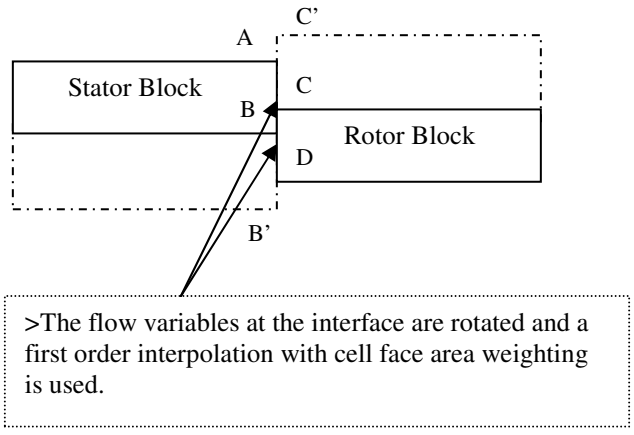

Figure 3.9: Unsteady sliding mesh interface boundary condition between the stator and rotor blocks.

CHAPTER 4

VALIDATION STUDIES

As stated earlier, the present analysis (GT-TURBO3D) was built for earlier studies[62,63] and has been extensively validated for helicopter rotors, wind turbines, prop-fans, fixed wing configurations, and single-stage axial and radial compressor configurations (NASA Rotor 37, NASA Rotor 67, NASA low speed centrifugal compressor, etc)[73-76] using the S-A one equation turbulence model. The code validation studies and grid convergence studies are documented in the afore-mentioned references and are not reproduced here for brevity.

A variety of two-equation turbulence models have been implemented in GT-TURBO3D and studied. Also, a local time stepping capability, a C-grid capability, and several multi-stage interface boundary conditions have been implemented in GT-TURBO3D.

As a further validation of the turbulence models implemented in this analysis,[68] this solver is evaluated for several airfoils (RAE2822 and NACA0015), an axial turbine configuration, and an axial compressor configuration. Also, several rotor-stator interface boundary conditions have been systematically studied.[70]

4.1 RAE2822 Airfoil

The present methodology is applied to a transonic flow over a RAE2822 airfoil. This test case corresponds to test case 10 by Cook et al.[77] This AGARD standard case is selected because the shock wave is strong enough to induce a boundary layer separation

over the airfoil surface. The flow conditions are as follows: Mach number of 0.75, Reynolds number of 6.2 million, and a corrected angle of attack of 2.72°. This case is simulated using GT-TURBO3D with periodic boundary conditions in the span-wise direction. The grid used in the current computations is a C-grid, which extends 20 chord lengths in all directions. This grid consists of 257 cells in the direction wrapping the airfoil (with 176 cells on the airfoil surface), 97 cells in the normal direction ($y^+ \sim 1$), and 5 cells in the span direction (Figure 4.1).

The flow field around the airfoil is examined through a study of the Mach number contours for all the turbulence models studied. The computed Mach number contours are shown in Figure 4.2. All the turbulence models are able to capture the shock wave location and the boundary layer separation caused by the shock wave over the airfoil surface. The smooth Mach number contours indicate that the blending in the HRKES model does not introduce any unphysical fluctuations to the flow field in the buffer zone.

Next, the details of the flow over the airfoil are examined through a comparison of pressure coefficient, C_p, distributions over the airfoil surface with experimental[77] data. The computed pressure coefficient distributions are shown in Figure 4.3. The computations agree well with the experimental[77] data. It is found that the outer region model has an effect on the near-wall model. It is also found that the k-ω-SST, HRKES1, and HRKES2 models predict the shock wave location accurately, while the HRKES3 and HRKES4 models predict the shock wave location to be slightly downstream. Furthermore, the solutions with or without using realizability constraints are almost identical. This indicates that realizability constraints have a minor role in the current

HRKES model. Then, the skin friction coefficient, C_f, distribution over the airfoil is compared with experimental[77] data as shown in Figure 4.4 with a good agreement.

To assess the grid independency of the current methodology, a limited grid independency study is done for this configuration using the HRKES2 turbulence model. A fine C-grid with 257 cells in the direction wrapping the airfoil (with 176 cells on the airfoil surface), 194 cells in the normal direction, and 5 cells in the span direction is also used in this study. Figure 4.5 shows the computed pressure coefficient and skin friction coefficient distributions over the airfoil surface for the medium grid (257*97*5) and the fine grid (257*194*5); the computed values are similar for both grids. The Mach number contours are also similar and are not shown here for brevity.

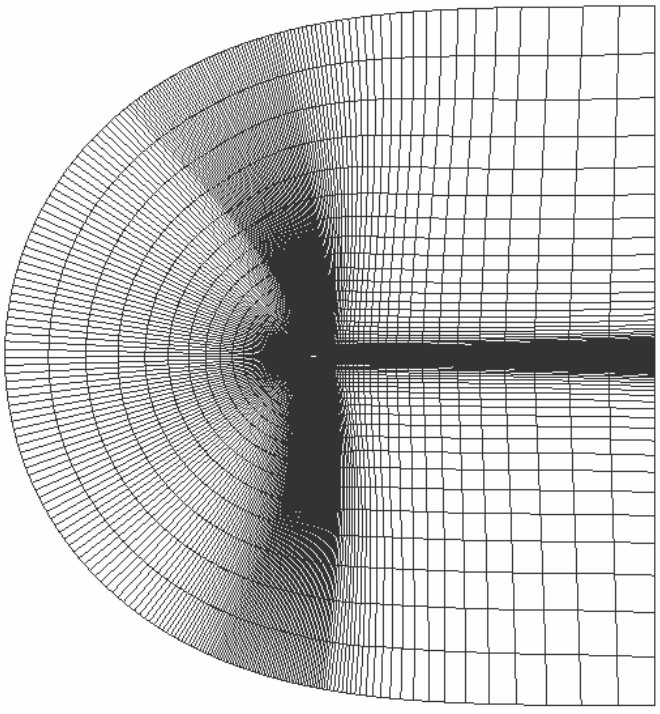

a) Far-field grid.

Figure 4.1: RAE2822 airfoil (257x97x5) C-grid.

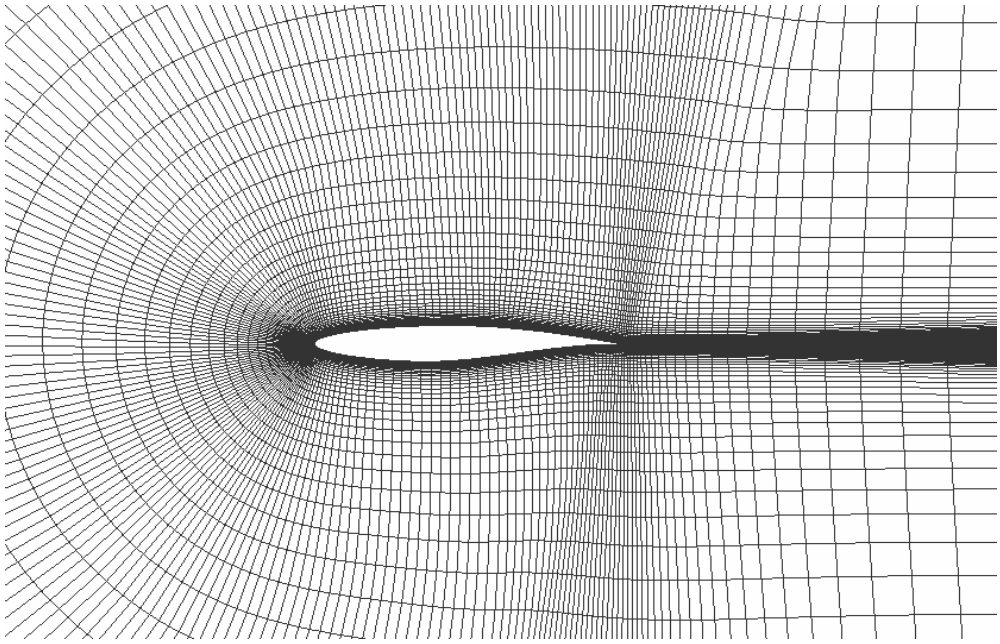

b) Near blade grid

Figure 4.1 (cont.): RAE2822 airfoil (257x97x5) C-grid.

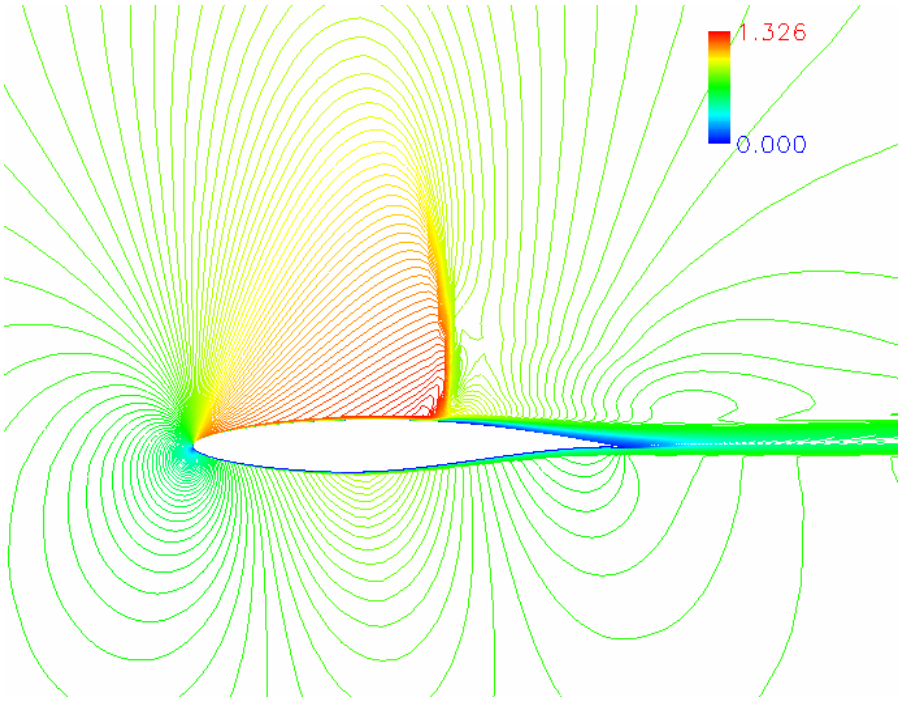

a) k-ω-SST

Figure 4.2: Mach number contours for RAE2822 airfoil.

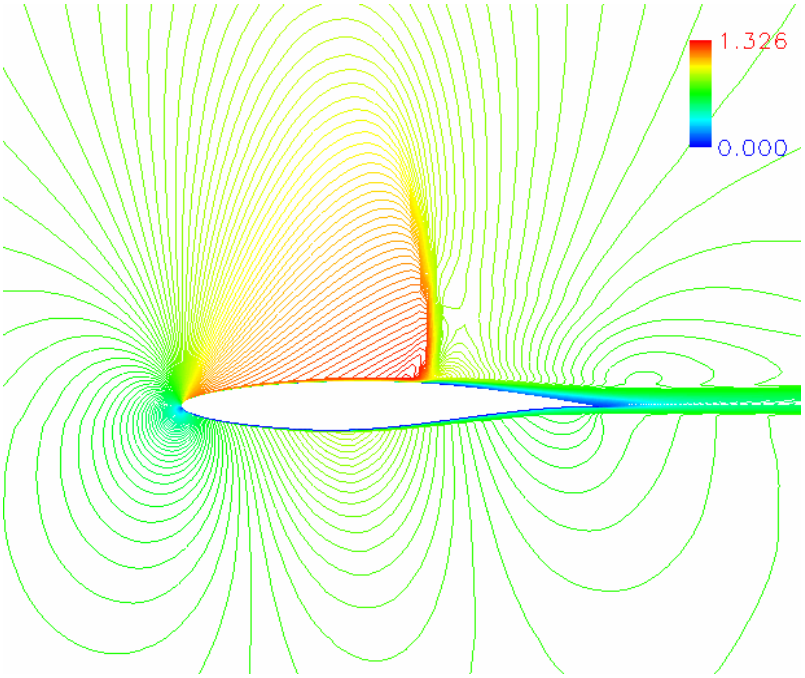

b) HRKES1

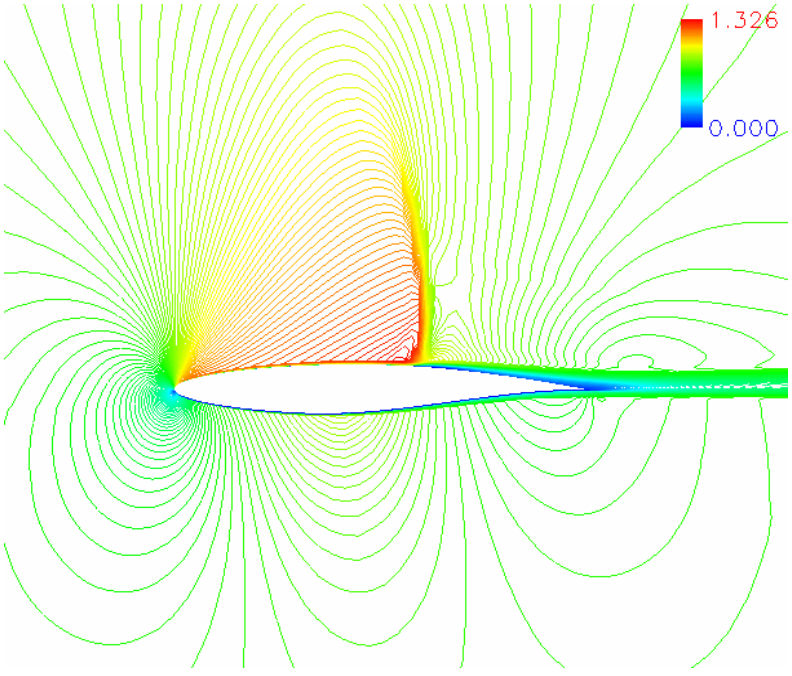

c) HRKES2

Figure 4.2 (cont.): Mach number contours for RAE2822 airfoil.

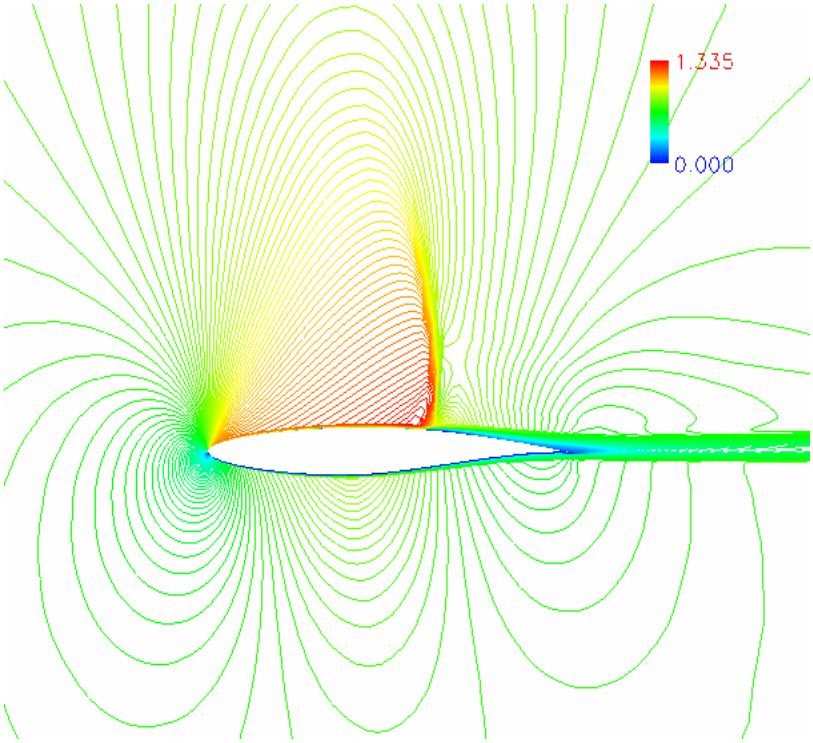

d) HRKES3

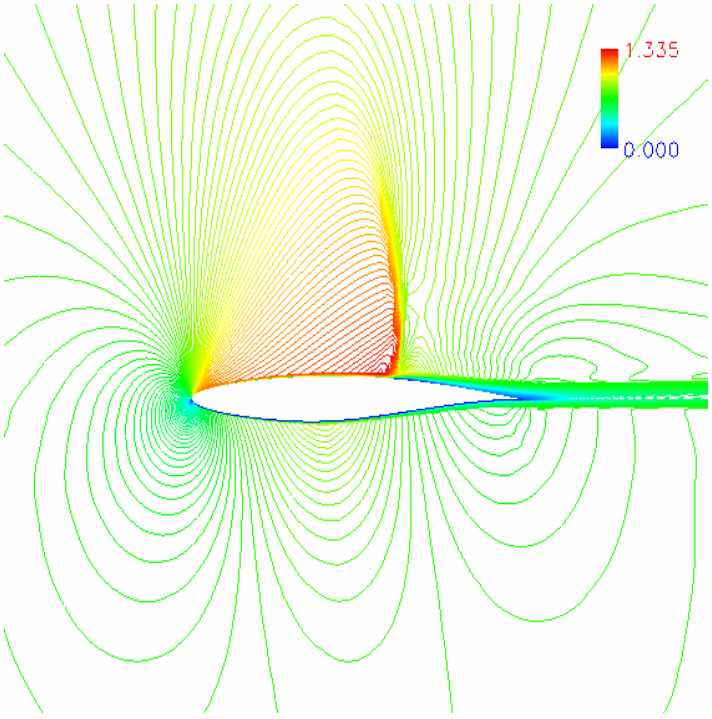

e) HRKES4

Figure 4.2 (cont.): Mach number contours for RAE2822 airfoil.

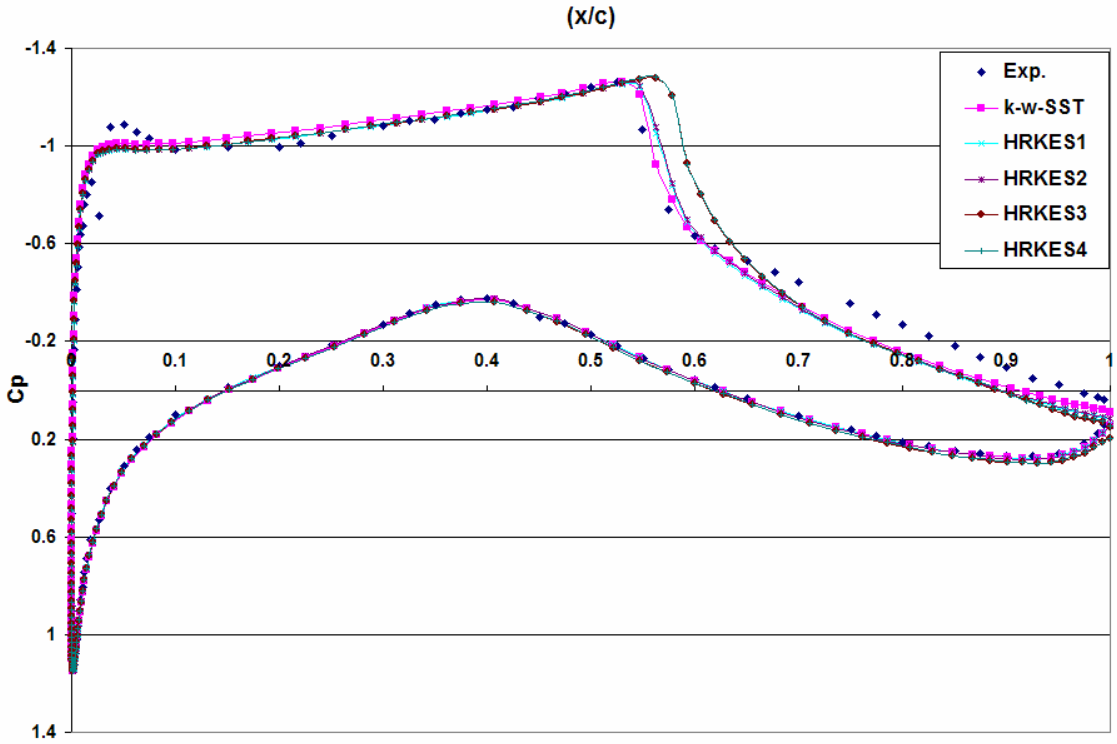

Figure 4.3: Pressure coefficient distribution over RAE2822 airfoil.

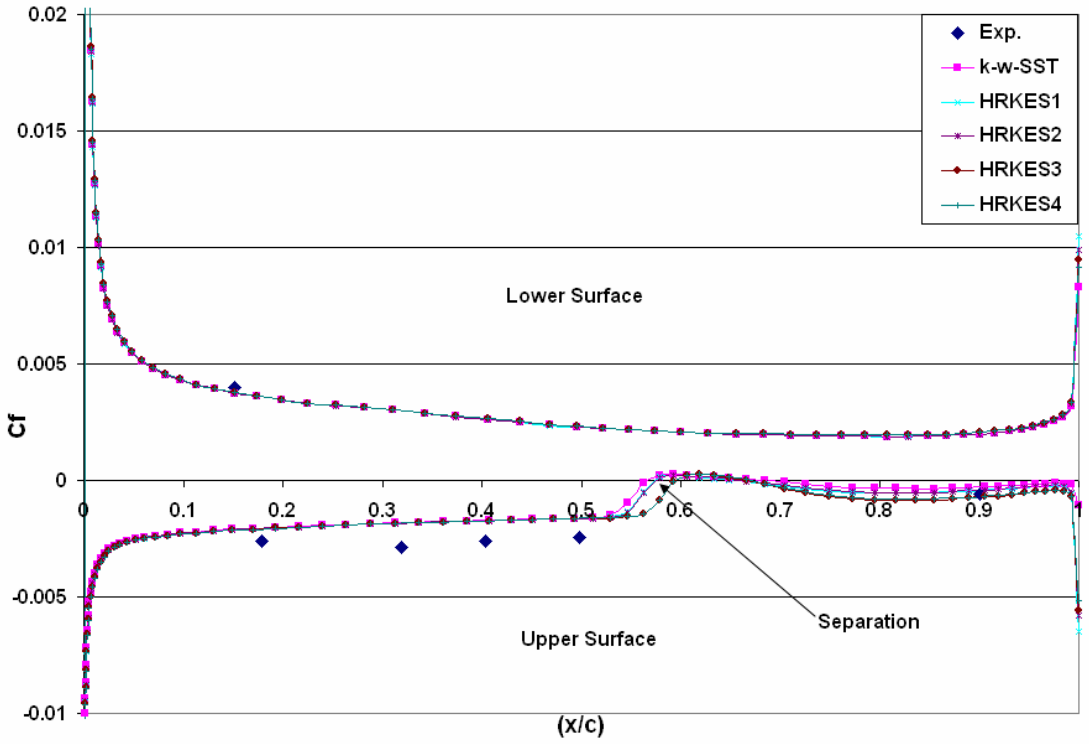

Figure 4.4: Skin friction coefficient distribution over RAE2822 airfoil.

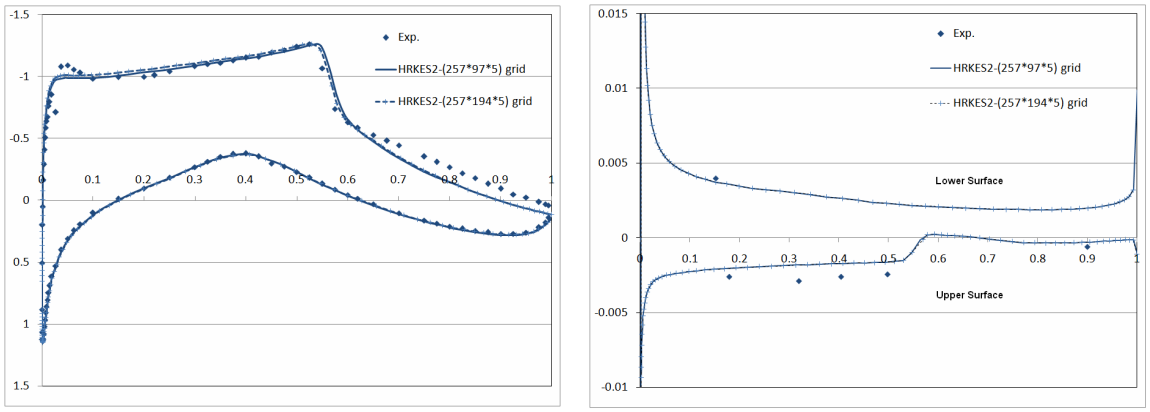

a) pressure coefficient b) skin friction coefficient

Figure 4.5: Grid effect on the pressure and skin friction coefficients distribution over RAE2822 airfoil.

4.2 NACA 0015 Airfoil

To further explore the differences between the HRKES and the k-ω-SST turbulence models, the flow field over a NACA 0015 airfoil is studied at different high angles of attack. This test case corresponds to the test case by Piziali.[78] The flow conditions are as follows: Mach number of 0.289, Reynolds number of 1.94 millions. This case is simulated using GT-TURBO3D with periodic boundary conditions in the span-wise direction. The C-grid used in the present computations consists of 257 cells in the direction wrapping the airfoil, 129 cells in the normal direction, and 5 cells in the span direction as shown in Figure 4.6.

The lift coefficient values for this airfoil at different angles of attack using all four options of the HRKES model and the k-ω-SST model are compared to the experimental data[78] in Figure 4.7. The experimental data has more points than the computational data at high angles of attack; this is because the experimental measurements are obtained

while the airfoil is slowly pitched up and down, while the computational data is obtained by fixing the airfoil at different angles of attack. The computational results agree well with the experimental results for all the turbulence models studied except near the stall vicinity. It is found that the HRKES1 and HRKES2 predict the lift coefficient values better than the baseline k-ω-SST model at higher angles of attack. Also, HRKES1 and HRKES2 predict the stall onset at an angle of attack around 14^{o} while the k-ω-SST model predicts it to be around 16^{o}. It is also found that HRKES3 and HRKES4 predicts higher lift coefficient values than k-ω-SST, HRKES1, and HRKES2 models at higher angles of attack. This shows that the fidelity of the HRLES turbulence models depend on the underlying blending functions used. Furthermore, the solutions with or without using the KES model realizability constraints are similar which indicates that the realizability constraints have a minor role in the current HRKES model. Figure 4.8 shows the drag and moment coefficients for this airfoil at different angles of attack using the HRKES2 model and the k-ω-SST model compared to the experimental data.[78] The HRKES2 model predicts more drag and less moment than the baseline k-ω-SST model at high angles of attack.

Next, the flow field around the airfoil at high angles of attack is examined through a study of the Mach number contours. The computed Mach number contours for both the k-ω-SST and HRKES2 turbulence models are shown in Figure 4.9, Figure 4.11, and Figure 4.13 for 14^{o}, 15^{o}, and 16^{o} angles of attack, respectively. The smooth Mach number contours indicate that the blending in the HRKES model does not introduce any unphysical fluctuations to the flow field in the buffer zone for large separated flow fields.

The Mach number contours also show that the k-ω-SST model predicts a smaller separation bubble than the HRKES2 model, which leads to the over prediction of the k-ω-SST model in the lift coefficient values compared to that of the HRKES2 model.

The flow field viscosity contours (as a multiplication of the laminar viscosity) around the airfoil at high angles of attack are shown in Figure 4.10, Figure 4.12, and Figure 4.14 for 14^o, 15^o, and 16^o angles of attack, respectively. Those figures show that the k-ω-SST model predicts higher and denser viscosity levels than the HRKES2 model, which leads the k-ω-SST model to predict smaller separation bubble than the HRKES2 model.

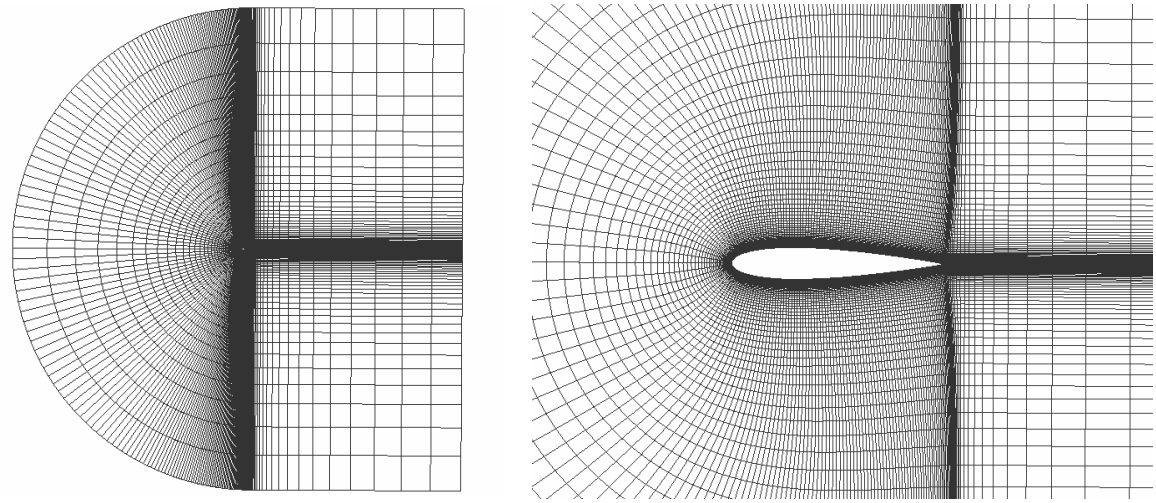

a) Far-field grid.

b) Near blade grid.

Figure 4.6: NACA 0015 airfoil (257x129x5) C-grid.

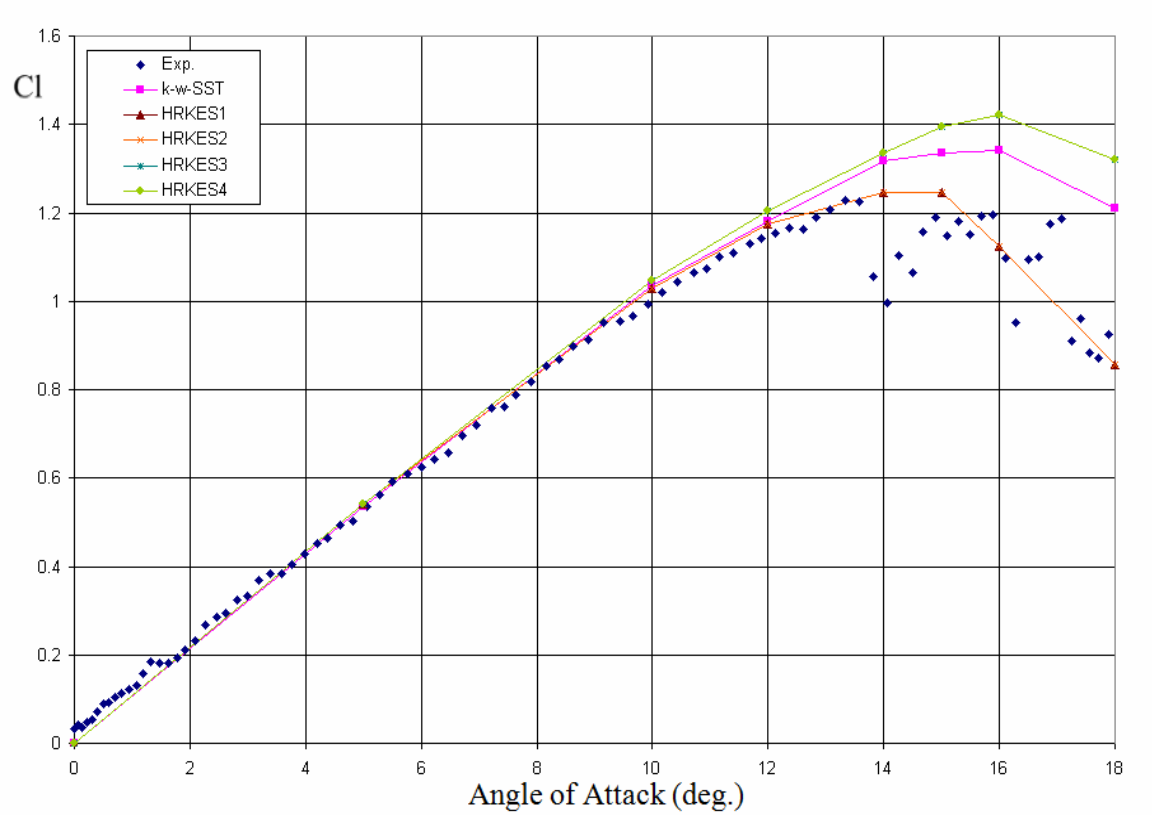

Figure 4.7: Lift coefficient vs. angle of attack for NACA0015 airfoil.

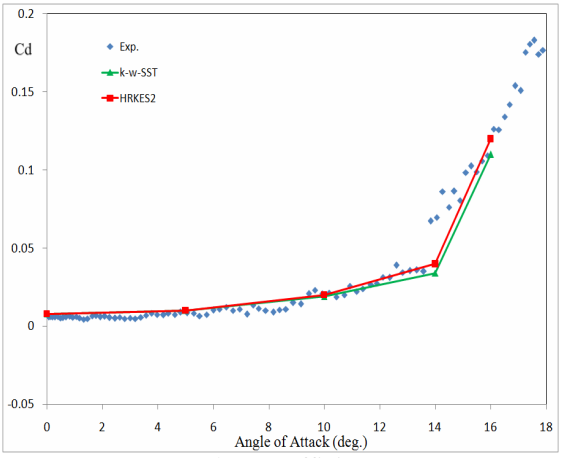

a) drag coefficient

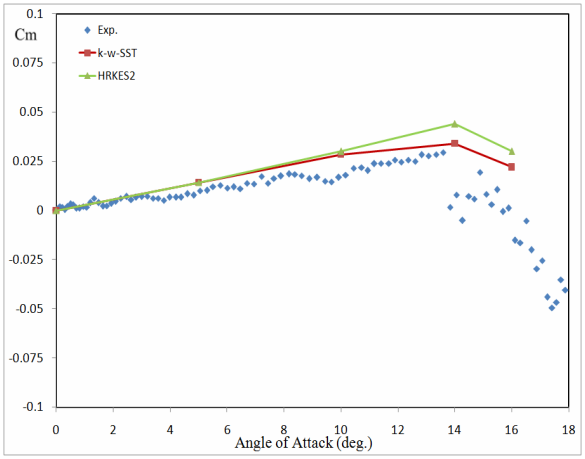

b) moment coefficient

Figure 4.8: Drag and moment coefficients vs. angle of attack for NACA0015 airfoil.

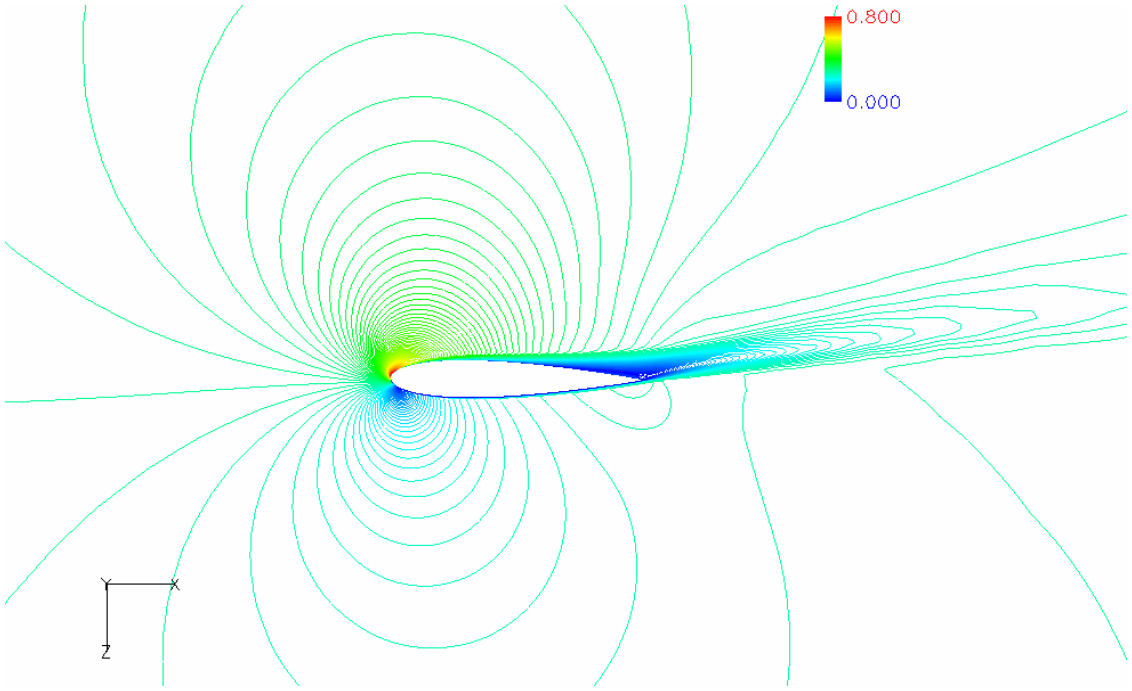

a) k-ω-SST

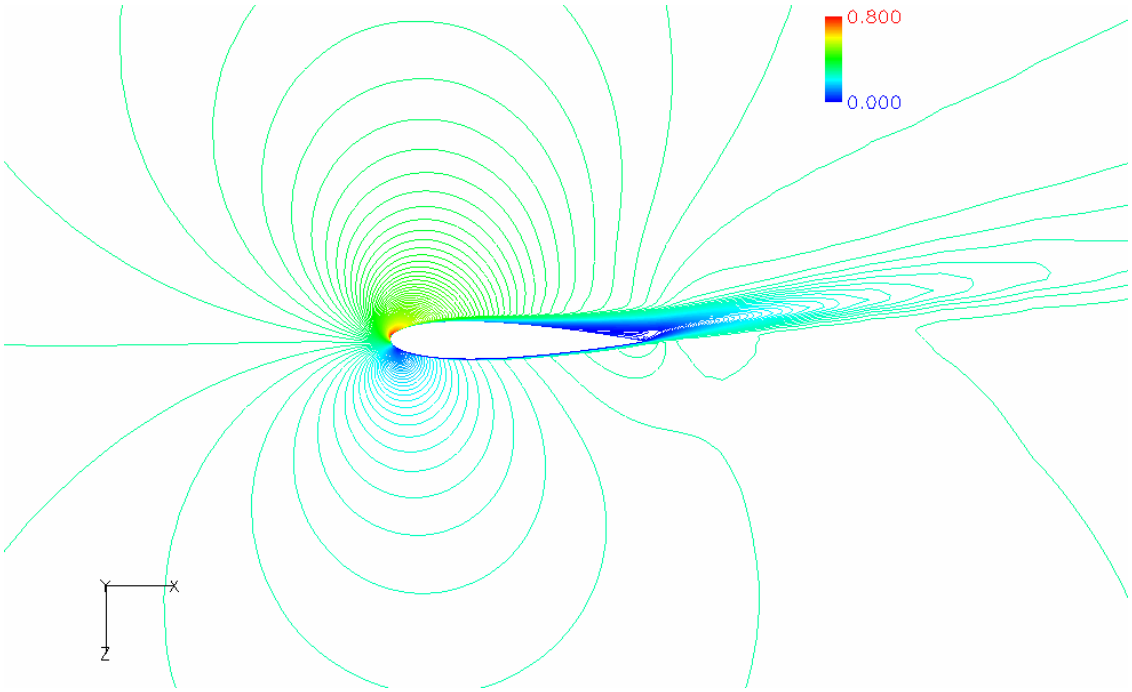

b) HRKES2

Figure 4.9: Mach no. contours for NACA0015 at 14^{o} angle of attack.

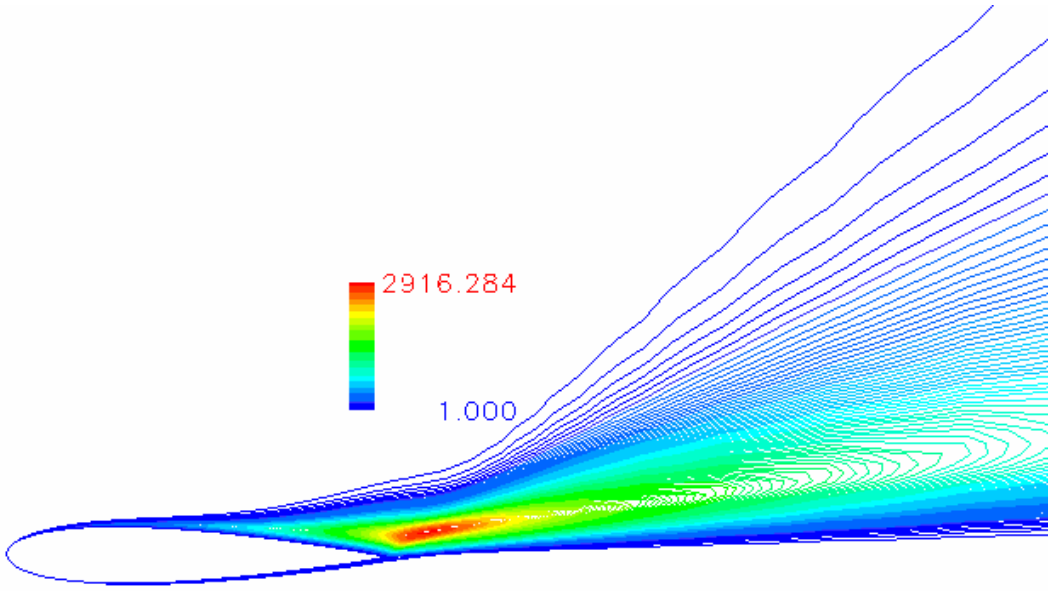

a) k-ω-SST

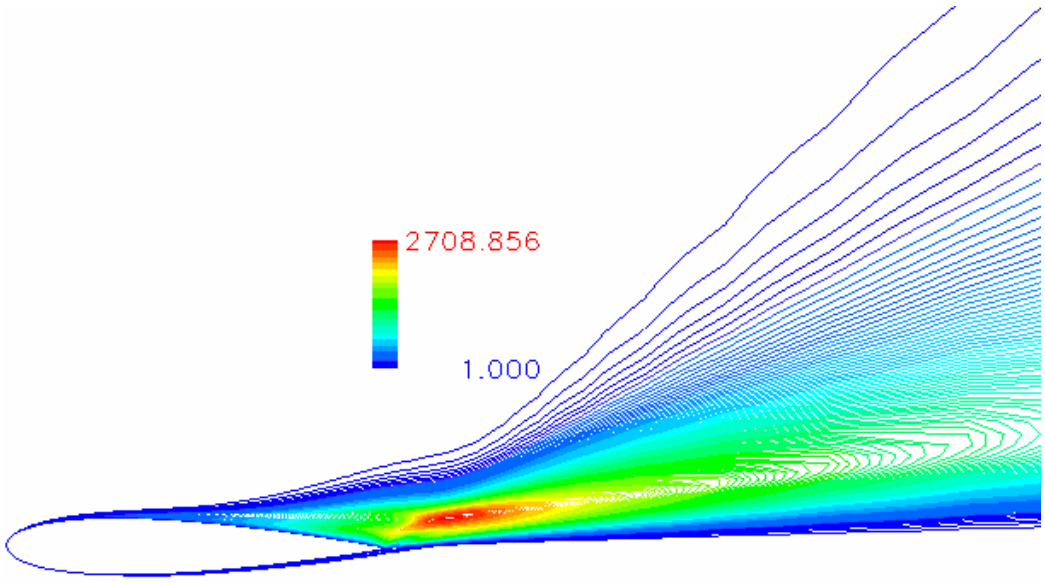

b) HRKES2

Figure 4.10: Viscosity contours for NACA0015 at 14^{o} angle of attack.

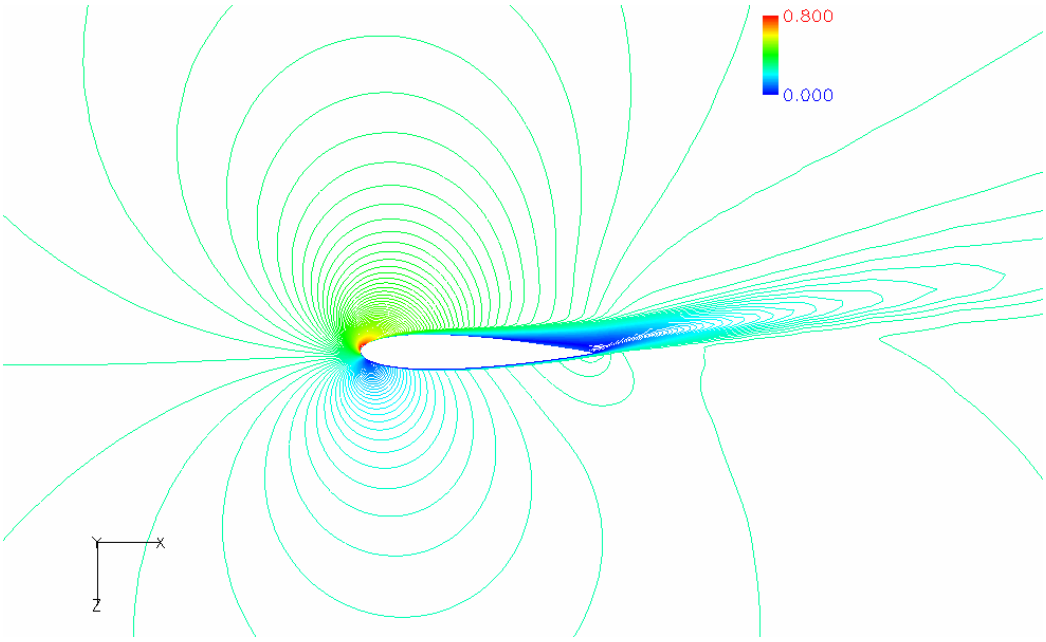

a) k-ω-SST

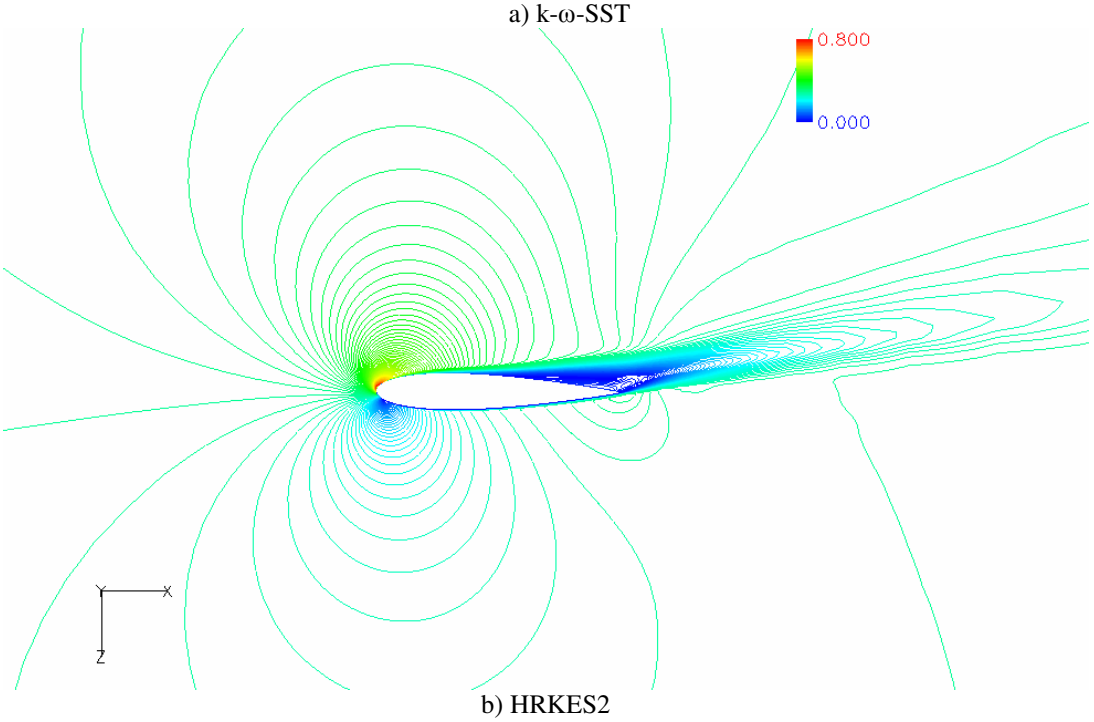

b) HRKES2

Figure 4.11: Mach no. contours for NACA0015 at 15^{o} angle of attack.

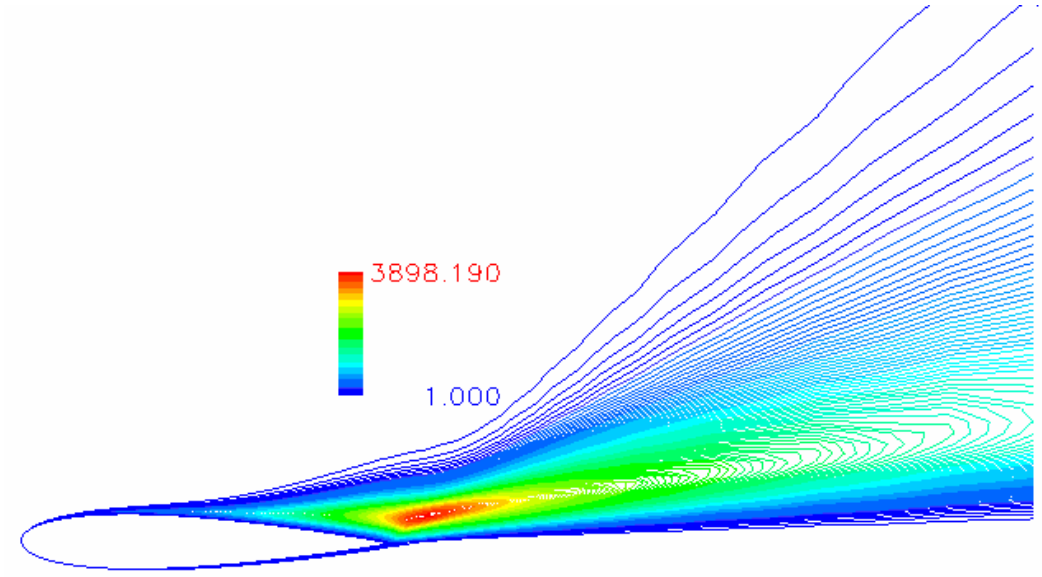

a) k-ω-SST

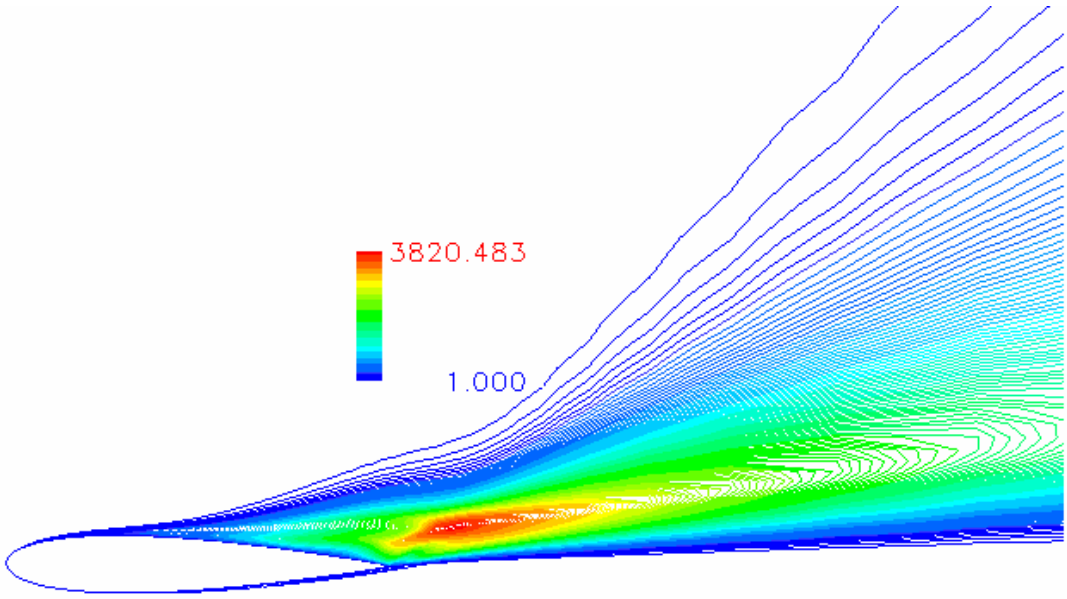

b) HRKES2

Figure 4.12: Viscosity contours for NACA0015 at 15^{o} angle of attack.

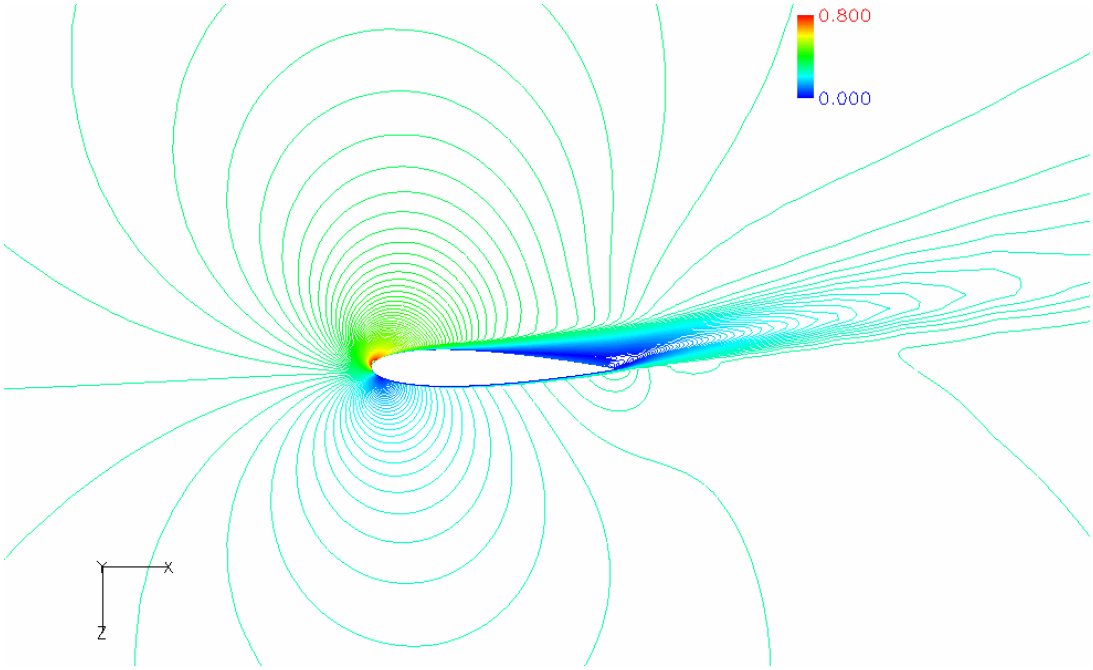

a) k-ω-SST

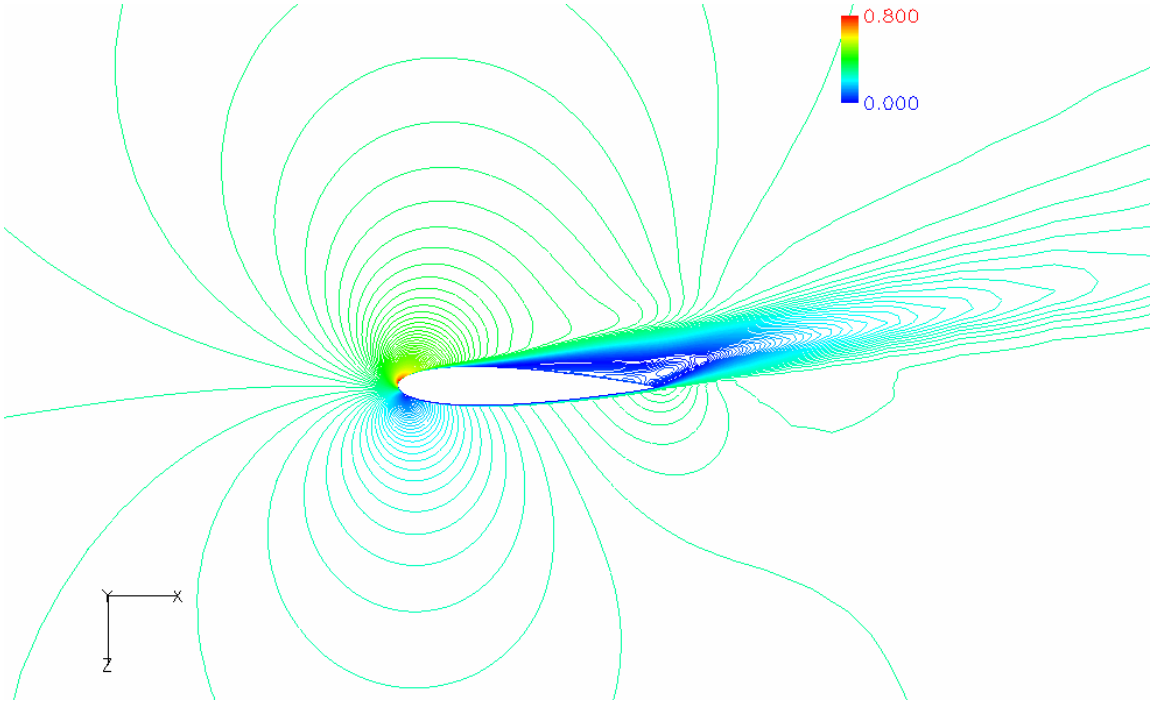

b) HRKES2

Figure 4.13: Mach no. contours for NACA0015 at 16^{o} angle of attack.

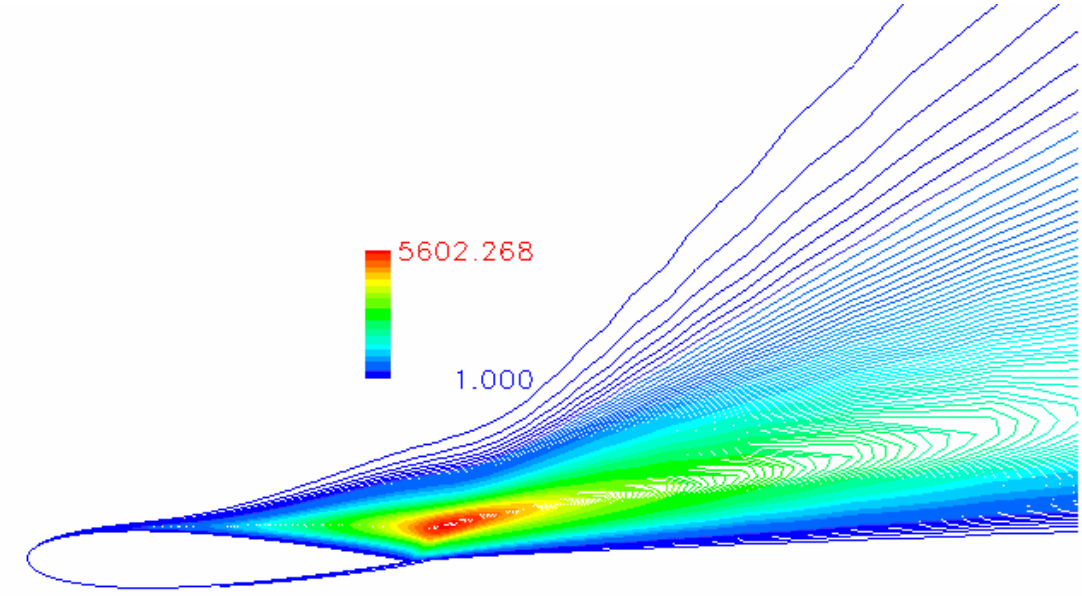

a) k-ω-SST

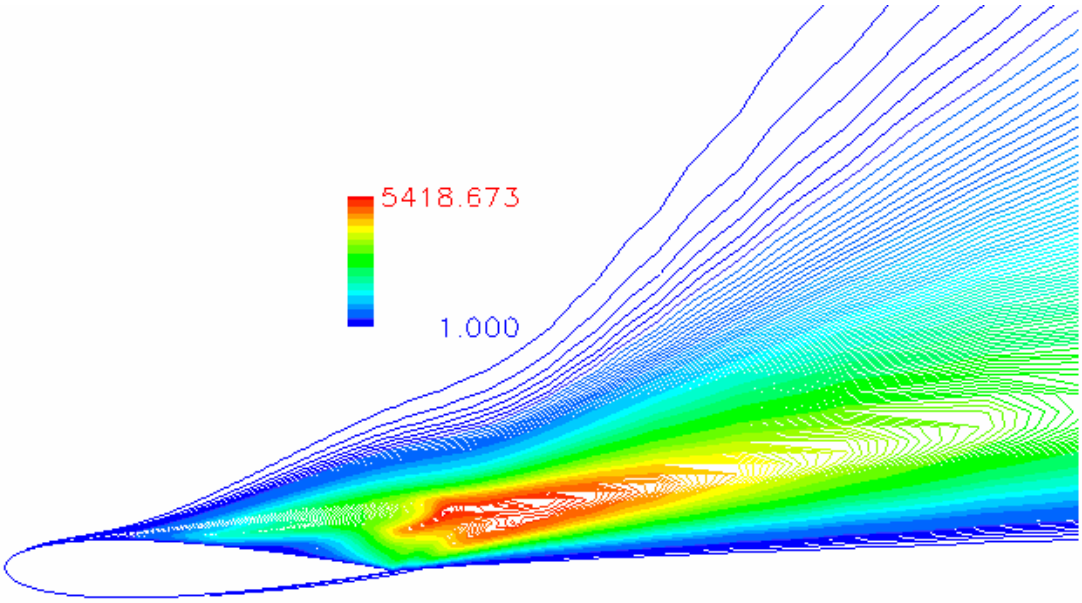

b) HRKES2

Figure 4.14: Viscosity contours for NACA0015 at 16^{o} angle of attack.

4.3 Single Bladed Turbine Configuration

As a further validation of this analysis, this solver is first evaluated for axial turbine configurations. The present methodology is applied to an annular turbine stator that was developed and tested at NASA Glenn Research Center by Goldman et al.[79] This stator has 36 vanes. The vanes have an axial chord length of 0.03823 m, a span (between the hub and the tip) of 0.0381 m, a 0.508 m tip diameter, and a hub-to-tip radius ratio of 0.85. The inlet Mach number is 0.211. This stage has a design pressure ratio of 0.6705, an exit Mach number of 0.665 and a Reynolds number based on the axial chord of 173,000. A C-grid with 137 cells in the direction wrapping the blade, 63 cells in the radial direction, and 32 cells in the blade-to-blade direction is used in this study as shown in Figure 4.15a. This grid is generated using the grid generator (TCGRID) developed by Chima.[80]

The global convergence characteristic of the different turbulence models studied here is first examined to investigate how robust is the proposed HRKES model compared to the classical k-ω-SST model for 3-D flows. Figure 4.16 shows the convergence history of the normalized mass flow rate for all of the studied turbulence models; all of the HRKES four options (listed in Table 3.1) have good convergence characteristics, similar to the baseline k-ω-SST model, and they all converge after approximately 20,000 iterations to the designed mass flow rate. This indicates that the HRKES model is as robust as the k-ω-SST model for 3-D flows.

Next, the flow field inside the stator passage is examined through a study of the Mach number contours and comparison with the published computational results.[81] The Mach number contours at 50% span from hub are shown in Figure 4.17; the computed

results show a good agreement with the published computational results.[81] The smooth Mach number contours indicate that the transition between the near-wall k-ω-SST model and the outer region KES model is smooth and does not introduce any noise or fluctuations to the flow field in the buffer zone for 3-D flow fields. It is found that all the studied turbulence models predict almost identical Mach number contours indicating that for completely attached flows, the proposed HRKES model behaves like the baseline k-ω-SST model.

Next, the details of the flow over the blades are examined through a comparison of pressure distributions over the stator blade surface with experimental[79] data. The normalized surface pressure distributions at 50% span from hub are shown in Figure 4.18a. The computed solution agrees very well with the experimental[79] data over most of the blade surface except for slight discrepancies over the upper blade surface aft of 75% of the chord.

To assess the grid independency of the turbulence models studied, a limited grid independency study is done for this configuration. A coarse C-grid with 97 cells in the direction wrapping the blade, 33 cells in the radial direction, and 32 cells in the blade-to-blade direction is also used in this study (Figure 4.15b). This grid is also generated using (TCGRID[80]). The normalized surface pressure distributions at 50% span from hub are shown in Figure 4.18b. The computed solution agrees very well with the experimental[79] data over most of the blade surface. It can be seen that the computed pressure distributions are virtually identical for the coarse and fine grids with all the turbulence

models. The convergence behavior and the Mach number contours are also similar and are not shown here for brevity.

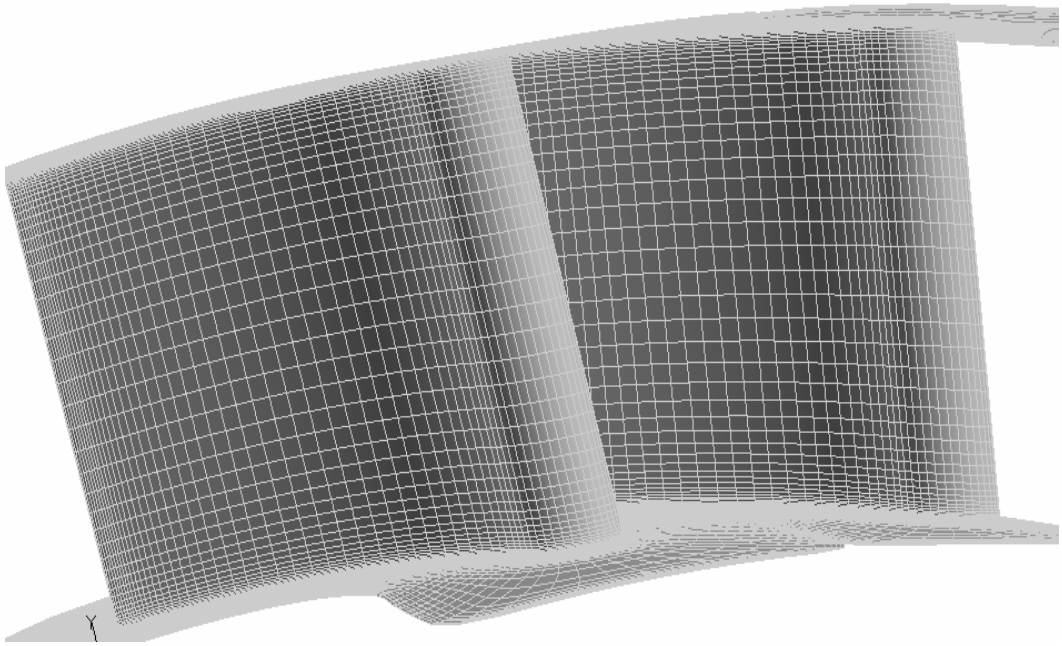

a) 137x63x32 grid

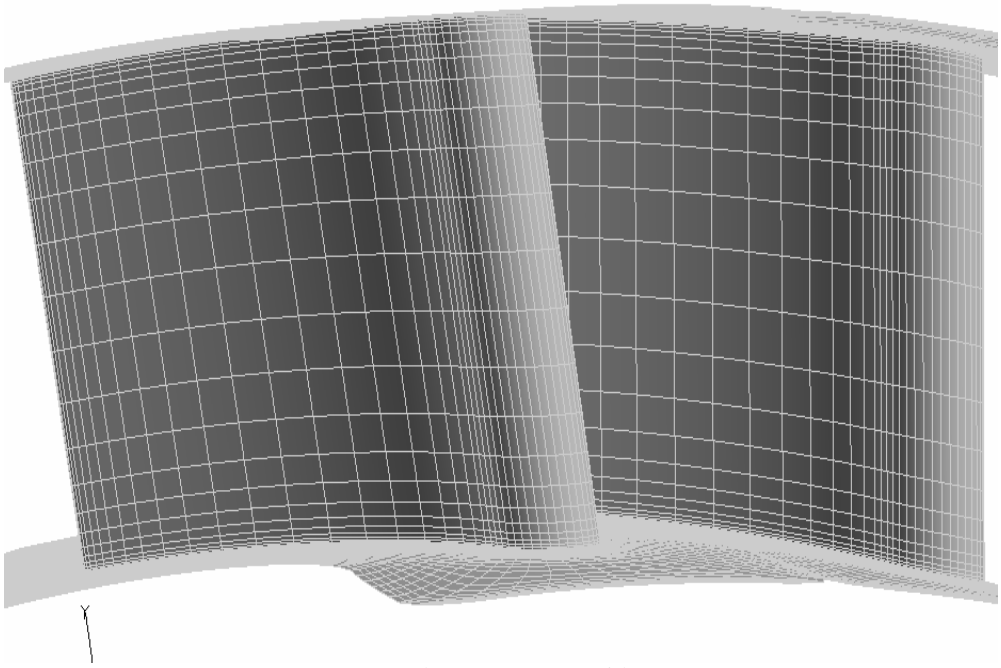

b) 97x33x32 grid

Figure 4.15: Goldman turbine vane grids.

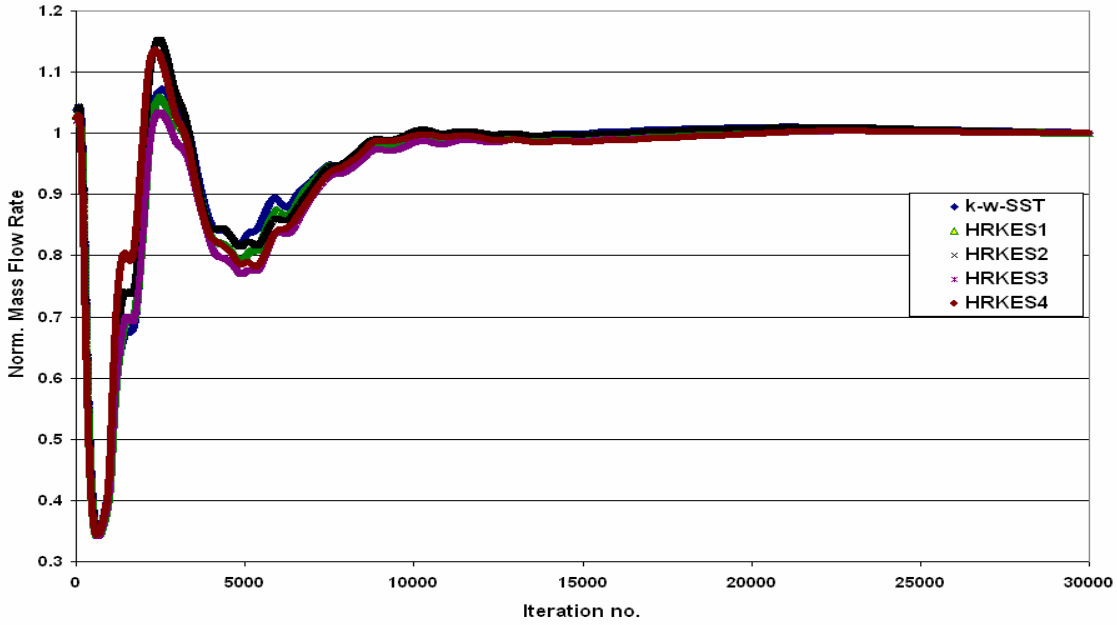

Figure 4.16: Non-dimensional mass flow rate convergence history for Goldman turbine vane.

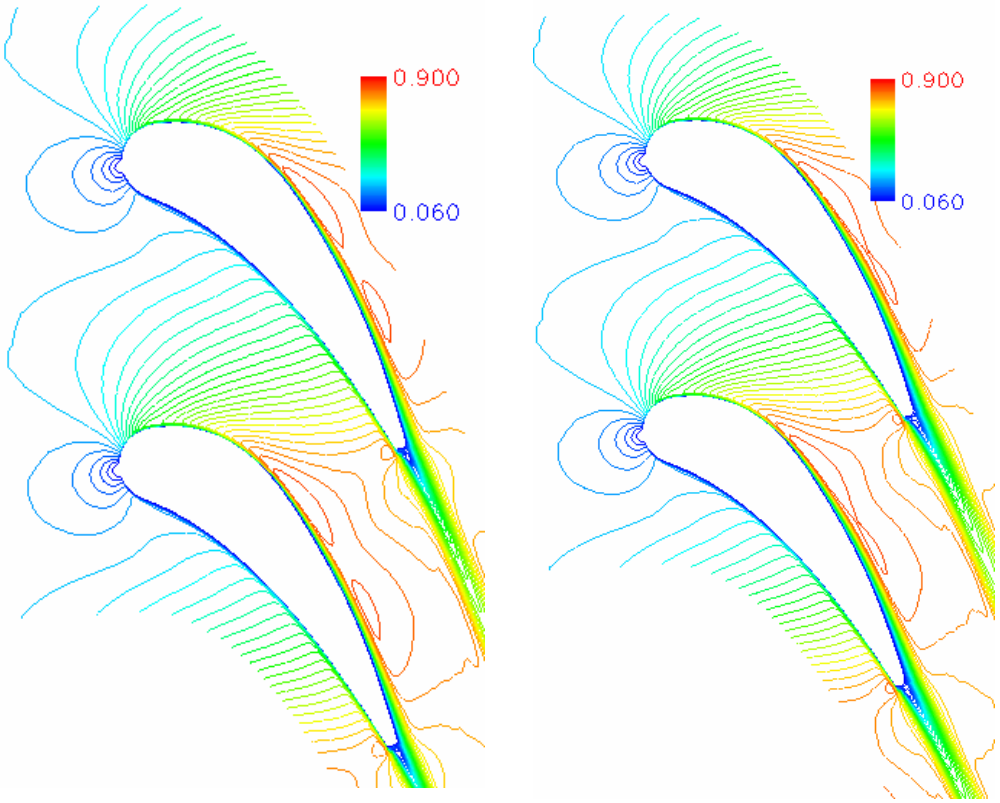

a) k-ω-SST

b) HRKES1

Figure 4.17: Mach number contours at mid span for Goldman turbine vane.

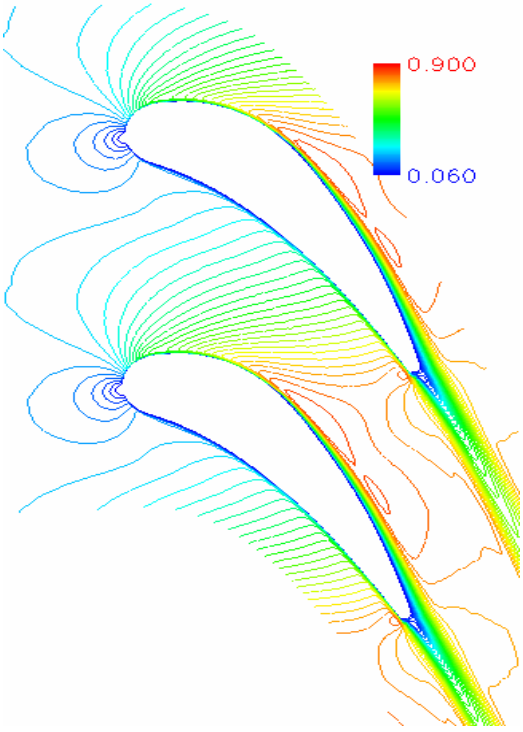

c) HRKES2

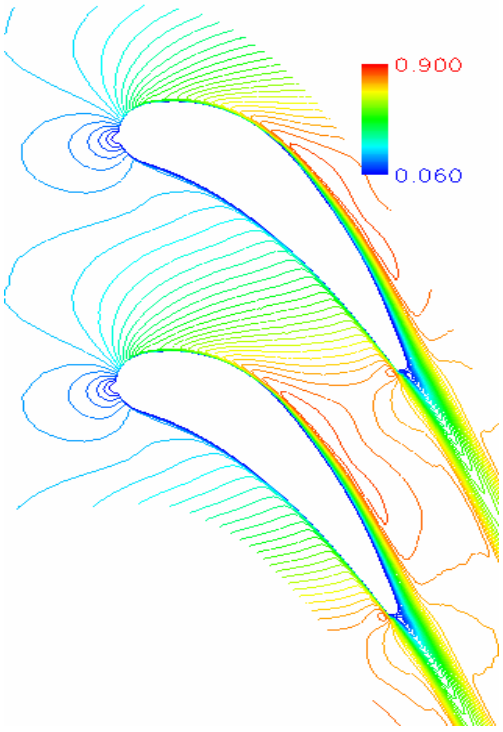

d) HRKES3

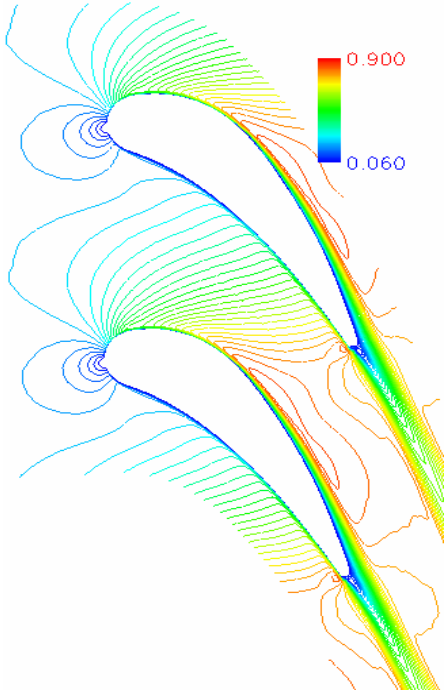

e) HRKES4

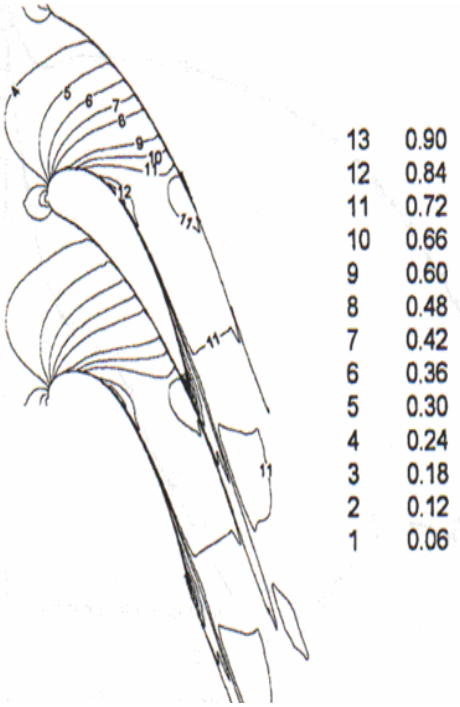

f) Yeuan,J.J. et al.[81]

Figure 4.17 (cont.): Mach number contours at mid span for Goldman turbine vane.

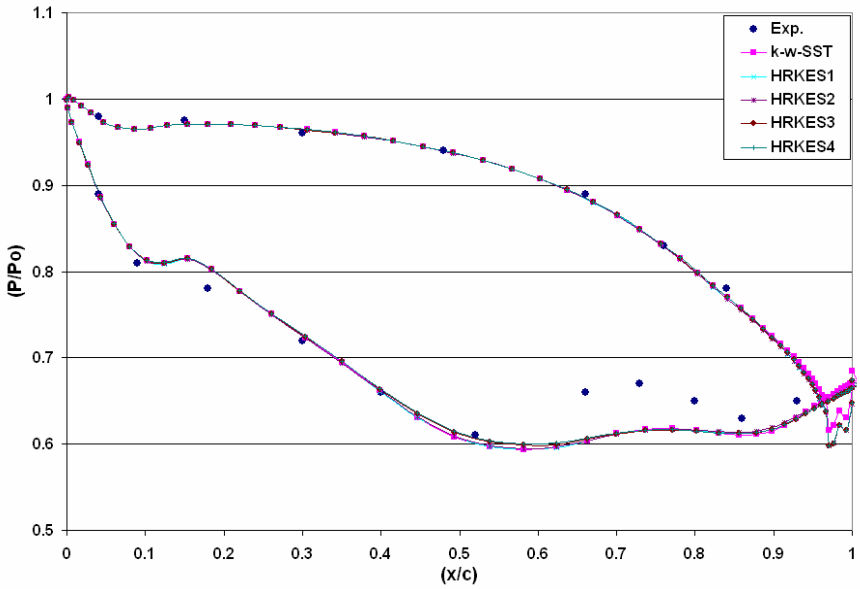

a) 137*63*32 grid

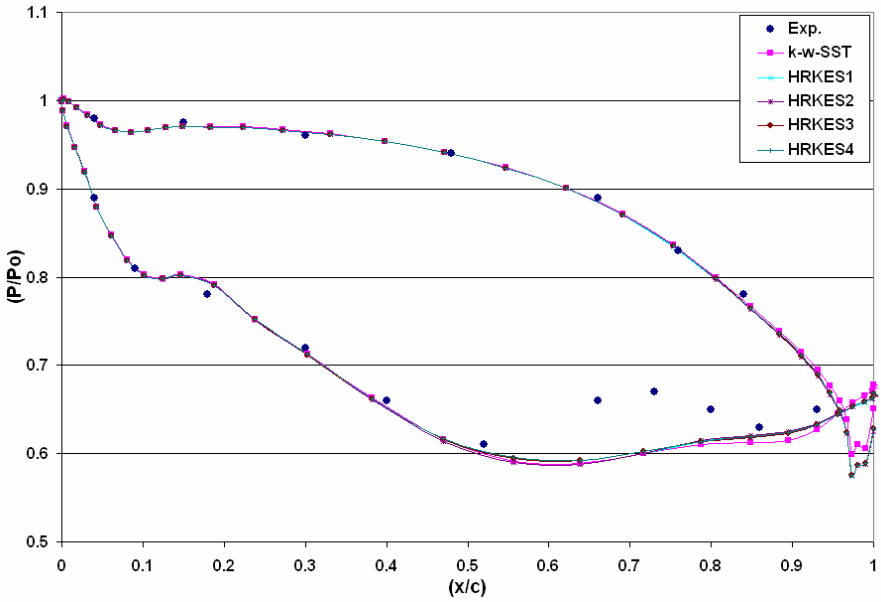

b) 97*33*32 grid

Figure 4.18: Surface pressure distributions at mid span for Goldman turbine vane.

4.4 NASA Rotor 67 Compressor Configuration

Next, the present methodology is applied to the first stage rotor (NASA Rotor 67) of a two stage transonic fan designed and tested with laser anemometer measurements[82] at the NASA Glenn center. Its design pressure ratio is 1.63, at a mass flow rate of 33.25 kg/sec. The rotor has 22 blades with tip radii of 25.7 cm and 24.25 cm at the leading and trailing edge, respectively. The hub/tip radius ratio is 0.375 at the leading edge and 0.478 at the trailing edge. The design rotational speed is 16043 RPM, and the tip leading edge speed is 429 m/sec with a tip relative Mach number of 1.38. An H-grid with 125 cells in the axial direction, 63 cells in the blade-to-blade direction, and 41 cells in the radial direction used in the current study is shown in Figure 4.19. Simulations are done at the design point conditions and by using a global time step.

The convergence characteristic for all the turbulence models studied is first examined. Figure 4.20 shows the convergence history of the normalized mass flow rate ($\dot{m}/\dot{m}_{design}$) through the rotor; all the approaches have good convergence characteristics and they all asymptotically converge after approximately 52,000 iterations to the same mass flow rate to within 1% of each other. The discrepancy between the computed and the measured mass flow rate is within 2%. The computed pressure ratio across the rotor is approximately 1.59 for all the turbulence models studied compared to the measured value of 1.63. Figure 4.21 shows the density contours at 50% span from the hub for all the turbulence models studied. The HRKES model results agree well with the baseline k-ω-SST model results.

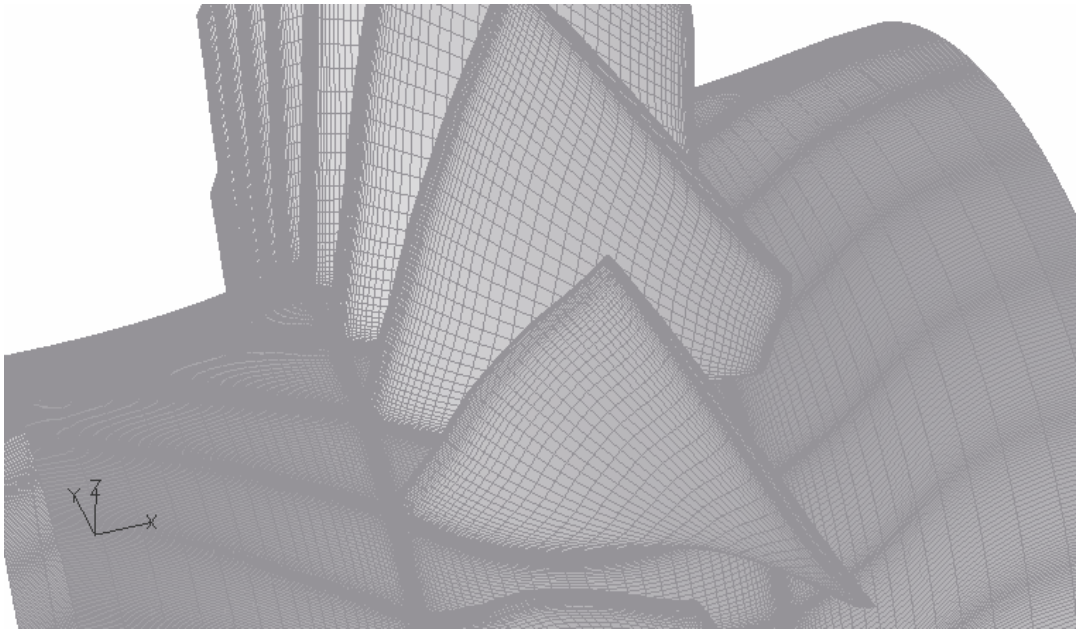

Figure 4.19: 125x63x41 H-Grid used for NASA Rotor 67.

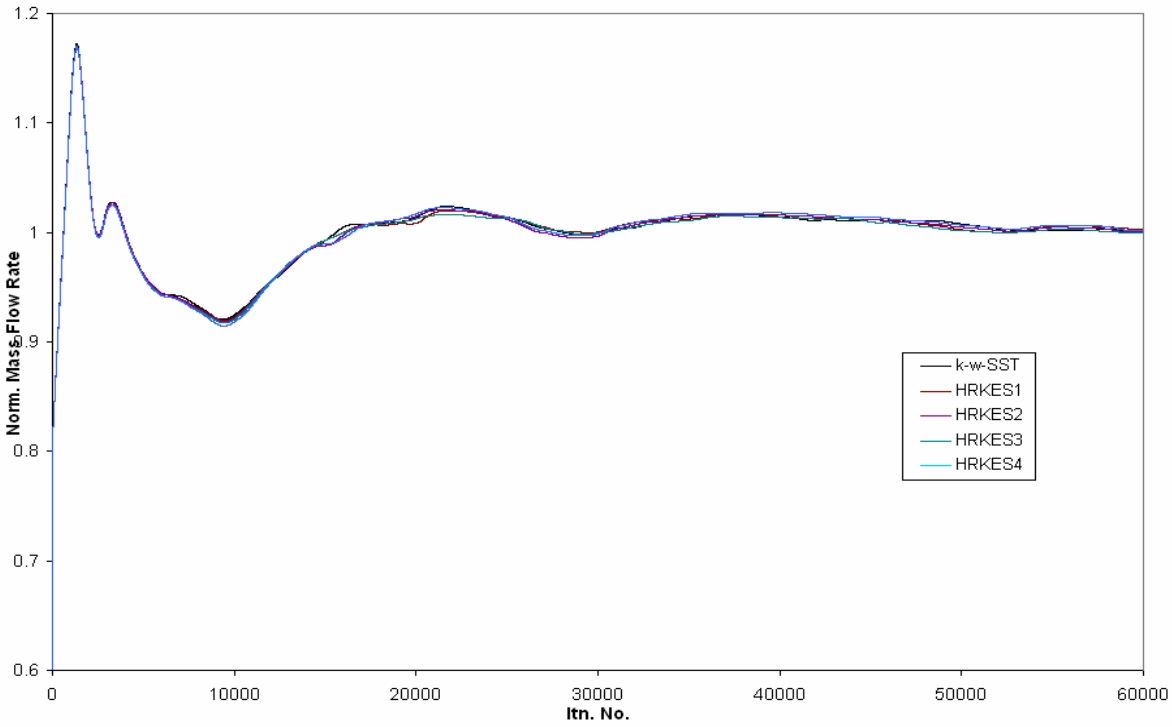

Figure 4.20: Non-dimensional mass flow rate convergence history for NASA Rotor 67.

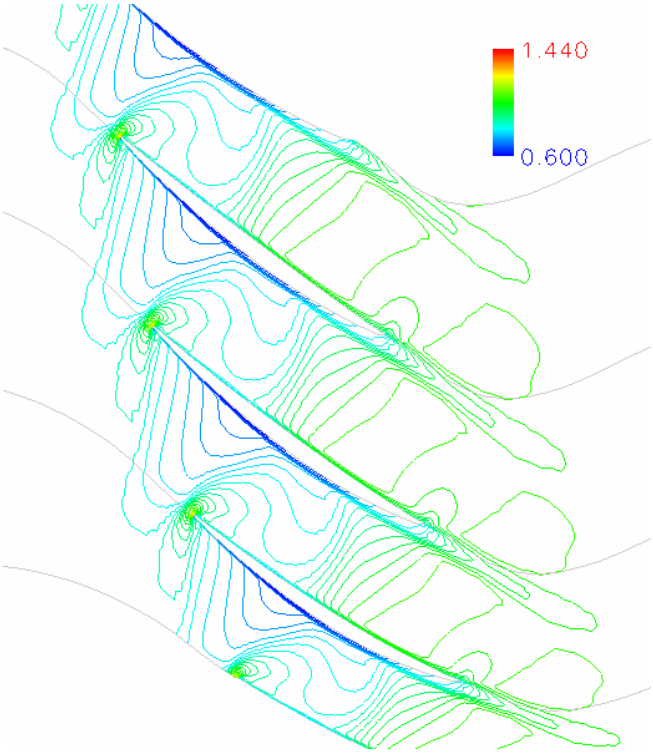

a) k-ω-SST

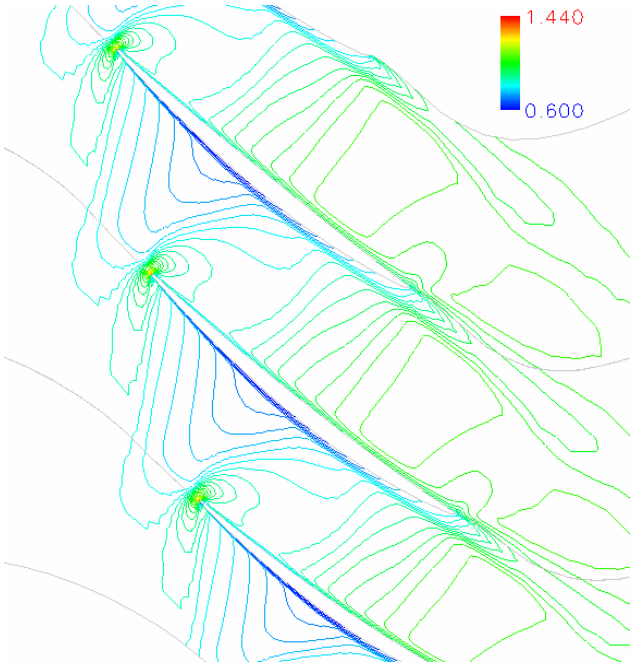

b) HRKES1

Figure 4.21: Density contours at mid-span for NASA Rotor 67.

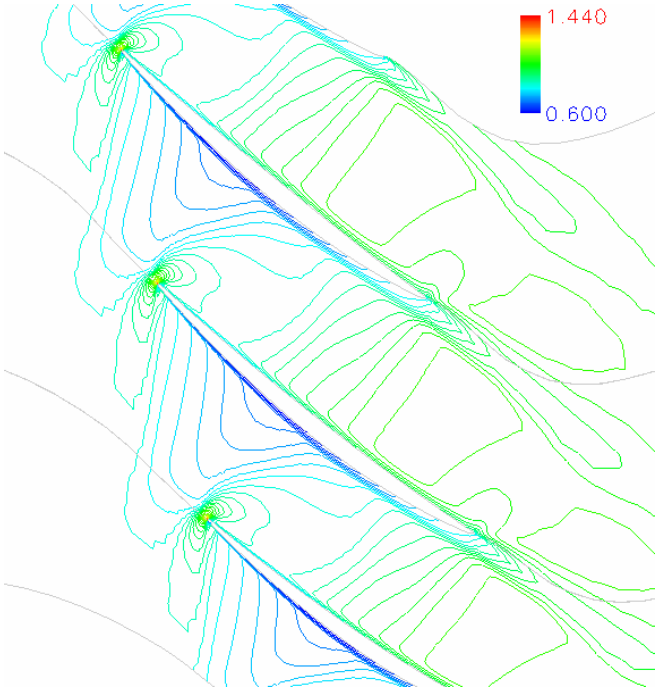

c) HRKES2

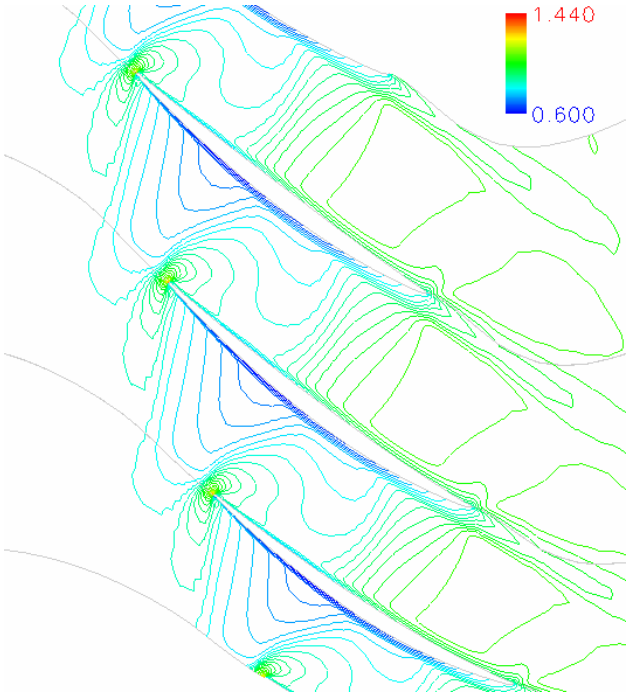

d) HRKES3

Figure 4.21 (cont.): Density contours at mid-span for NASA Rotor 67.

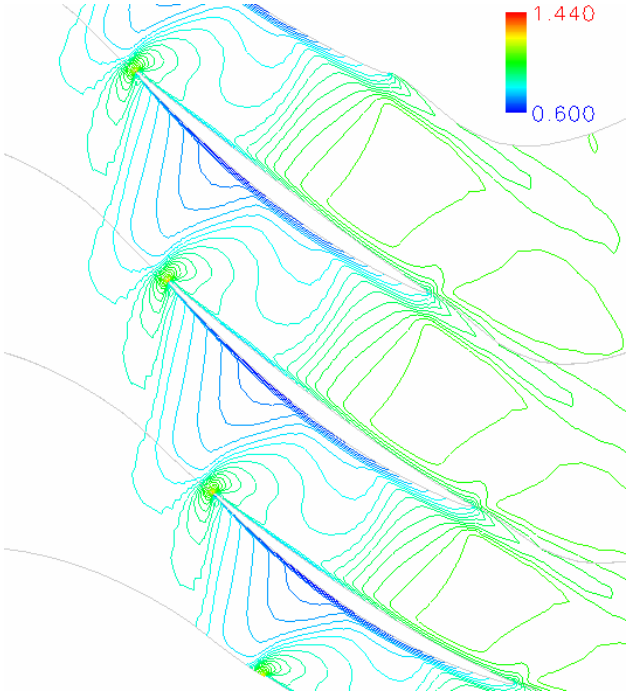

e) HRKES4

Figure 4.21 (cont.): Density contours at mid-span for NASA Rotor 67.

4.5 SSME Turbine Stage

The first stage (a stator and a rotor) of the two-stage fuel turbine on the space shuttle main engine (SSME)[83] is used to systematically assess the five average plane interface boundary conditions (IBC1 to IBC5, mentioned in the previous chapter and summarized in Table 4.1 below) and the unsteady sliding mesh (USM) interface boundary condition. The SSME[83] configuration has 41 stator vanes and 63 rotor blades. The grid used is shown in Figure 4.22. It is a two block H-grid with 127 cells in the axial direction, 45 in the radial direction, and 45 cells in the azimuthal direction. This grid is generated using TCGRID.[80] This stage operates at an inlet Mach number of 0.132 with a

design pressure ratio of 0.65, and a wall to total temperature ratio of 0.7. Details of the simulations carried out and the results are found in the following sections.

4.5.1 Averaging Plane Interface Boundary Condition:

All five averaging plane interface boundary conditions described in the previous chapter and summarized in Table 4.1 are coded and tested. The first four (IBC1 through IBC4) require comparable CPU time, while IBC5 scheme requires 1% to 2% of extra CPU time because it involves more operations. Thus the computational penalty is negligible with the IBC5 scheme. The global convergence characteristic of the five interface boundary condition approaches (IBC1 to IBC5) is first examined. The convergence history of the normalized mass flow rate ($\dot{m}/\dot{m}_{design}$) for the stator block and the rotor block for all the five interface boundary conditions are shown in Figure 4.23. These simulations are done using a global time step to monitor any unsteady flow events of interest. Figure 4.23 shows that all the approaches have a good convergence characteristic and that they all asymptotically converge to the same mass flow rate to within 1% of each other. The discrepancy between the computed and the measured mass flow rate is also within 1%.

Next, the flow behavior at the rotor-stator interface is examined. One way of doing this is to look at the difference between the mass flow rate leaving the upstream block and entering the downstream block as shown in Figure 4.24. The transient in the solution prior to the establishment of nominal steady state (before 15,000 iterations) is not shown. This quantity is a measure of the error in conserving mass at the interface. It can be seen that that IBC1, IBC4 and IBC5 conserve the mass flow rate across the interface better

than IBC2 and IBC3. All of the methods, with the exception of IBC2, give less than 0.1/% error in the mass flow rate at the interface. This is comparable to the errors reported by Chima[71] for the same configuration on a comparable grid. It can be concluded that IBC2, based on these results, is not an acceptable approach.

Next, the flow field inside the rotor-stator passages is examined through a study of the Mach number contours and comparison with the published[71] data. The Mach number contours at 50% span from the hub are shown in Figure 4.25. The results for IBC1, IBC3, and IBC4 are shown in Figure 4.25a-c, respectively. Those figures show that the Mach number contours at the stator exit become uniform, as a consequence of the averaging used in IBC1, IBC3, and IBC4. This is an unphysical behavior and when it is used to get an upstream boundary condition for the rotor row, it will create incorrect uniform inflow information which will contaminate the flow predictions over the rotor. The IBC5 approach on the other hand produces a non-uniform Mach number distribution at the stator exit as shown in Figure 4.25d. These contours are similar in shape to those computed by Chima[71] using a similar characteristic boundary condition approach for the same configuration (Figure 4.25e). Thus, it can be concluded that only the IBC5 approach retains some of the flow non-uniformity at the rotor-stator interface.

This also can be seen by plotting the Mach number contours at the exit of the stator row block for IBC1, IBC3, IBC4, and IBC5 as shown in Figure 4.26a-d, respectively. Those Mach number contours are for two adjacent stator blade passages. It is expected that the Mach number contours will show the azimuthal variations such as the deficit in velocity due to the stator wake at the interface in a physically consistent boundary

condition implementation. Only the IBC5 approach captures and retains the azimuthal details such as those of the Mach number deficit associated with the wake from the stator blades as shown in Figure 4.26d. This deficit is totally smeared out in IBC1, IBC3, and IBC4 as shown in Figure 4.26a-c.

Next, the details of the flow over the blades are examined through a comparison of pressure distributions over the rotor and stator blade surfaces with published[71] data. The normalized surface pressure distributions at 50% span from the hub are shown in Figure 4.27. The present simulations reproduce the expected trend over the stator and the rotor blade rows and all five methods produce nearly identical behavior over both the stator and rotor. Thus, it may be concluded that as far as blade loading (pressures, temperature, skin friction, and heat transfer) effects are concerned, there is no particular advantage to using one method over another.

To conclude this section, five different averaging plane approaches for stator-rotor interface boundary conditions have been evaluated. It is shown that all of these approaches give a nearly identical convergence characteristics and blade surface pressure distributions indicating that the underlying average method yields useful time averaged solution. It is also shown that IBC1, IBC4 and IBC5 preserve the mass flow rate at the interface better than IBC2 and IBC3. However, only the IBC5 approach (characteristic boundary condition approach) preserves some of the non-uniformity spatial details of the flow without the smearing associated with the averaging process and allows the continuity of the flow variables at the stator blade row exit. It is therefore recommended

that the IBC5 approach be used in future studies over the other averaging plane approaches investigated in the current work.

Table 4.1: Summary of averaging plane interface boundary conditions.

	Outflow (Stator Block) Face AB	Inflow (Rotor Block) Face CD
IBC1	$(\overline{\rho_S}, \overline{u_S}, \overline{v_S}, \overline{w_S})$ $(\overline{p_R})$	$(\overline{p_R})$ $(\overline{\rho_S}, \overline{u_S}, \overline{v_S}, \overline{w_S})$
IBC2	(ρ_S, u_S, v_S, w_S) $(\overline{p_R})$	$(\overline{p_R})$ $(\overline{\rho_S}, \overline{u_S}, \overline{v_S}, \overline{w_S})$
IBC3	$\left(\overline{\rho_R}, \overline{u_R}, \overline{v_R}, \overline{w_R}, \overline{p_R}\right)$	$\left(\overline{\rho_S}, \overline{u_S}, \overline{v_S}, \overline{w_S}, \overline{p_S}\right)$
IBC4	$\frac{1}{2}\begin{pmatrix} \overline{\rho_S}+\overline{\rho_R} \\ \overline{u_S}+\overline{u_R} \\ \overline{v_S}+\overline{v_R} \\ \overline{w_S}+\overline{w_R} \\ \overline{p_S}+\overline{p_R} \end{pmatrix}$	$\frac{1}{2}\begin{pmatrix} \overline{\rho_S}+\overline{\rho_R} \\ \overline{u_S}+\overline{u_R} \\ \overline{v_S}+\overline{v_R} \\ \overline{w_S}+\overline{w_R} \\ \overline{p_S}+\overline{p_R} \end{pmatrix}$
IBC5	$\rho = \rho_S$ $u = u_S$ $v = v_S$ $w = w_S$ $p = \frac{1}{2}[\overline{p_R} + p_S + \overline{\rho_R}.\overline{a_R}.(u_S - \overline{u_R})]$	$C_{5R} = -\overline{\rho_S}.\overline{a_S}.(u_R - \overline{u_S}) + (p_R - \overline{p_S})$ $\rho = \overline{\rho_S} + \frac{C_{5R}}{2\overline{a_S}^2}$ $u = \overline{u_S} - \frac{C_{5R}}{2\overline{\rho_S}.\overline{a_S}}$ $v = \overline{v_S}$ $w = \overline{w_S}$ $p = \overline{p_S} + \frac{1}{2}.C_{5R}$

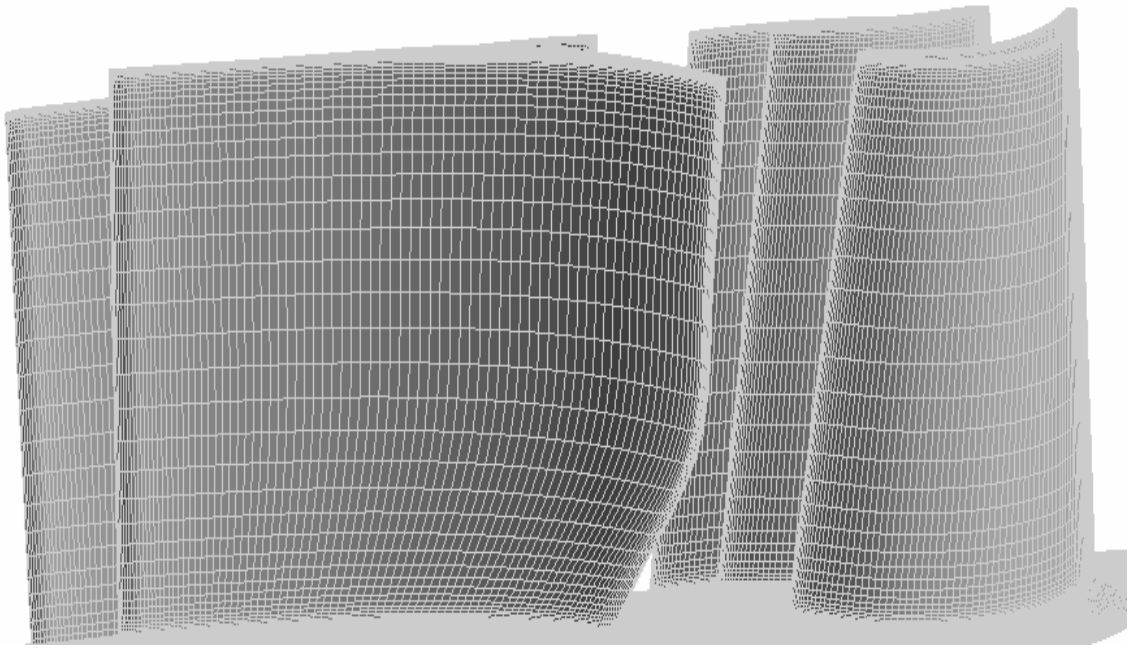

Figure 4.22: Two block (127x45x45) H-grid for the first stage of the SSME turbine.

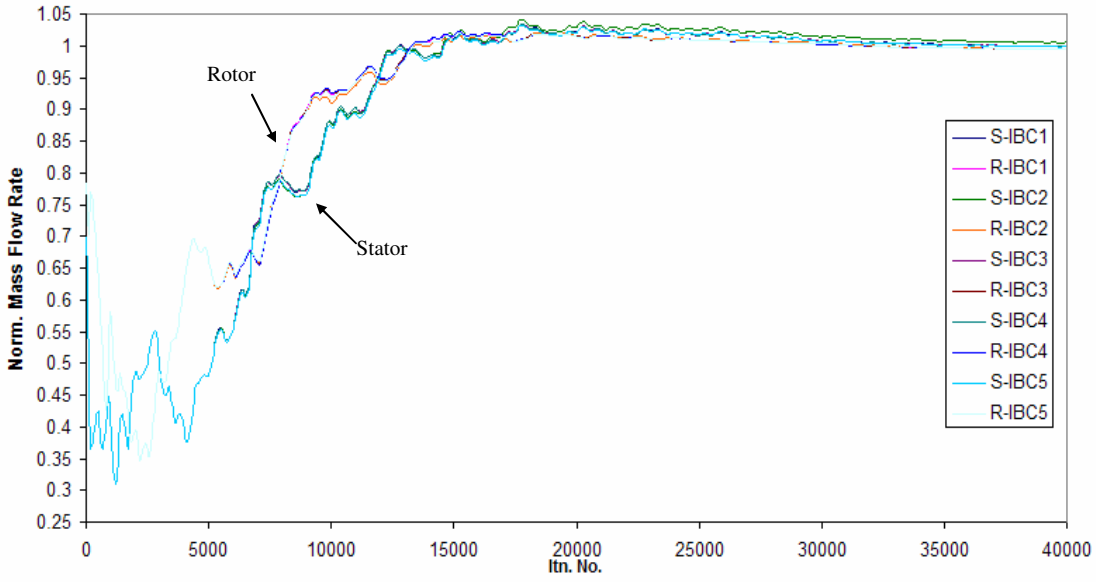

Figure 4.23: Non-dimensional mass flow rate convergence history for the IBC1-IBC5 schemes.

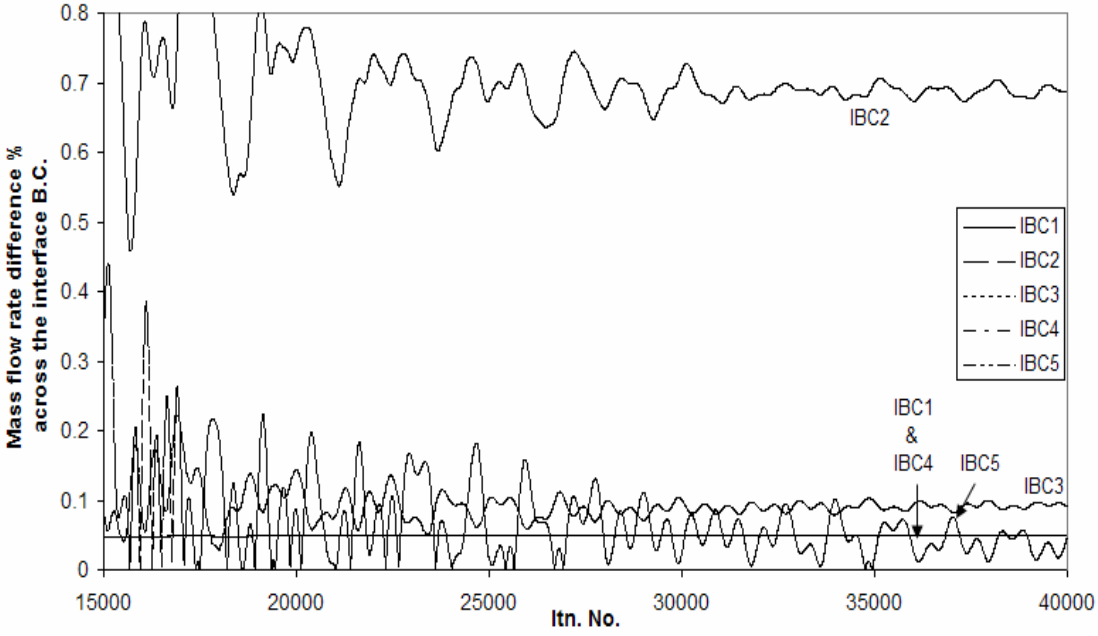

Figure 4.24: Variation of mass flow rate difference with time across the interface B.C.

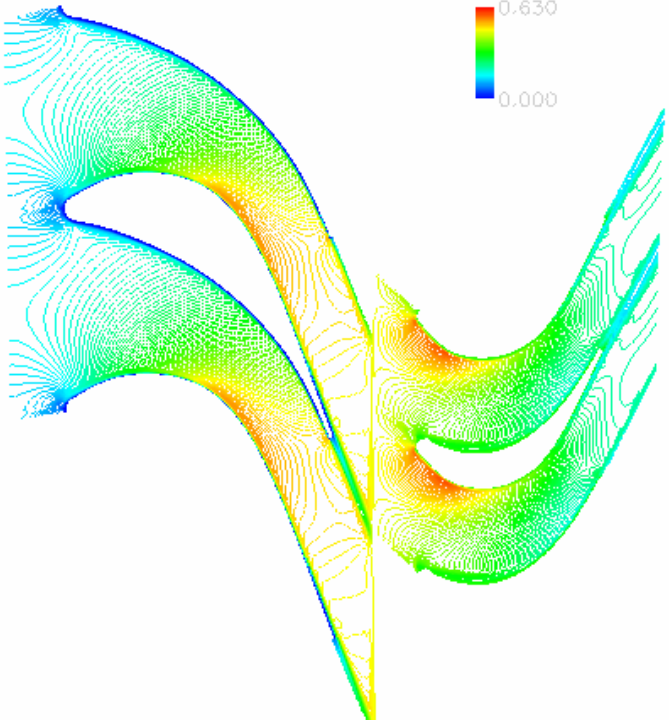

a) GT-TURBO3D using IBC1

Figure 4.25: Mach number contours at mid span for the first stage of the SSME turbine.

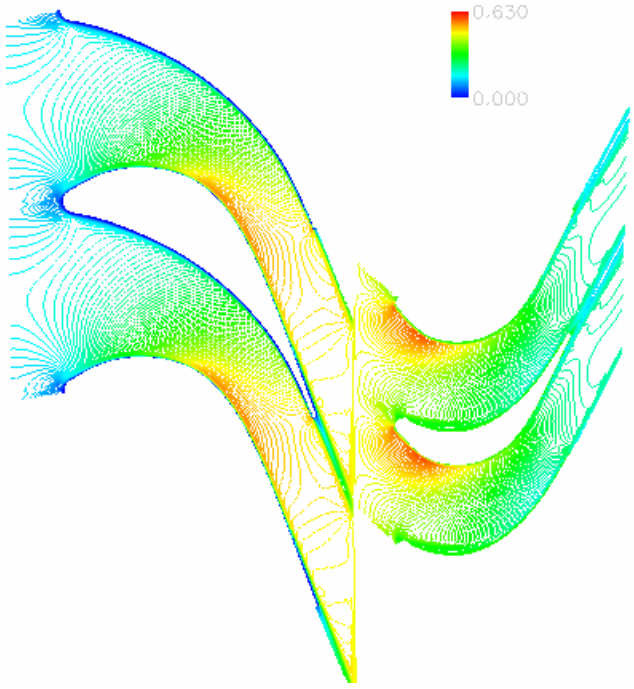

b) GT-TURBO3D using IBC3

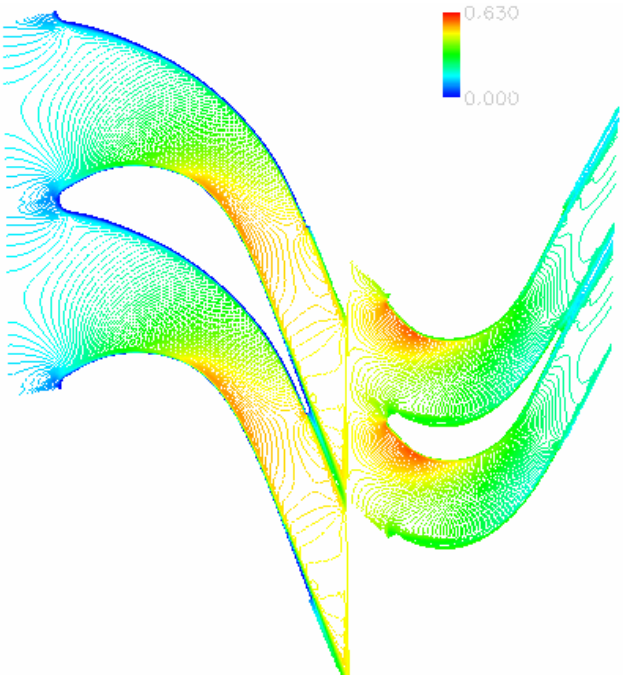

c) GT-TURBO3D using IBC4

Figure 4.25 (cont.): Mach number contours at mid span for the first stage of the SSME turbine.

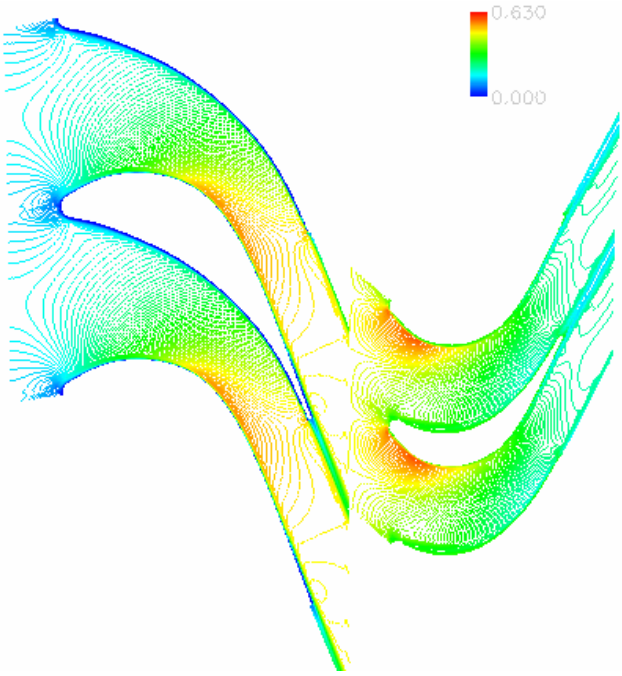

d) GT-TURBO3D using IBC5

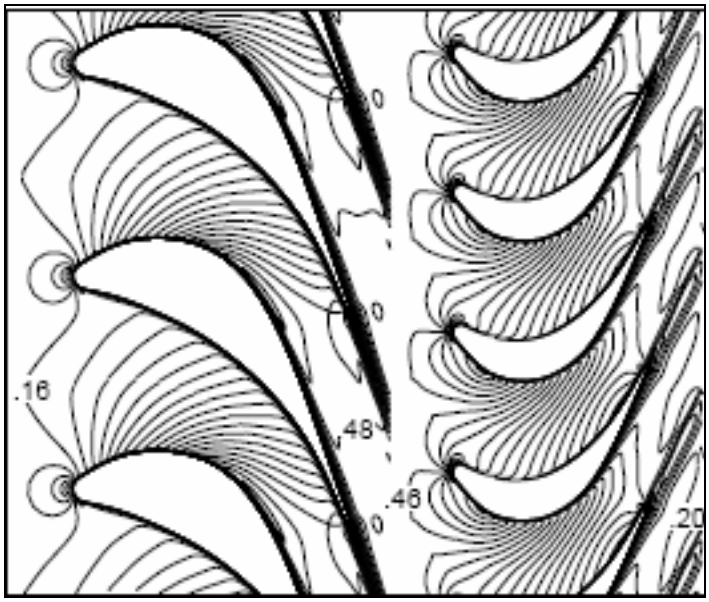

e) Swift code by Chima[71]

Figure 4.25 (cont.): Mach number contours at mid span for the first stage of the SSME turbine.

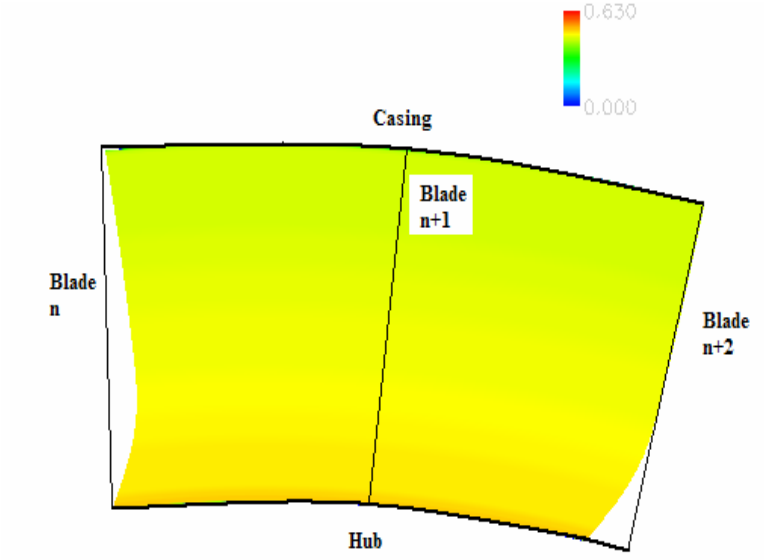

a) GT-TURBO3D using IBC1

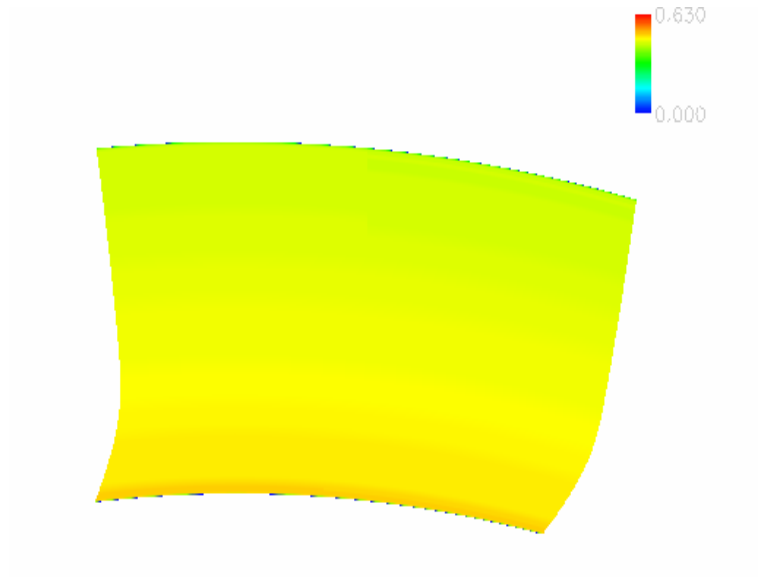

b) GT-TURBO3D using IBC3

Figure 4.26: Mach number contours at the rotor-stator interface for two adjacent blade passages.

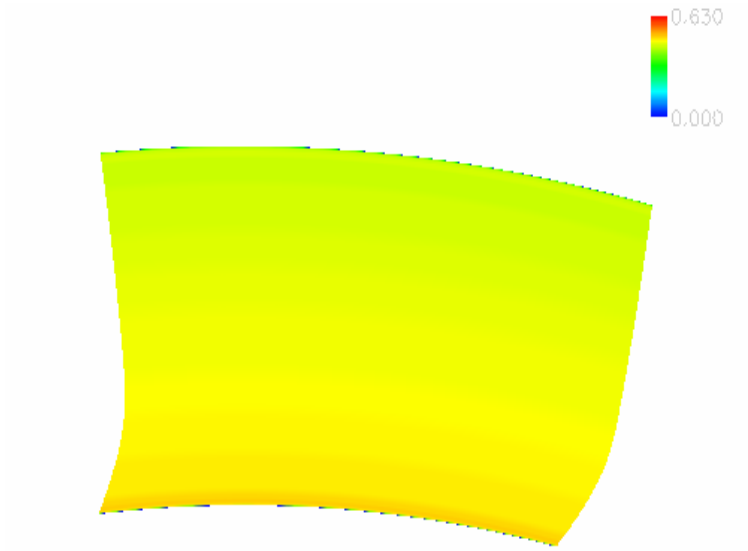

c) GT-TURBO3D using IBC4

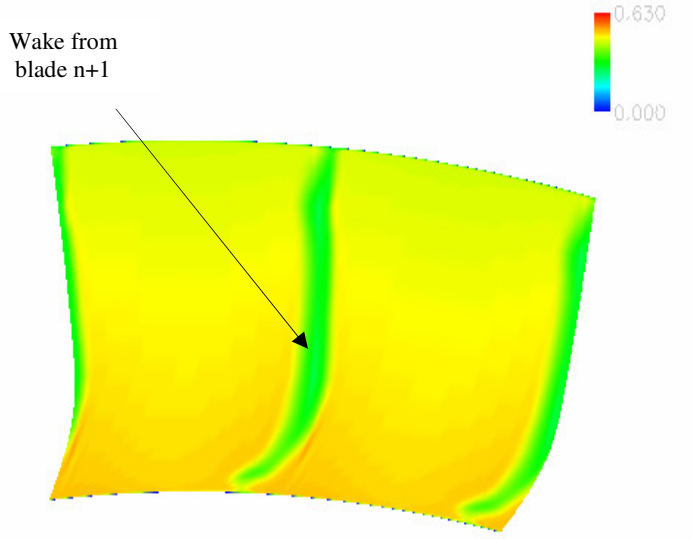

d) GT-TURBO3D using IBC5

Figure 4.26 (cont.): Mach number contours at the rotor-stator interface for two adjacent blade passages.

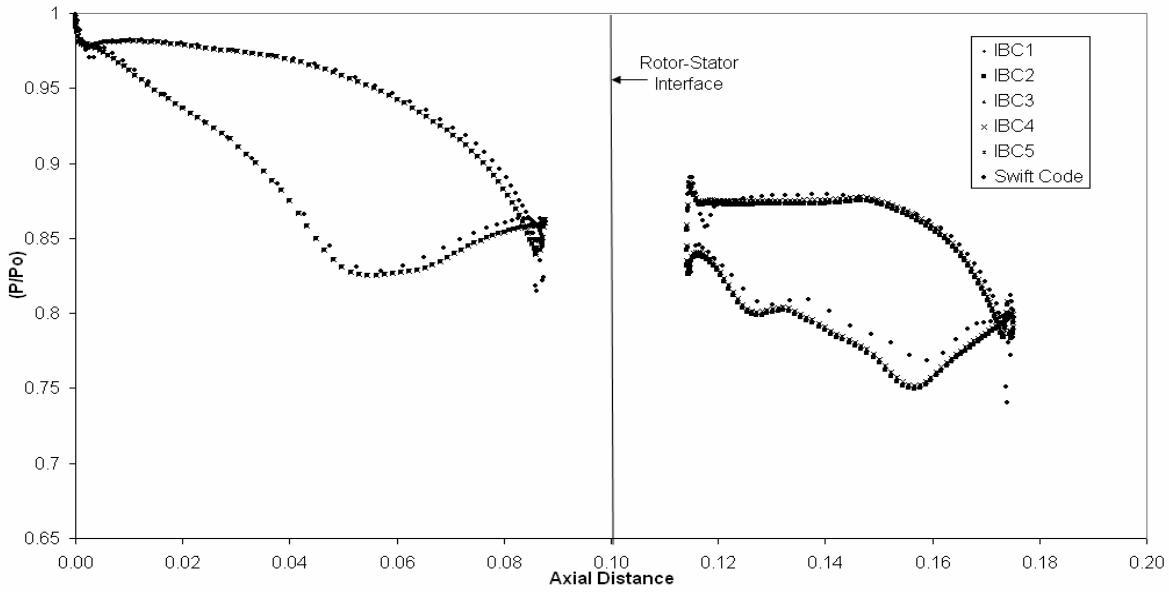

Figure 4.27: Normalized pressure distribution at mid span of the first stage of the SSME turbine.

4.5.2 Unsteady Sliding Mesh Interface Boundary Condition:

As showed in the previous section, while the averaging plane methods have the advantage of conserving mass, momentum, and energy at each radial location in a global sense, and by using a characteristic boundary conditions approach (as in IBC5), the continuity of the flow variables at the rotor-stator interface is not achieved. The underlying averaging precludes the proper transfer of locally separated pockets of flow between stages, preventing the use of these methods from modeling the spatial propagation of stall cells between stages. To overcome these limitations, an unsteady sliding mesh[61] (USM) is implemented and validated in the current methodology.

The global convergence characteristic of the USM interface boundary condition approach is first examined. Figure 4.28 shows the convergence history of the normalized

mass flow rate ($\dot{m}/\dot{m}_{design}$) for the stator block and the rotor block. The USM approach has a good convergence characteristic and the stator and rotor blocks asymptotically converge to the same mass flow rate to within 1% of each other. The periodic oscillations seen in the mass flow rate is a characteristic of the unsteady sliding mesh. The discrepancy between the computed and the measured mass flow rate is also within 1%.

Next, the flow field inside the rotor-stator passages is examined through a study of the Mach number contours. The Mach number contours at 50% span from the hub are shown in Figure 4.29. The smooth and continuous Mach number contours across the interface boundary indicate that the USM approach captures and retains the azimuthal details such as those of the Mach number deficit associated with the wake from the stator blades. Thus, it can be concluded that the USM approach preserves the flow non-uniformity between the stator and rotor blade rows.

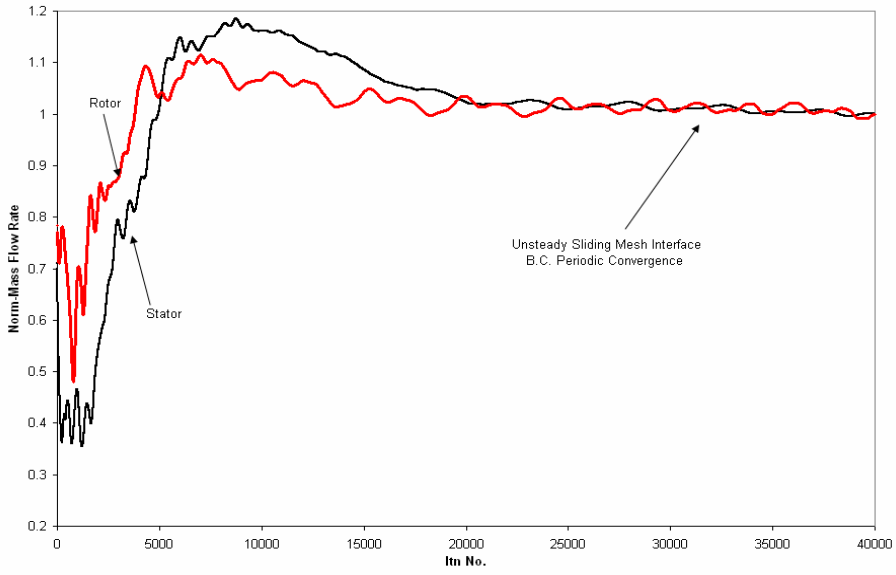

Figure 4.28: Non-dimensional mass flow rate convergence history for the USM interface BC.

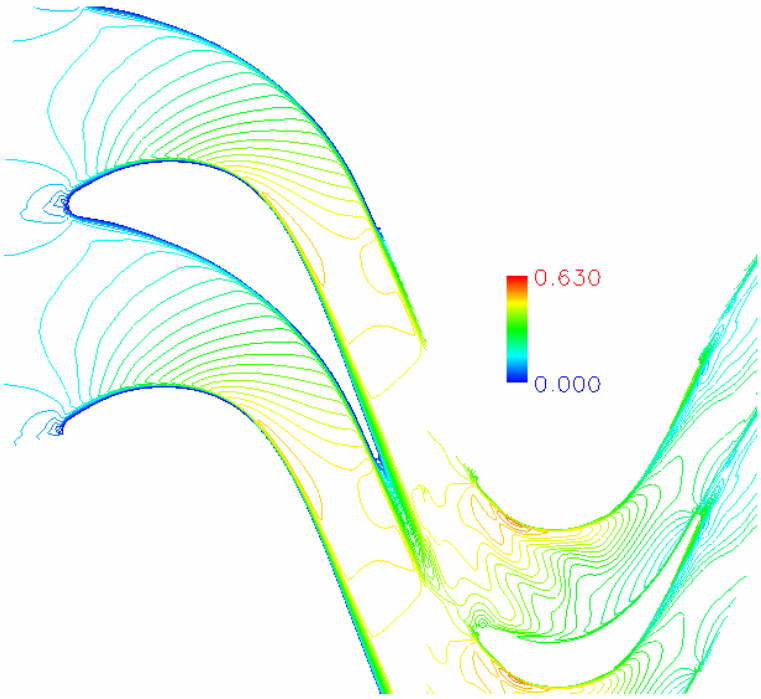

Figure 4.29: Mach number contours at mid span for the first stage of the SSME turbine using USM.

CHAPTER 5

COMPRESSOR STAGE STUDIES

As stated earlier, the present analysis solver (GT-TURBO3D) has been extensively validated for wind turbines, prop-fans, fixed wing configurations, and single-stage axial and radial compressors configurations (NASA Rotor 37, NASA Rotor 67, NASA low speed centrifugal compressor, etc).[73-76]As demonstrated in the previous chapter, this solver is validated for several airfoils (RAE2822 and NACA0015), two axial turbine configurations (Goldman turbine vane, SSME turbine stage), and an axial compressor configuration (NASA Rotor 67). Also, limited grid independency studies are done for the RAE2822 airfoil and for the Goldman turbine vane. From these studies, it is believed that the current analysis using the specified grid densities are grid independent.

In this chapter, the present methodology is applied to study the flow mechanism behind stall inception in the NASA Stage 35 compressor configuration as a representative of a modern transonic compressor stage. NASA Stage 35 is a transonic inlet stage for a core compressor (a rotor followed by a stator), and has been widely used by several researchers. This stage was originally designed and tested at NASA Glenn Research Center by Reid et al.[84] This compressor stage has a design pressure ratio of 1.82 at a mass flow rate of 20.19 kg/sec and has a rotor tip speed of 455 m/sec. The rotor has 36 multiple-circular-arc blades with a maximum radius of 9.94 cm, a hub to tip ratio of 0.7, an aspect ratio of 1.19, and a tip solidity of 1.288. The stator has 46 multiple-circular-arc blades with an aspect ratio of 1.26.

The grid used in the current work is shown in Figure 5.1. It is a two block (rotor block and stator block) H-grid with 180 cells in the axial direction, 49 in the radial direction, and 54 cells in the azimuthal direction. This grid is generated using the grid generator code TCGRID.[80] The tip clearance gap is modeled using a simple periodicity model rather than gridding the clearance gap in a separate mesh block to reduce the computational cost. This is considered adequate for the prediction of the tip vortex strength, trajectory, and extent as indicated by Chima[25] and followed by other researchers.[85]

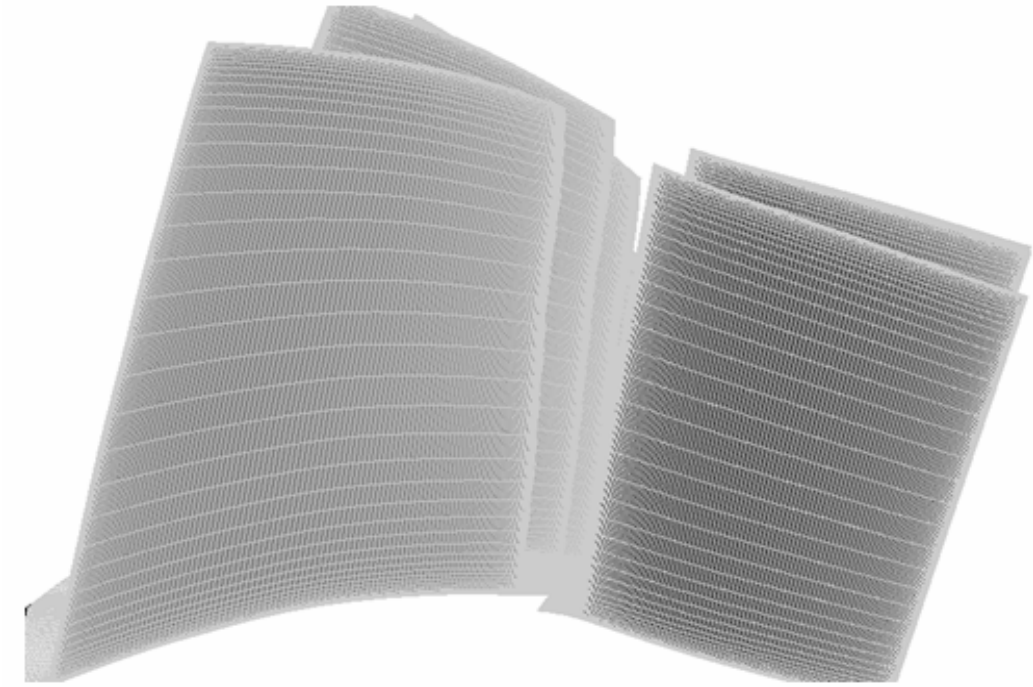

a) NASA Stage 35 grid overview

Figure 5.1: Two block (180x49x54) H-grid for the NASA Stage 35 compressor configuration.

b) Blade to blade grid at mid-span

Rotor Stator

c) Blade to blade grid near the leading edge

Figure 5.1 (cont.): Two block (180x49x54) H-grid for the NASA Stage 35 compressor configuration.

At the rotor-stator interface, unsteady sliding mesh (USM) interface boundary conditions are used in the current analysis rather than using the characteristic interface boundary conditions (IBC5 - Table 4.1). As shown in the previous chapter, the sliding mesh interface boundary conditions used here ensure that the local flow information propagates correctly between the successive blade rows because it does not include any averaging at the interface boundary. Figure 5.2 shows the entropy contours at the mid-span of the compressor stage. As shown in this figure, the rotor wake is preserved across the rotor-stator interface with a slight dissipation due to the interpolation between the two sides of the interface boundary. The rotor wake skewing and stretching while passing through the stator blade passage can also be observed in this figure.

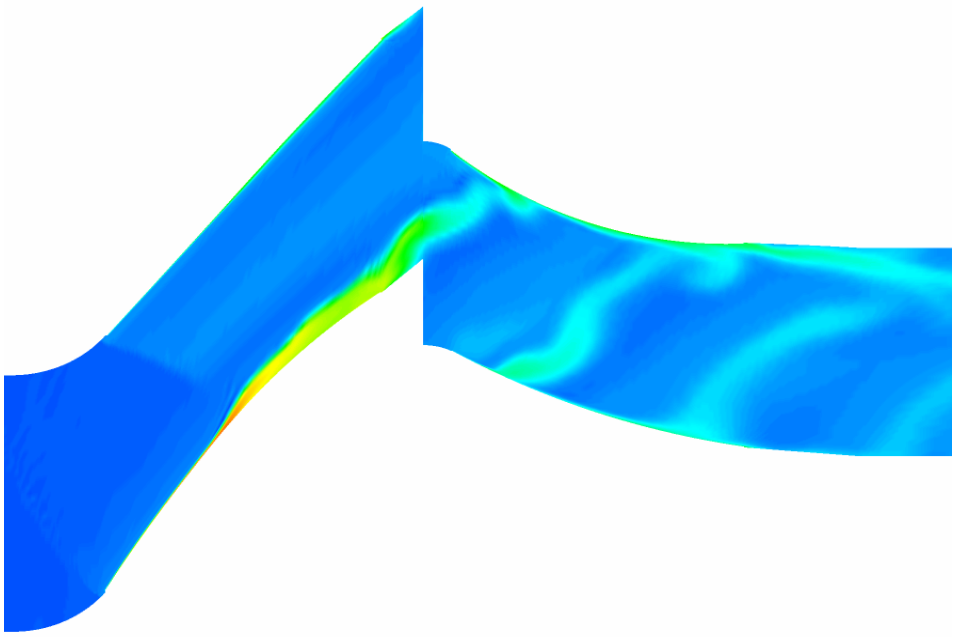

Figure 5.2: Entropy contours for the NASA Stage 35.

To study the flow structure as the compressor marches towards stall, the flow fields along a compressor speed line are simulated. A single blade passage is modeled here assuming blade passage to blade passage periodicity. Although full annulus analysis is needed to simulate the compressor rotating stall inception, similar flow phenomena can occur in a single blade passage during actual rotating stall inception[26] while requiring much lower computational resources. This assumption is considered adequate up to the stall inception point.[86] There are usually two approaches followed to simulate a compressor speed line. The first approach is done by running the compressor to a targeted mass flow rate and letting the static back pressure float; while the second approach is done by running the compressor to a fixed static back pressure and letting the mass flow rate float. In the present simulations, the second approach is followed, where the stage characteristics are generated by running different simulations to different static back pressures. First, the near choke condition flow points are run to low static back pressure values and then the solutions are restarted with incrementally increasing the static back pressure to compute the intermediate points on the speed line towards stall. Then, near stall, the static back pressure is increased with very small increments.

As shown in the previous chapter, predictions using the HRKES2 model option (using the blending function F_2 and the realizability constraints to bound the KES model parameters - Table 3.1) were more accurate than the other HRKES model options compared to the experimental measurements. Therefore, the simulations presented in this chapter are carried out using the baseline k-ω-SST turbulence model and the Hybrid

RANS/KES turbulence model HRKES2 (the '2' in 'HRKES2' will be dropped from now on and it will be referred to as 'HRKES').

Figure 5.3 shows the mass flow rate convergence history using k-ω-SST and HRKES turbulence models at the near choking condition. Each simulation is run for 4 cycles and the convergence history is shown for the last 1/3 cycle. As shown, both turbulence models have the same convergence characteristics and their solutions reached cyclic convergence. Since the current simulations are unsteady, time averaged solutions are obtained by averaging over multiple time steps after the cyclic convergence is achieved. The computed choked mass flow rates are 20.93 kg/sec and 20.89 kg/sec using k-ω-SST and HRKES models, respectively, which are within a difference of less than 0.3% compared to the measured choking mass flow rate of 20.95 kg/sec.

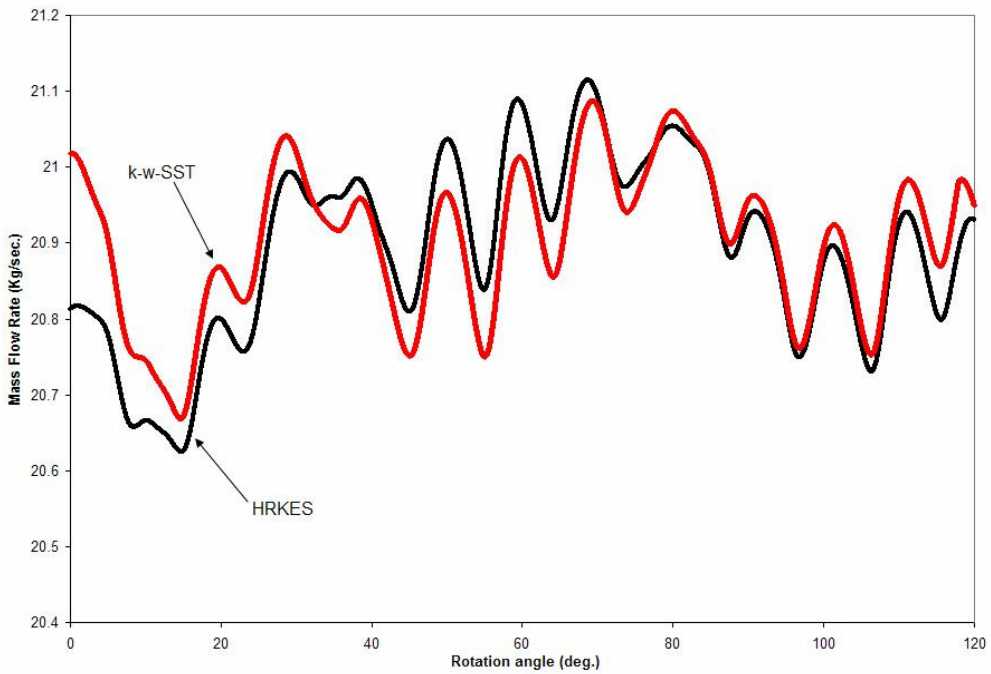

Figure 5.3: Mass flow rate convergence history for NASA Stage 35 near choking.

Figure 5.4 shows the compressor stage's computed and measured[84] characteristics at the design rotational speed using both the k-ω-SST and the HRKES turbulence models. On the vertical axis, the total pressure ratio rise across the compressor stage is plotted against the normalized mass flow rate ($\dot{m}/\dot{m}_{choked}$) on the horizontal axis and compared to the experimental data. As mentioned above, the compressor stage's characteristics are generated by running different simulations to different static back pressures. First, the near choke condition flow points are run to low static back pressure values and then the solutions are restarted with incrementally increasing the static back pressure to compute multiple points on the speed line towards stall. Figure 5.4 shows that the computational results and the computed characteristic line shape agree well with the experimental[84] results for both the k-ω-SST and HRKES turbulence models except in the vicinity of stall. For the HRKES model simulations, point A represents the near design operating condition, point B represents the near stall operating condition, and point C is in stall condition. Figure 5.5 shows the mass flow rate convergence history for points A, B, and C. Increasing the static back pressure after point B causes the compressor to stall, while the k-ω-SST model simulations do not capture the compressor stall for the same static back pressure conditions. Figure 5.6 shows the normalized variance in the mass flow rate (Var/Var_{choked}) using the HRKES turbulence model plotted against the normalized mass flow rate ($\dot{m}/\dot{m}_{choked}$). It is observed that as the mass flow rate through the compressor decreases and the compressor approaches stall, the fluctuations in the mass flow rate increase slowly until near stall where it increases rapidly. Thus, monitoring these fluctuations can be used to detect the onset of stall.

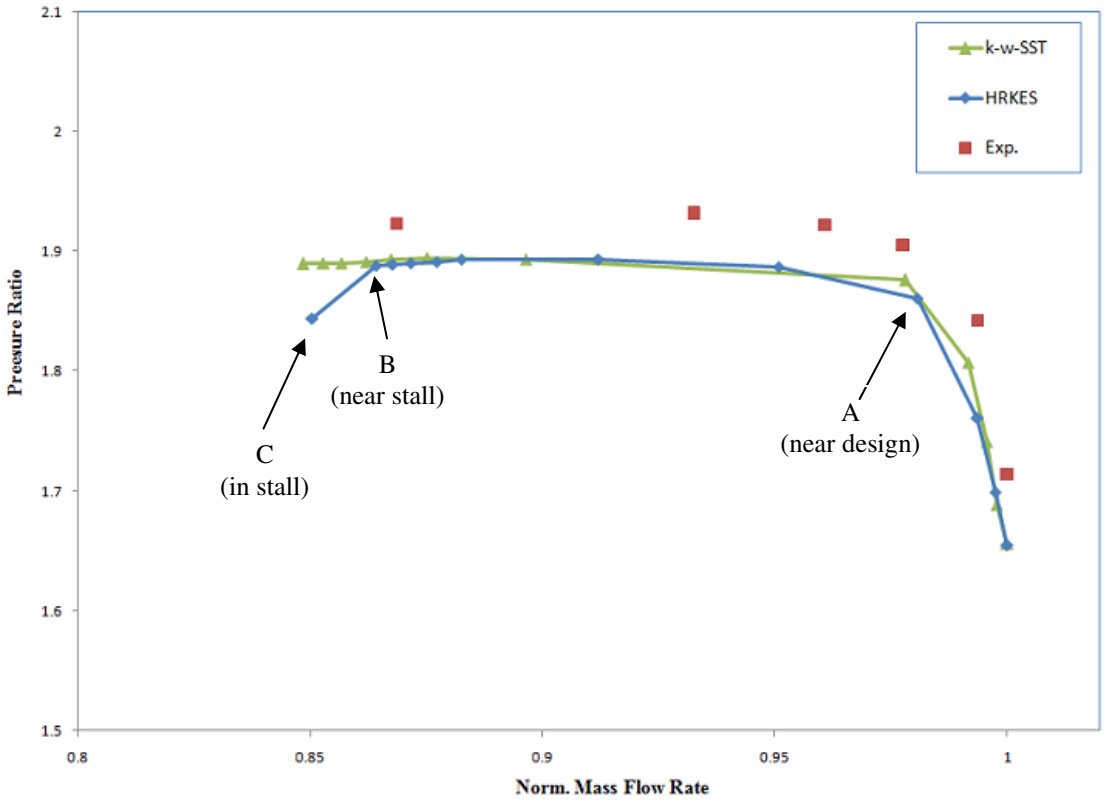

Figure 5.4: NASA Stage 35 compressor speed line.

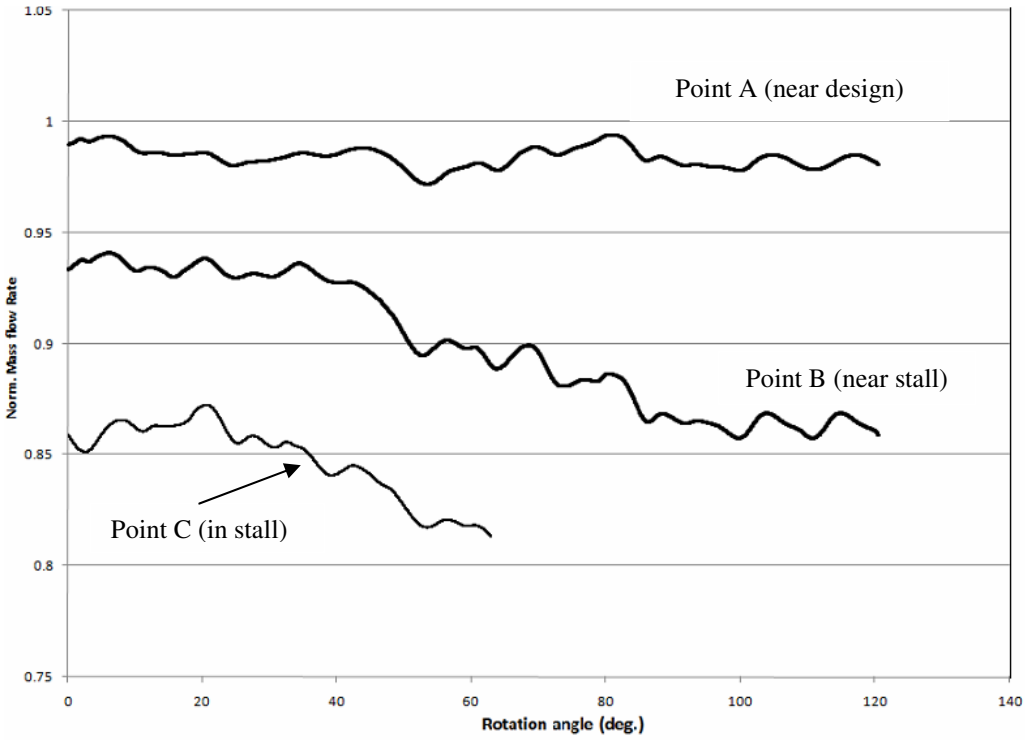

Figure 5.5: Mass flow rate convergence history for NASA Stage 35 operating points A, B, and C.

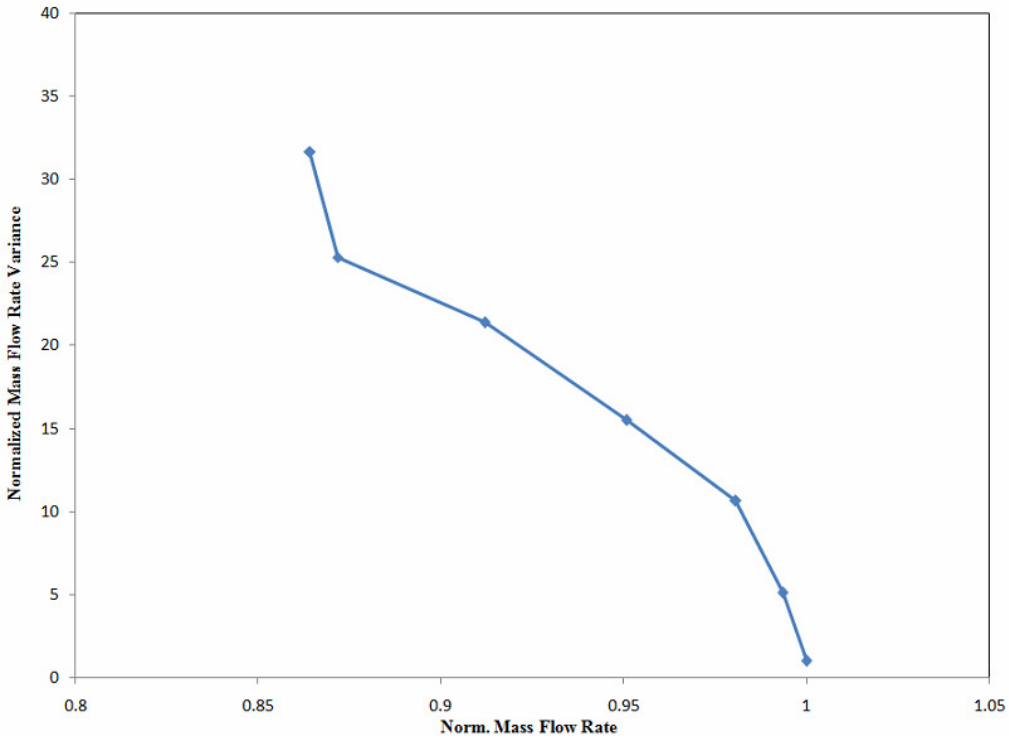

Figure 5.6: Normalized mass flow rate variance for NASA Stage 35.

As mentioned in Chapter 2, the tip clearance flow plays a very important role in compressor stall inception and the interactions between the shock wave and the tip clearance flow have been identified by researchers as the primary cause behind stall inception in transonic compressors. Furthermore, earlier experimental investigations (Suder et al.[88]) and numerical studies (Chen et al.[85]) indicated that stall initiates in the tip region of the rotor for this compressor stage. Therefore, to explore the flow mechanisms and the physical trends leading to stall inception, the role of the tip clearance flow and the shock wave as the compressor throttles towards stall is examined by investigating the answers to the following questions:

- What is the behavior of the shock wave?
- What is the behavior of the rotor tip clearance flow?
- How does the rotor tip clearance flow interact with the shock wave?
- Does the shock boundary layer interactions cause flow separation?

In order to answer these questions, the averaged flow fields at two operating points A and B along the compressor speed line shown in Figure 5.4 are studied. Point A represents the near design operating condition and point B represents the near stall operating condition. The flow field in the rotor tip region for both operating points A and B is analyzed in detail. The current simulations are carried out using the k-ω-SST and HRKES turbulence models. Only the simulations obtained using the HRKES model are analyzed here, given the superior behavior of the HRKES model compared to the k-ω-SST model, as discussed earlier. The results shown in the current work are obtained from single passage simulations and duplicated over two neighboring blade passages for better visualization.

First, the shock wave and tip clearance flow and their interactions are investigated. Figure 5.7, Figure 5.8, and Figure 5.9 show the non-dimensional static pressure contours, which are independent of the frame of reference, at the tip section of the rotor blade, in the tip clearance region and on the casing walls, respectively, and at corresponding stator span sections for both operating points A and B. Because of the transonic nature of the flow, supersonic flow appears when the rotor rotational velocity is combined with the main flow axial velocity, and the relative Mach number exceeds unity which leads to the formation of shock waves. Tip vortices and tip clearance leakage flow are generated in

the flow due to the pressure difference between the pressure side and the suction side of the rotor blade in a similar manner to the formation of the aircraft wing tip vortices. High pressure flow from the blade's pressure surface rolls over the blade tip to reach the lower pressure flow over the blade's suction surface. The lower axial momentum rotor tip leakage flow interacts with the main axial flow creating a vortex sheet which rolls up into the leakage vortex as it travels downstream. The formation of the tip leakage flow vortex reduces the effective main flow stream area and adds more blockage to the flow passage. As the mass flow rate through the compressor decreases, the angle of the tip vortex will increase, impinging at a more forward location on the adjacent rotor blade surface. This can cause the flow to spill over the adjacent blade leading edge and induce stall. [19, 87]

As the compressor throttles towards stall from the near design operating point A to the near stall operating point B, as shown in Figure 5.7 through Figure 5.9, the following flow phenomena are identified. In those figures, darker regions represent low pressure areas and lightly shaded regions correspond to high pressure areas. In Figure 5.7a, for the near design operating point A, the low pressure area (very dark) extending from the rotor tip till mid-passage represents the tip clearance leakage flow vortex as it travels downstream. This figure shows that the shock wave is very close to the rotor leading edge and the shock front is uniform. The shock wave passes continuously across the passage where it intersects the tip vortex and bends. The shock wave then continues until it intersects the rotor suction surface. In Figure 5.7b, for the near stall operating point B, the low pressure area (very dark) near rotor tip represents the tip clearance leakage flow vortex as it travels downstream. This figure shows that the shock wave is stronger and it

stands further upstream from the rotor leading edge compared to the near design condition. The shock wave front becomes non-uniform which indicates the high unsteadiness of the shock wave at the near stall condition. The shock wave passes continuously across the passage where it intersects the tip vortex closer to the rotor blade suction surface compared to the near design condition. The shock wave then bends before intersecting the rotor suction surface further upstream compared to the near design condition. Figure 5.8 and Figure 5.9 show the non-dimensional static pressure contours in the tip clearance region and on the casing walls, respectively, for both operating points A and B. Those figures show similar flow structure to that observed in Figure 5.7.

Figure 5.10 shows the rotor tip clearance flow stream lines for the two operating points A and B. By looking at the rotor tip clearance flow stream lines in Figure 5.10a, for the near design operating point A, it is observed that only the forward 20% of the tip leakage flow emerges to form the tip leakage flow vortex core. The vortex interacts with the shock wave near the mid-passage plane. The interaction between the shock wave and the tip vortex is not strong and it slightly alters the shape and trajectory of the vortex. The trajectory of the vortex is not perpendicular to the axial flow direction and the shock wave has a minor impact on the tip vortex trajectory. In Figure 5.10b, for the near stall operating point B, it is again observed that only the forward 20% of the tip leakage flow emerges to form the tip leakage flow vortex core, which is now moved further ahead compared to the near design condition. Due to the high blade loading at near stall condition, which implies a larger pressure difference between the pressure surface and the suction surface of the rotor blade near the tip, the tip vortex is larger in size compared

to the near design condition. The vortex interacts with the shock wave closer to the rotor suction surface. The interaction between the shock wave and the tip vortex is strong and it impacts the shape and trajectory of the vortex. The center portion of the vortex now becomes perpendicular to the axial flow direction. This trend agrees well with the stall inception criterion of Hoying et al.[87] In their work, Hoying et al.,[87] using vortex kinematics analysis, developed a criterion for stall inception when the trajectory of the tip clearance vortex becomes perpendicular to the axial flow direction.

Figure 5.11 shows the flow field entropy contours in the blade to blade mid-passage plane and at the rotor blade leading edge plane for the near design operating point A and the near stall operating point B. In this figure, darker regions represent low entropy areas and lightly shaded regions correspond to high entropy areas. Entropy rises in the tip vortex and this can be observed clearly. Looking at the rotor leading edge plane, the entropy increases at the near stall condition as compared to the near design conditions. This low momentum flow region near the rotor blade tip leading edge will cause the flow spillage over it. For the near design condition, Figure 5.11a shows that the shock wave interactions with the tip vortex are not strong. On the other hand, for the near stall condition, Figure 5.11b shows that the rotor blade tip vortex is larger in size and its interactions with the shock wave are stronger at near stall compared to the near design condition. The velocity vectors near the casing walls will be examined later at this plane for the possibility of shock wave induced flow separation. Figure 5.11 also shows the entropy rise across the rotor blade passage at the tip at the near stall condition which was also indicated by Chima[89] for this compressor configuration.

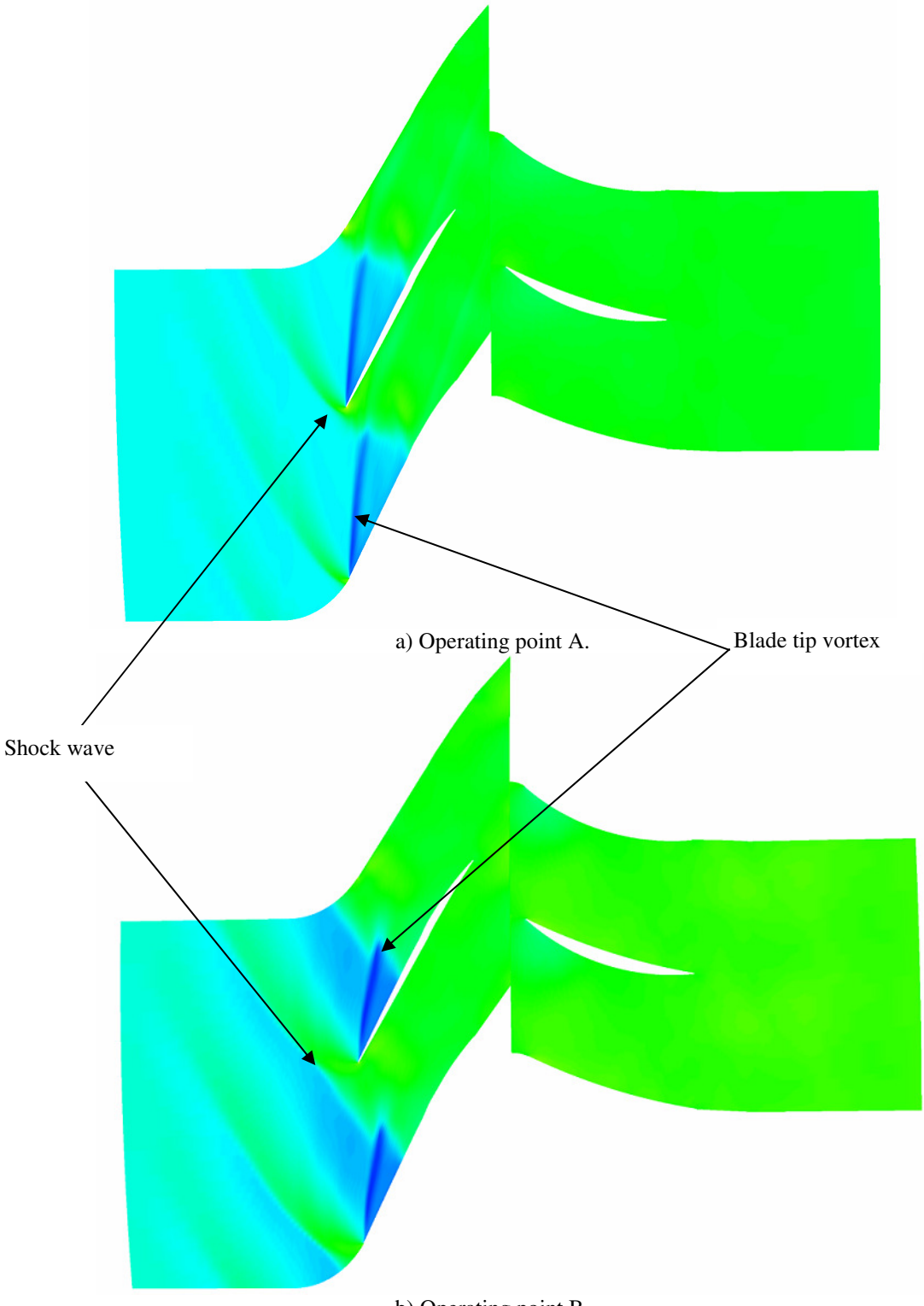

Figure 5.7: Static pressure contours at the tip section for NASA Stage 35.

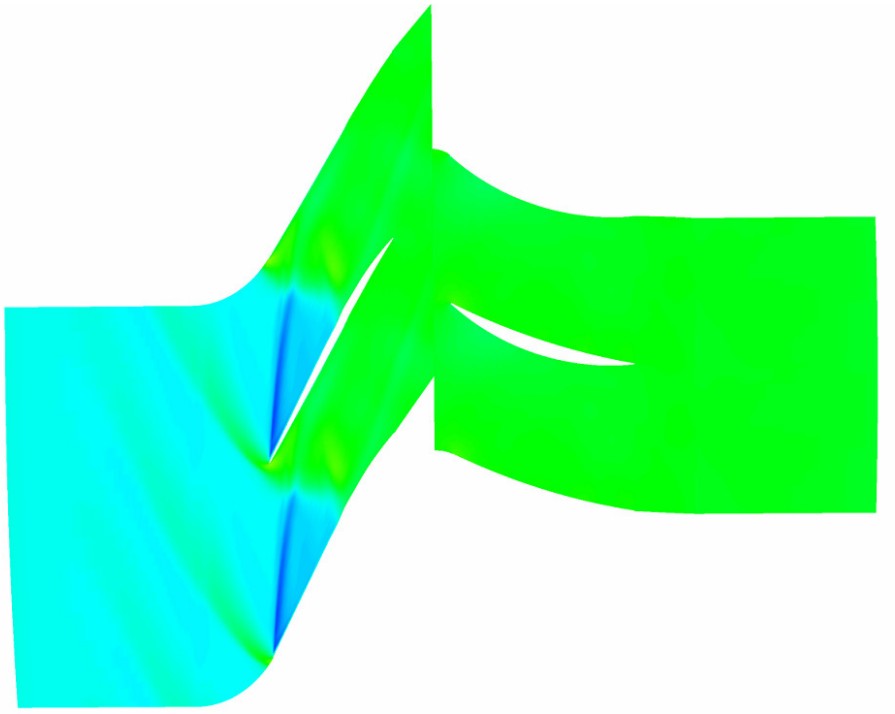

a) Operating point A.

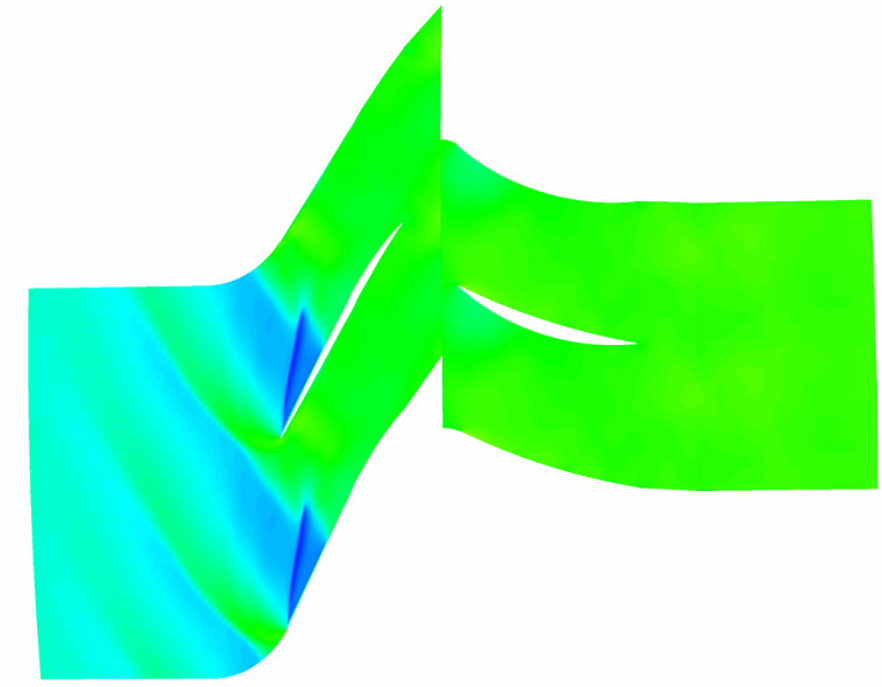

b) Operating point B.

Figure 5.8: Static pressure contours in the tip clearance for NASA Stage 35.

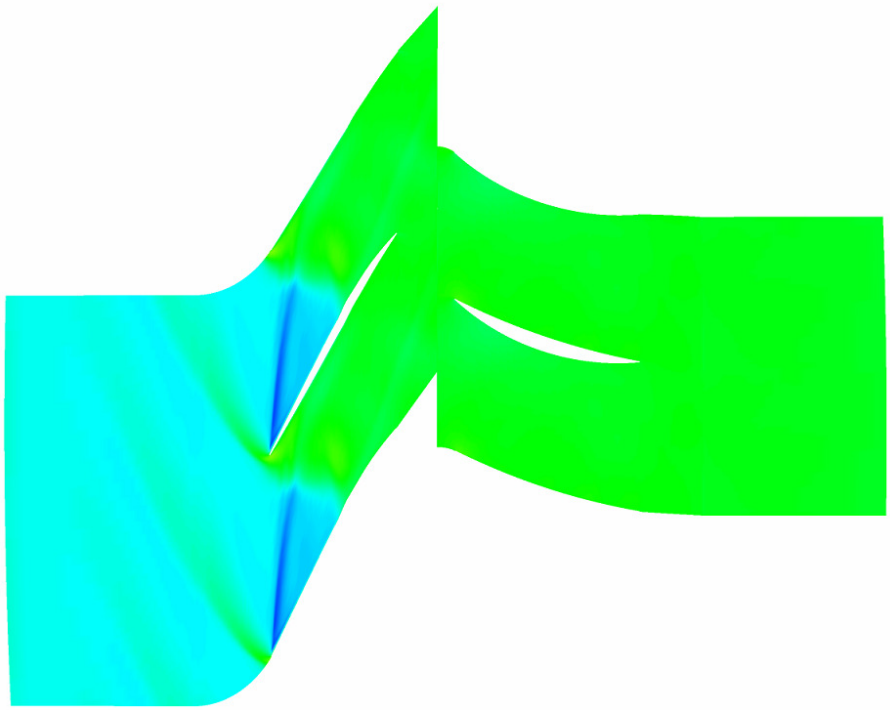

a) Operating point A.

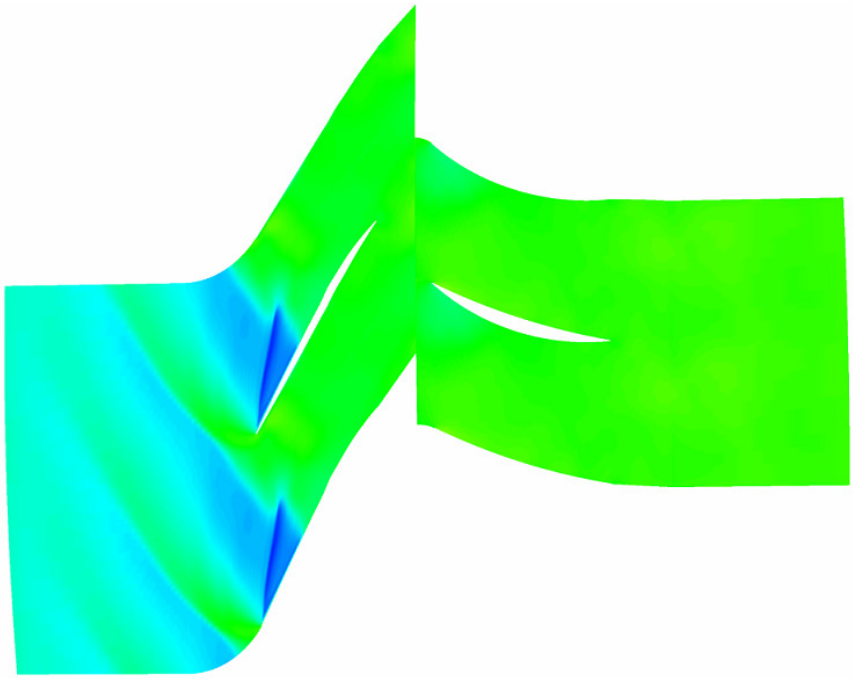

b) Operating point B.

Figure 5.9: Static pressure contours on the casing walls for NASA Stage 35.

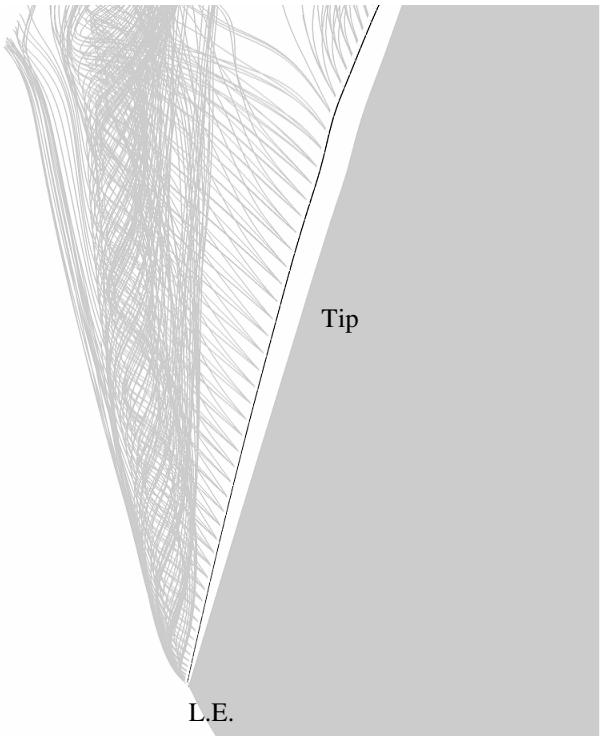

a) Operating point A.

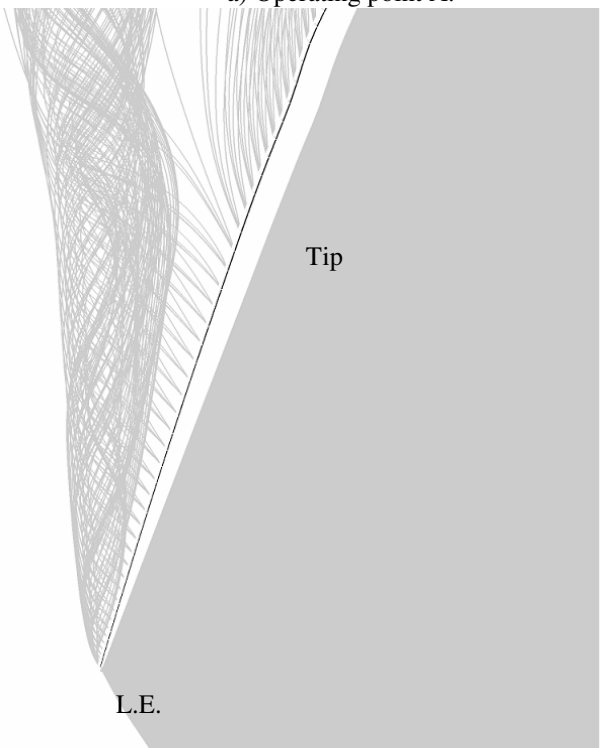

b) Operating point B.

Figure 5.10: NASA Stage 35 rotor tip leakage flow stream-lines.

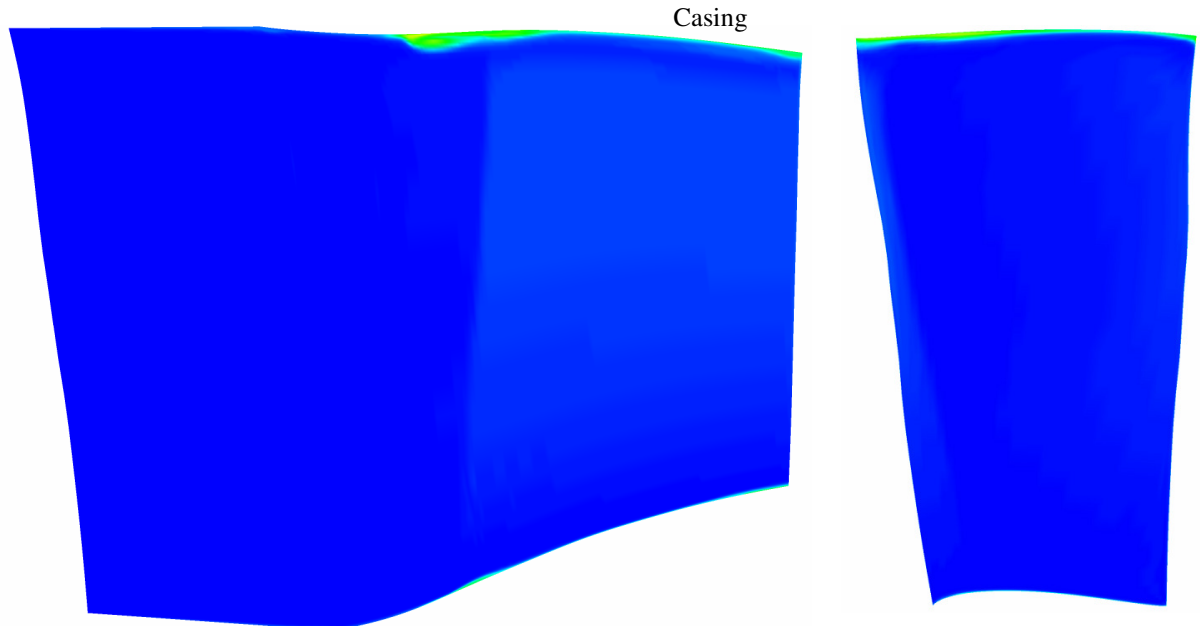

a) Operating point A.

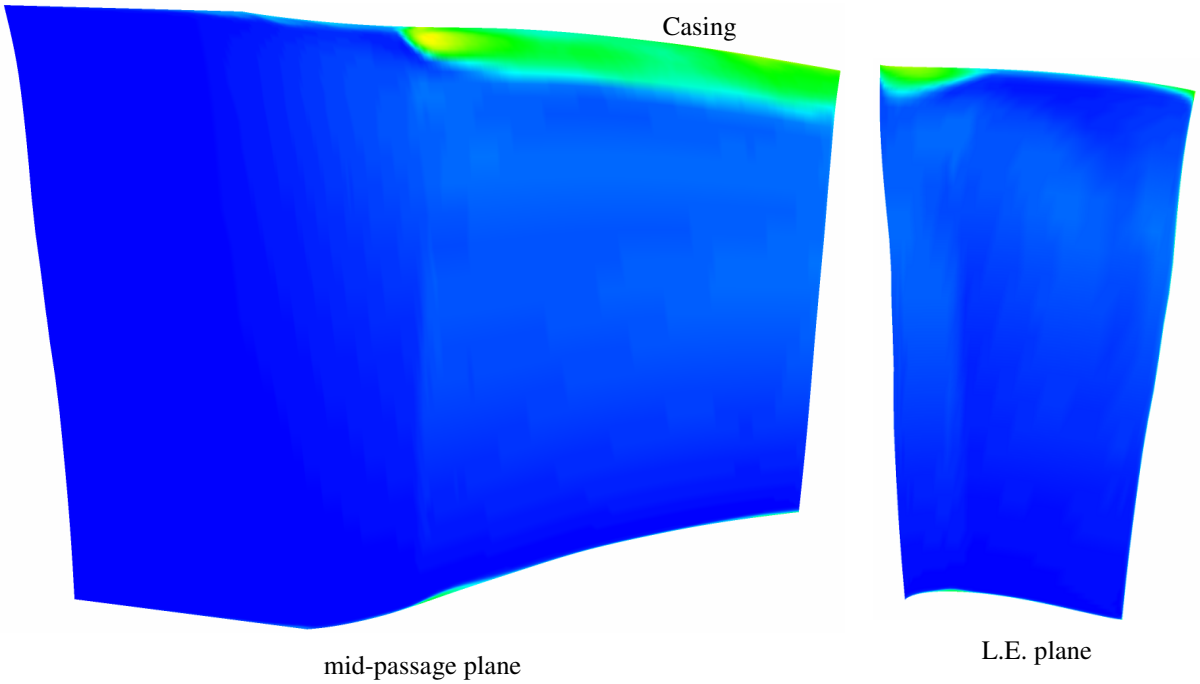

b) Operating point B.

Figure 5.11: Entropy contours at the NASA Stage 35 rotor mid-passage plane.

Furthermore, when a shock wave interacts with a boundary layer, the low momentum flow in the boundary layer is subjected to the pressure rise across the shock wave. This sudden pressure rise acts as a high adverse pressure gradient on the boundary layer and if the shock wave is strong enough, the pressure rise across it will cause the boundary layer to separate. Therefore, the possibility of the shock boundary layer interactions to induce flow separation is investigated. In the rotor blade passage, this can only occur in two locations where the shock wave interacts with the tip clearance leakage flow vortex and with the boundary layer over the casing surface. The first location is over the rotor tip suction surface; by examining the rotor tip clearance flow stream lines at the near stall condition shown in Figure 5.10b, no flow separation is observed in this region. The second location is on the casing surface; by examining the velocity vectors near the rotor blade casing in the blade to blade mid-passage plane for the near stall operating point B shown in Figure 5.12, it is observed that the only reversed flow near the casing walls is the tip clearance vortex reversed flow which eliminates the casing flow separation possibility.

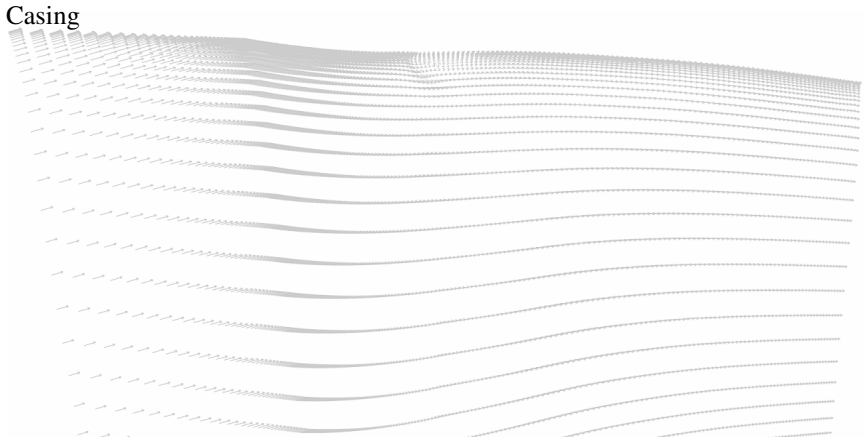

Figure 5.12: Velocity vectors near the NASA Stage 35 casing at rotor mid-passage plane at near stall.

Figure 5.13 shows the velocity vectors near the rotor blade tip leading edge for the stalling point C. In the stalling condition, flow spillage occurs over the rotor tip leading edge which follows well with the stall inception criterion of Vo et al.[19] In their work, Vo et al.[19] showed that the stall inception is most likely accompanied by the forward spillage of the tip clearance vortex flow which is observed here.

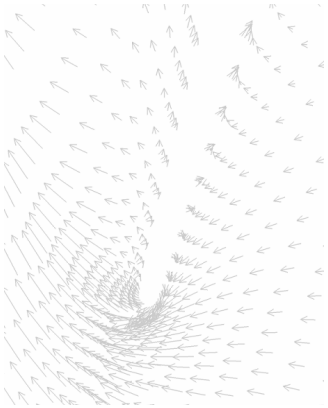

Figure 5.13: Velocity vector near the NASA Stage 35 rotor leading edge at stalling point C.

The fluctuations in the pressure over the rotor casing at a leading edge station and a trailing edge station are shown in Figure 5.14 as the compressor approaches stall. The periodic variations in the magnitude of the pressure values can be observed.

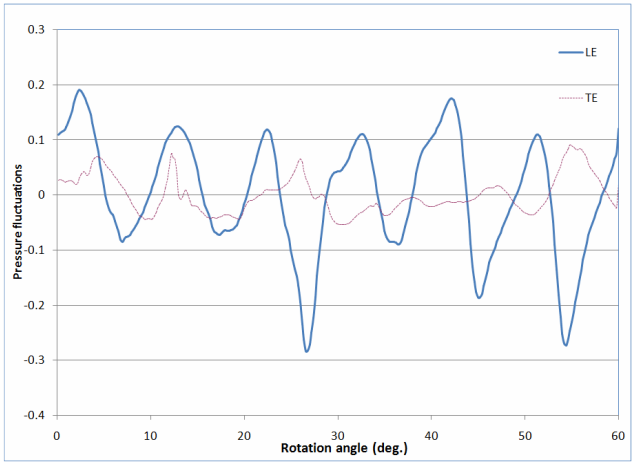

Figure 5.14: Static pressure fluctuations on the NASA Stage 35 rotor casing as the compressor approaches stall.

Finally, Figure 5.15 shows the instantaneous flow field negative axial velocities at the rotor tip section as the compressor approaches stall (going from left to right and from top to bottom). In this figure, lightly shaded regions represent the reverse flow or negative axial velocities and dark regions correspond to positive axial velocities. Figure 5.15 shows that the negative axial velocities in the flow field are initially formed by the rotor tip clearance vortex flow. As the compressor approaches stall, the tip clearance vortex reverse flow impinges the leading edge of the adjacent rotor blade and causes the flow spillage over it which follows well with the stall inception criterion of Vo et al.[19] Then, the flow separates over the rotor blade tip section.

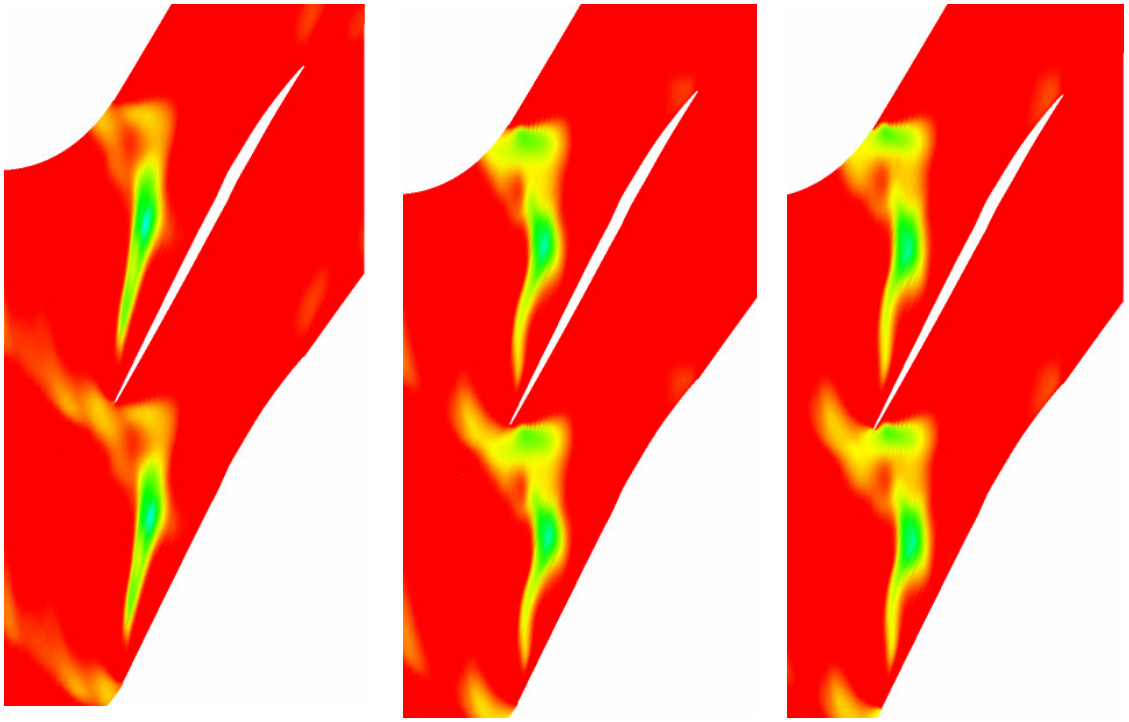

Figure 5.15: Instantaneous negative axial velocity at the rotor tip section as the compressor approaches stall (left to right, top to bottom).

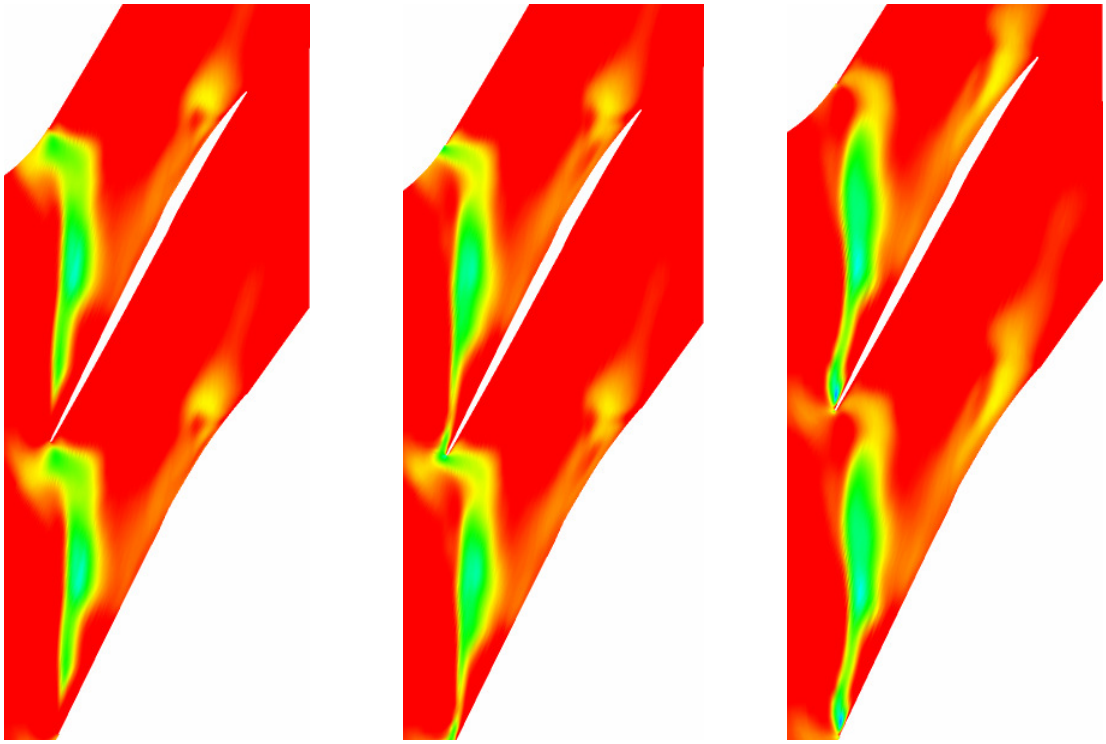

Figure 5.15 (cont.): Instantaneous negative axial velocity at the rotor tip section as the compressor approaches stall (left to right, top to bottom).

To summarize this chapter, the present methodology is applied to study the flow mechanism behind stall inception in the NASA Stage 35 compressor configuration. The answers to the following questions are sought by studying the flow fields in the rotor tip region at the two operating points (near design operating condition and near stall operating condition): What is the behavior of the shock wave? What is the behavior of the tip clearance flow? How does the tip clearance flow interact with the shock wave? Does the shock boundary layer interactions cause flow separation? It is observed that at near stall, the shock wave is stronger and further upstream of the rotor leading edge compared to the near design conditions. The tip vortex is larger in size due to the increased blade loading and is moved further ahead. The interactions between the shock

wave and the tip clearance leakage flow are stronger and alter the trajectory of the tip vortex and the vortex trajectory becomes perpendicular to the main axial flow direction. Those interactions generate a low momentum area near the adjacent rotor blade tip leading edge which causes the flow spillage over it. No shock boundary layer interactions flow separations are found here. Thus, it is believed that the rotor blade tip clearance vortex and its interaction with the shock wave is the main reason behind the stall inception in this compressor stage.

CHAPTER 6

CONCLUSIONS AND RECOMMENDATIONS

An existing 3-D Navier Stokes solver has been extensively modified and improved through the implementation and investigation of a new Hybrid RANS/KES advanced turbulence models, improved rotor-stator interface boundary conditions, and general grid topologies. Parallelization, high order schemes (WENO5), and improved convergence using local time stepping are available as options as well although these features were not used in the present study. Extensive validation studies are done for several 2-D and 3-D configurations ranging from simple isolated airfoils, through axial turbine vanes and compressor blades before applying the current methodology to a transonic compressor stage (rotor + stator).

For the investigations of the advanced turbulence models, a new Hybrid RANS/KES (HRKES) turbulence model has been developed, implemented, and studied for a number of internal and external flows (RAE2822 airfoil, NACA0015 airfoil, Goldman turbine vane, and NASA Rotor 67 compressor configuration). Within the HRKES model, a combination of two blending functions and the use of realizability constraints to bound the parameters of the KES model have been evaluated.

For the investigations of the rotor-stator interface boundary conditions, five different averaging plane approaches have been implemented and studied for the SSME turbine stage. Since the underlying averaging associated with averaging plane methods precludes the accurate transfer of local flow information between the successive blades, an

unsteady sliding mesh interface boundary condition is implemented and validated in the current methodology.

Using the HRKES turbulence model and the unsteady sliding mesh rotor-stator interface boundary conditions, the current methodology is applied to explore the flow mechanisms behind the stall inception in the NASA stage 35 compressor configuration as a representative of a modern compressor stage.

In this chapter, conclusions of this research are presented in Section 6.1 and the recommendations for future work are given in Section 6.2.

6.1 Conclusions

Based on the current studies, the following conclusions can be drawn:

- Existing RANS models are not suitable for predicting the onset of stall even in 2-D flows. Hybrid RANS/LES models are needed for better predictions of separated flows. The Hybrid RANS/KES model developed and studied in the current work (by blending k-ω-SST with KES using the Menter's k-ω-SST F_2 function) showed better predictions in separated flows and in predicating the stall inception than the baseline k-ω-SST model.
- All of the different rotor-stator interface averaging plane approaches studied in the current work predict fairly well the averaged flow field but they preclude the proper transfer of the flow field unsteady wakes/vortices across the rotor-stator interface. An unsteady sliding mesh is needed for such a task.
- Compressor stall events could be detected by monitoring global flow characteristics such as mass flow rate fluctuations and casing pressure data. By

exploring the flow field as the compressor throttles towards stall, the following flow phenomena are observed. The shock wave moves further upstream from the rotor blade leading edge and becomes stronger. The rotor tip clearance flow vortex grows larger and stronger due to the high blade loading at near stall conditions. The interactions between the rotor blade tip vortex and the shock wave also become stronger and more unsteady. Those interactions alter the trajectory of the rotor blade tip vortex which generates a low momentum area near the adjacent rotor blade tip leading edge and cause the flow spillage over it. Therefore, the interactions between the rotor blade tip vortex and the shock wave are believed to be the main reason behind the stall inception in this compressor stage. These findings are consistent with other published research for the same compressor configuration.

6.2 Recommendations

Based on the current studies, the following recommendations are made for future studies:

- To give more generality to the HRKES model, it is recommended to develop and implement a dynamic model for the coefficients of eddy viscosity and kinetic energy dissipation in the KES equations; also, a locally dynamic model for the estimation of the KES model constants should be implemented.
- Due to the expensive computational requirements for using the unsteady sliding mesh interface boundary conditions, it is recommended to develop and implement reduced order models (e.g.: Deterministic Stress Methods) for faster simulation time.

- In the interest of computational time, only one blade passage is modeled in the stall inception predictions, so it is recommended that the current simulations be carried out for multiple blade passages to be able to monitor the evolution of rotating stall.

It is hoped that this work will give a good understanding of the challenges faced in advanced turbulence modeling of separated flows, rotor-stator interface boundary conditions modeling, and the stall inception predictions of axial compressors and that it will serve as a useful step for future research.

REFERENCES

1. Gravdahl, J. T., and Egeland, O., “Compressor Surge and Rotating Stall: Modeling and Control”, London: Springer Verlag, 1999.

2. MacCormack, R. W., “The Effect of Viscosity in Hypervelocity Impact Cratering,” AIAA Paper, 69-35, 1969.

3. Briley, W. R., and Macdonald, H., “Three dimensional viscous flows with large secondary velocity,” Journal of Fluid Mechanics, Vol.144, pp. 47-77, 1984.

4. Beam, R., and Warming, R., “An Implicit Factored Scheme for the Compressible Navier-Stokes Equations,” AIAA Journal, Vol.16, No. 4, pp. 393-402, 1978.

5. Denton, J. D., “An Improved Time Marching Scheme Method for Turbomachinery Flow Calculation,” Journal of Engineering for Power, Vol. 105, no. 3, pp. 514-524, July 1983.

6. Steger, J. L., Pulliam, T. H., and Chima, R. V., “An implicit Finite difference Code for Inviscid and Viscous Cascade Flow,” AIAA paper 80-1427, 1980.

7. Chima, R. V., “Analysis of Inviscid and Viscous Flows in Cascades with an Explicit Multiple-Grid Algorithm,” AIAA paper 84-1663, 1984.

8. McNally, W. D., “FORTRAN Program for Calculating Compressible Laminar and Turbulent Boundary Layers in Arbitrary Pressure Gradients,” NASA TN-D-5681, 1970.

9. Chima, R. V., "Explicit Multigrid Algorithm for Quasi-Three-Dimensional Viscous Flows in Turbomachinery," Journal of Propulsion Power, Vol. 3, No. 5, pp. 397-405, 1987. Also NASA TM 87128.

10. Chima, R. V., "Viscous Three-Dimensional Calculations of Transonic Fan Performance," in CFD Techniques for Propulsion Applications, AGARD Conference Proceedings, No. CP-510, AGARD, Neuilly-Sur-Seine, France, pp. 21-1 to 21-19, Feb. 1992. Also NASA TM 103800.

11. Adamczyk, J. J., Celestina, M. L., Beach, T. A., and Barnett, M., "Simulation of 3-D Viscous Flow within a Multistage Turbine," NASA TM 101376.

12. Hathaway, M. D., "Three Dimensional Flows in Multistage Compressors," NASA N92-70923, pp. 21-34, 1987.

13. Hathaway, M. D., Chriss, R. M., Wood, J. R., and Strazisar, A. J., "Experimental and Computational Investigation of the NASA Low-speed Centrifugal Compressor Flow Field," NASA-TM-4481, 1993.

14. Emmons, H. W., Pearson, C. E., and Grant, H. P., "Compressor Surge and Stall Propagation," Transactions of the ASME 77, pp. 455-469, 1995.

15. Moore, F. K. and Greitzer, E. M., "A Theory of Post-Stall Transients in Axial Compression Systems: Part 1 - Development Equations", ASME Journal of Engineering for Gas Turbines and Power, Vol. 108, pp. 68-76, 1986.

16. Moore, F. K. and Greitzer, E. M., "A Theory of Post-Stall Transients in Axial Compression Systems: Part 2-Application", ASME Journal of Engineering for Gas Turbines and Power, Vol. 108, pp. 231-239, 1986.

17. Camp, T. R. and Day, I. J., "A Study of Spike and Modal Stall Phenomena in a Low-Speed Axial Compressor", ASME Journal of Turbomachinery, Vol. 120, pp. 393-401, 1998.

18. Gong, Y., Tan, C. S., Gordon, K. A., and Greitzer, E. M., "A Computational Model for Short Wavelength Stall Inception and Development in Multi-Stage Compressors", ASME Journal of Turbomachinery, Vol. 121, pp.726-734, 1999.

19. Vo, H. D., Tan, C. S., and Greitzer, E. M., "Criteria for Spike Initiated Rotating Stall", ASME Paper GT2005-68374.

20. He, L. and Ismael, J. O., "Computations of Blade Row Stall Inception in Transonic Flows", ISABE Proceedings, pp. 697-707, 1997.

21. Niazi, S., Stein, A., and Sankar, L. N., "Numerical Study of Surge and Stall Alleviation in a High-Speed Transonic Fan Rotor", AIAA Paper 2000-0225.

22. Hah, C., Rabe, D. C., and Wadia, A. R., "Role of Tip-Leakage Vortices and Passage Shock in Stall Inception in a Swept Transonic Compressor Rotor", ASME Paper GT2004-53867.

23. Haixin, C., Xudong, H. and Song, F., "CFD Investigation on stall Mechanism and Casing Treatment of a Transonic Compressor", AIAA-2006-4799, 42nd AIAA/ASME/SAE/ASEE Joint Propulsion Conference and Exhibit, Sacramento, California, 9-12 July, 2006

24. Adamczyk, J. J., Celestina, M. L., and Grietzer, E. M., "The Role of Tip Clearance in High-Speed Fan Stall," Transactions of the ASME, Vol. 115, January 1993.

25. Chima, R. V., "Calculation of Tip Clearance Effects in a Transonic Compressor Rotor," NASA TM 107216, May 1996.

26. Hah, C., Bergner, J., and Schiffer, H.P., "Short Length-Scale Rotating Stall Inception in a Transonic Axial Compressor – Criteria and Mechanism", Proceedings of GT2006, ASME Turbo Expo 2006, GT2006-90045.

27. Indue, M., Kuroumaru, M., Iwamoto, T., and Ando, Y., "Detection of a Rotating Stall Precursor in Isolated Axial Flow Compressor Rotors", Journal of Turbomachinery Vol.113, No. 2, pp. 281-289, April 1991.

28. Lawless, P. B., Kim, K. H., and Fleeter, S., "Characterization of Abrupt Rotating Stall Initiation in an Axial Flow Compressor", Journal of Propulsion and Power, Vol.10, No. 5, pp. 709-715, September-October 1994.

29. Dhingra, M., Neumeiery, Prasad, J.V.R, and Shinx, H., "Stall and Surge Precursors in Axial Compressors", AIAA 2003-4425, 39th AIAA/ASME/SAE/ASEE Joint Propulsion Conference and Exhibit, Huntsville, Alabama, 20-23 July, 2003.

30. Smith, A. M. O., and Cebeci, T., "Numerical Solution of the Turbulent Boundary Layer Equations," Douglas aircraft division report DAC 33735, 1967.

31. Baldwin, B. S., and Lomax, H., “Thin-layer Approximation and Algebraic Model for Separated Turbulent Flows,” AIAA 1978-257.

32. Spalart, P. R., and Allmaras, S. R., “A One-Equation Turbulence Model for Aerodynamic Flows,” La Rech. A’reospatiale, Vol. 1, pp. 5-21, 1994.

33. Jones, W. P., and Launder, B. E., “The Prediction of Laminarization with a Two-Equation Model of Turbulence,” International Journal of Heat and Mass Transfer, Vol. 15, pp. 301-313, 1972.

34. Wilcox, D. C., "Reassessment of the Scale-Determining Equation for Advanced Turbulence Models," AIAA Journal, Vol. 26, No. 11, pp. 1299-1310, 1988.

35. Menter, F. R., “Two-Equation Eddy-Viscosity Turbulence Models for Engineering Applications,” AIAA Journal, Vol. 32, No. 8, pp. 1598-1605, 1994.

36. Piomelli, U. and Chasnov, J.R., “Large-Eddy Simulations: Theory and Applications,” in Henningson, D., Hallbäck, M., Alfredsson, H. and Johansson, A., Transition and Turbulence Modeling, Doredrecht, Kluwer Academic Publishers, pp. 269-336, 1996.

37. Spalart, P. R., Jou, W. H., Strelets, M., and Allmaras, S. R., “Comments on the Feasibility of LES for Wings, and on a Hybrid RANS/LES Approach,” First AFOSR International Conference on DNS/LES, Ruston, Louisiana, 1997.

38. Strelets, M., “Detached Eddy Simulation of Massively Separated Flows,” AIAA 2001-0879, 39th AIAA Aerospace Sciences Meeting and Exhibit, 2001.

39. Nichols, R. H., “Comparison of Hybrid RANS/LES Turbulence Models on a Circular Cylinder at High Reynolds Number,” AIAA 2005-498, 43rd AIAA Aerospace Sciences Meeting and Exhibit, Reno, Nevada, 2005.

40. Basu, D., Hamed, A., and Das, K., “DES and Hybrid RANS/LES Models for Unsteady Separated Turbulent Flow Predictions,” AIAA 2005-0503.

41. Nichols, S., Sreenivas, K., Karman, S., and Mitchell, B., "Turbulence Modeling for Highly Separated Flows," AIAA 2007-1407, 45th AIAA Aerospace Sciences Meeting and Exhibit, Reno, Nevada, 8-11 January, 2007.

42. Baurle, R. A., Tam, C. J., Edwards, J. R., and Hassan, H. A., "Hybrid Simulation Approach for Cavity Flows: Blending, Algorithm, and Boundary Treatment Issues," AIAA Journal, Vol. 41, No. 8, pp. 1463-1480, 2003.

43. Xiao, X., Edwards, J. R., and Hassan, H. A., "Blending Functions in Hybrid Large-Eddy/Reynolds-Averaged Navier- Stokes Simulations," AIAA Journal, Vol. 42, No. 12, pp. 2508-2515, 2004.

44. Robinson, D. F., and Hassan, H. A., "Further Development of the k– ζ (Enstrophy) Turbulence Closure Model," AIAA Journal, Vol. 36, No. 10, pp. 1825–1833, 1998.

45. Basu, D., Hamed, A., Das, K., and Tomko, K., "Comparative Analysis of Hybrid Turbulence Closure Models in the Unsteady Transonic Separated Flow Simulations," AIAA 2006-117, 44th AIAA Aerospace Sciences Meeting and Exhibit, Reno, Nevada, 9-12 January, 2006.

46. Yoshizawa, A., and Horiuti, K., "A Statistically Derived Subgrid Scale Kinetic Energy Model for the Large-Eddy Simulation of Turbulent Flows," Journal of the Physical Society of Japan, Vol. 54, No. 8, pp. 2834-2839, 1985.

47. Sanchez-Rocha, M., Kirtas, M., and Menon, S. "Zonal Hybrid RANS-LES Method for Static and Oscillating Airfoils and Wings," AIAA 2006-1256, 44th AIAA Aerospace Sciences Meeting and Exhibit, Reno, Nevada, 9 - 12 January, 2006.

48. Menon, S. and Kim, W., "A New Dynamic One-Equation Subgrid Model for Large-Eddy Simulations," AIAA 1995-0356.

49. Fang, Y., and Menon, S., "A Two Equation Subgrid Model for Large Eddy Simulation of High Reynolds number Flows", AIAA 2006-116, 44th AIAA Aerospace Sciences Meeting and Exhibit, Reno, Nevada, 9-12 January, 2006.

50. Fang, Y., and Menon, S., "Kinetic Eddy Simulation of Static and Dynamic Stall," AIAA 2006-3847, 24th Applied Aerodynamics Conference, San Francisco, California, 5-8 June, 2006.

51. Shelton, A., Braman, K., Smith, M., and Menon, S., "Improved Hybrid RANS-LES Turbulence Models for Rotorcraft," presented at the AHS 62nd Annual Forum, Phoenix, Arizona, 9-11 May, 2006.

52. Duque, E. P. N., Sankar, L. N., Menon, S., Ruffin, S., Smith, M., Ahuja, A., Brentner, K. S., Long, L. N., Morris, P. J., and Gandhi, F., "Revolutionary Physics-Based Design Tools for Quiet Helicopters," AIAA 2006-1068, 44th AIAA Aerospace Sciences Meeting and Exhibit, Reno, Nevada, 9-12 January, 2006.

53. Adamczyk, J. J., "Model Equation for Simulating Flows in Multistage Turbomachinery," ASME Paper 85-GT-226, March 1985.

54. Adamczyk, J. J., Mulac, R. A., and Celestina, M. L., "A Model for Closing the Inviscid Form of the Average-Passage Equation System," ASME Paper 86-GT-227, June 1986.

55. Chima, R. V., and Yokota, J. W., "Numerical Analysis of Three-Dimensional Viscous Internal Flows," AIAA Paper 88-3522.

56. Boyle, R. J., and Giel, P. W., "Three-Dimensional Navier-Stokes Heat Transfer Predictions for Turbine Blade Rows," AIAA Paper 92-3068.

57. Hah, C., Tsung, F. L., and Loellbach, J., "Unsteady Flow Analysis in a High turbine Stage with Two Three Dimensional Navier-Stokes Codes," AIAA Paper 97-0503.

58. Wyss, M. L., Chima, R. V., and Tweedt, D. L., "Averaging Techniques for Steady and Unsteady Calculations of a Transonic Fan Stage," AIAA Paper 93-3065.

59. Denton, J. D., "The Calculation of Three Dimensional Viscous Flow through Multistage Turbomachines," ASME Paper 90-GT-19, June 1990.

60. Saxer, A. P., and Giles, M. B., "Predictions of Three-Dimensional Steady and Unsteady Inviscid Transonic Stator/Rotor Interaction with Inlet Radial Temperature Nonuniformity," Journal of Turbomachinery, Vol. 116, pp. 347-357, July 1994.

61. Rai, M. M., "Three Dimensional Navier Stokes Simulation of Turbine Rotor-Stator Interaction; Part I- Methodology," AIAA Paper 87-2058.

62. Niazi, S., "Numerical Simulation of Rotating Stall and Surge Alleviation in Axial Compressors," PhD Dissertation, Georgia Institute of Technology, July 2000.

63. Stein, A., "Computational Analysis of Stall and Separation Control in Centrifugal Compressors," PhD Dissertation, Georgia Institute of Technology, May 2000.

64. Roe, P. L., "Discrete Models for the Numerical Analysis of Time-Dependent Multidimensional Gas Dynamics," NASA Contract Report CR-172574, March 1985.

65. Roe, P. L., "Characteristic-Based Schemes for the Euler Equations," Annual Review of Fluid Mechanics, Vol. 18, pp. 337-365, 1986.

66. Liu, Y. and Vinokur, M., "Upwind Algorithms for General Thermo-Chemical Non-equilibrium Flows," AIAA Paper 89-0201.

67. Yoon, S., Jameson, A., "Lower-Upper Symmetric-Gauss-Seidel Method for the Euler and Navier-Stokes Equations," Journal of AIAA, Vol.26, No. 9.

68. Zaki, M., Suresh, M., and Sankar, L., "A Hybrid RANS/KES Model for External and Internal Flow Applications," AIAA-2008-5216, presented at the 44th AIAA/ASME/SAE/ASEE Joint Propulsion Conference & Exhibit, Hartford, CT, 20-23 July, 2008.

69. Pulliam, H. P. and Steger, J. L., "Implicit Finite-Difference Simulations of Three-Dimensional Compressible Flow," AIAA Journal, Vol. 18, pp. 159-167, February 1980.

70. Zaki, M., Iyengar, V., and Sankar, L., "Assessment of Rotor-Stator Interface Boundary Condition Techniques for Modeling Axial Flow Turbines," AIAA-2006-4619, presented at the 42nd AIAA/ASME/SAE/ASEE Joint Propulsion Conference & Exhibit, Sacramento, CA, 9-12 July, 2006.

71. Chima, R. V., "Calculation of Multistage Turbomachinery Using Steady Characteristic Boundary Conditions", AIAA Paper 98-0968.

72. Giles, M. B., "Nonreflecting Boundary Conditions for Euler Equation Calculations," AIAA Journal, Vol. 28, No. 12, pp. 2050-2058, December 1990.

73. Stein, A., Niazi, S., and Sankar, L. N., "Computational Analysis of the Centrifugal Compressor Surge Control using Air Injection," Journal of Aircraft, Vol. 38, No. 3, pp. 513-520, May-June 2001.

74. Stein, A., Niazi, S., and Sankar, L. N., "Computational Analysis of Surge and Separation Control in Centrifugal Compressors," AIAA Journal of Propulsion and Power, Vol. 16, No. 1, pp. 65-71, January-February 2000.

75. Niazi, S., Stein, A., and Sankar, L. N., "Computational Analysis of Stall Control Using bleed Valve in a High-Speed Compressor," AIAA 2000-3507, 36th AIAA Joint Propulsion Conference, Huntsville, AL, 2000.

76. Niazi, S., Stein, A., and Sankar, L. N., "Numerical Studies of Stall and Surge Alleviation in a High-Speed Transonic Fan Rotor," AIAA 2000-0225, 38th AIAA Aerospace Sciences Meeting, Reno, NV.

77. Cook, P.H., McDonald, M.A., and Firmin, M.C.P., "Aerofoil RAE 2822 - Pressure Distributions, and Boundary Layer and Wake Measurements," Experimental Data Base for Computer Program Assessment, AGARD Report AR 138, 1979.

78. Piziali, R. A., "2-D and 3-D oscillating wing aerodynamics for a range of angles of attack including stall," NASA-TM-4632, 1994.

79. Goldman, L. J., and McLallin, K. L., "Cold Air Annular Cascade Investigations of Aerodynamic Performance of Core Engine Cooled Turbine Vanes. 1: Solid Vane Performance and Facility Description", NASA TM X-3224.

80. Chima, R. V., "TCGRID 3-D Grid Generator for Turbomachinery", User's Manual and Documentation, December 1999.

81. Yeuan, J. J., and Hamed, A., "Three Dimensional Viscous Flow Simulations in a Turbine Stator Using a Nonperiodic H-Typed Grid", AIAA Paper 98-3562.

82. Strazisar, A. J., Wood, J. R., Hathaway, M. D., Suder, K. L., "Laser Anemometer Measurements in a Transonic Axial Flow Fan Rotor", NASA TP-2879, November 1989.

83. Dunn, M. G., Kim, J., Civinkas, K. C., and Boyle, R. J., "Time Averaged Heat Transfer and Pressure Measurements and Comparison with Predictions for a Two Stage Turbine", Journal of Turbomachinery, Vol. 116, pp. 14-22, January 1994.

84. Reid, L., and Moore, R. D., "Design and Overall Performance of Four Highly-Loaded, High-Speed Inlet Stages for an Advanced, High-Pressure-Ratio Core Compressor," NASA TP-1337, 1978.

85. Chen, J., Hathaway, M. D., and Herrick, G. P., "Pre-Stall Behavior of a Transonic Compressor Stage via Time Accurate Numerical Simulation," NASA TM 2008-215163.

86. Davis, R. L., and Yao, J., "Prediction of Compressor Stage Performance from Choke Through Stall," AIAA 2005-1005, 43rd AIAA Aerospace Sciences Meeting, Reno, NV.

87. Hoying, D. A., Tan, C. S., Vo, H. D., and Greitzer, E. M., "Role of Blade Passage Flow Structures in Axial Compress Rotating Stall Inception," Journal of Turbomachinery, Vol. 121, pp. 735-742, 1998.

88. Suder, K. L., Hathaway, M. D., Thorp, S. A., Strazisar, A. J., and Bright, M. M., "Compressor Stability Enhancement Using Discrete Tip Injection," ASME Journal of Turbomachinery, Vol. 123, pp. 14-23, 2001.

89. Chima, R. V., "A Three-Dimensional Unsteady CFD Model of Compressor Stability," ASME GT2006-90040, proceedings of the ASME Turbo Expo 2006, Barcelona, Spain, May 8-11, 2006.